X-ray magnetic circular dichroism in iron/rare-earth multilayers and the impact of modifications of the rare earth's electronic structure

Dissertation

zur Erlangung des Doktorgrades

der Mathematisch-Naturwissenschaftlichen Fakultäten

der Georg-August-Universität zu Göttingen

vorgelegt von

Markus Götz Münzenberg

aus

Gießen

Göttingen 2000

D 7

Contents

List of symbols

chapter 1:

E: energy

$\mu(E)$:   absorption

$\Delta\mu_C$:   X-ray magnetic circular dichroism

$I(E)$:   intensity behind absorber

$I_0(E)$: intensity in front of the absorber

chapter 2:

$\rho(E)$: density of d-electrons

$\rho_n(E)$: density of d-holes

$\rho_n^{\uparrow}(E)$: density of spin up d-holes

$\rho_n^{\downarrow}(E)$: density of spin down d-holes

ω: transition probability

M : $2p \rightarrow 5d$ radial transition matrix element

$M^{\uparrow}$: $2p \rightarrow 5d$ transition matrix element for spin-up photoelectrons

$M^{\downarrow}$: $2p \rightarrow 5d$ transition matrix element for spin-down photoelectrons

I_{L3}:   area of the L_3-white line

I_{L2}:   area of the L_2-white line

A: area of the L_3-XMCD signal

B: area of the L_2-XMCD signal

m_S: spin moment

m_S^{α}:   angular dependent spin moment

m_O :   orbital moment

m_O^{α}:   angular dependent orbital moment

α: parameter of the phenomenological analysis, effective dichroic polarization of the measured 5d-dichroism

β: parameter of the phenomenological analysis, energy splitting of the 5d-spin
          split band

ψ_i: wavefunctions

$L(E)$: Lorentzian function

A_L: amplitude of $L(E)$

2Γ: full halfwidth of $L(E)$

chapter 4:

B_{hf}:   magnetic hyperfine field

$p(B_{hf})$: magnetic hyperfine field distribution

chapter 5:

A_{ex}:   magnetic exchange stiffness

L_{ex}:   magnetic exchange length

$K(K_1)$: (uniaxial) magnetocrystalline anisotropy energy

$<K>$: random crystalline anisotropy

T_C: Curie temperature

0. Introduction

Orbital and spin magnetic moments are invaluable quantities for the understanding of macroscopic magnetic properties of matter. The decomposition of the total magnetic moment in a multicomponent, heteromagnetic system into various orbital and spin moment contributions of each element would be a significant progress in understanding the mechanisms underlying technologically important aspects of multilayer and alloy materials, such as magnetoresitance, magnetic anisotropy, and coercivity.

The recent experimental development of the X-ray Absorption Spectroscopy (XAS) and the magnetic counterpart the Magnetic Circular Dirchroism (XMCD) [1], together with the development of new generations of synchrotron radiation facilities with high photon flux and the two important sum rules developed from the theoretical side [2], propose a new procedure to deduce element-specific orbital and spin magnetic moments of the valence-band partial density of states with s, p, d or f character.

Rare earth (RE) materials are interesting for technical applications because of their 4f electrons that strongly influence the magnetic properties. There is a complex interplay between the 5d electrons, the outer electron shell which forms the bonding, and the 4f shell that tends to localize at the atom. Both carry a magnetic moment. The 5d shell acts as a transmitter of the magnetic interactions. But the interpretation of the dichroism at the rare-earth (RE) $L_{2,3}$ edges, which probes the RE-5d valence electron states by the dipole transition $2p \rightarrow 5d$, is still a topic of controversial discussion. The signal does not reveal the magnetic polarization of the 5d electrons in the ground state, the sum rules fail and predict even the wrong sign of the magnetic moments [3]. The line shape observed is determined by the intra-atomic Coulomb interactions between the photoelectron and the magnetically

aligned 4f electron. As it was pointed out at first for Gadolinium [4], this may be attributed the polarization dependence of the dipole matrix element: due to the 4f-5d exchange interaction, the 5d majority spin shell is contracted and a stronger overlap with the wave function of the core level electron enhances the transition probability. This contribution yields an opposite sign of the dichroism. Because of the life time of the core hole, the density of hole states of cannot be resolved in the XAS experiment. Thus the analysis of the XMCD-$L_{2,3}$ spectra yields to essentially two parameters that determine the shape of the circular dichroism. In a simple phenomenological model, the first parameter describes the difference in amplitude of two Lorentzians; It is related to the spin-polarization of the valence states which competes with a spin dependence of the transition probability. The and the second parameter is associated with a shift in energy of the two Lorentzians.

Up to now mostly bulk compounds were studied and discussed within similar phenomenological approaches [3,5]. In this work, the different mechanisms and magnetic interactions in Fe/RE-mulitlayer systems will be discussed. The magnetic and electronic structure of the RE sublayer is modified by the formation of

- the hydride REH_X with metallic (dihydride) and insulating characteristic (trihydride) of the REH_X sublayer in Fe/ReH_X-multilayer structures and
- by alloying Si into the RE sublayer.

For the Fe/REH_X-multilayer samples (with RE= Ce, La and Gd) the electronic properties of the magnetic/paramagnetic interface are studied. The metal-to-insulator transition in the REH_X can simply be induced during the experiment by the application of a hydrogen atmosphere of 10-1000 mbar. It is an interesting task to determine the character and decrease length of the magnetic-interface polarization induced by the 3d-Fe states for the metallic REH_2-dihydride phase and the insulating REH_3 trihydride. La and Gd are a borderline case for the application

of the phenomenological model.

The experiments performed on the Fe/Ce$_{1-X}$Si$_X$ multilayers are conceived to induce a smooth progression of the 4f-states in the multilayers from itinerancy to localization, i.e. between the α and γ-like configurations of Ce by increasing the content x of the s-p element Si. It is the aim to study the impact of this effect on the Ce-L and M isotropic and XMCD spectra.

The determination of the interface polarization in ferromagnet/insulator structures is a topic of actual research interest. Such studies are of special interest for the optimization of the tunneling barriers, used in sensor modules or new ultrafast non-volatile storage applications. Another topic of strong interest is the role of exchange biasing. An antiferromagnet/ferromagnet structure leads to a magnetic pinning at the interface and thus a magnetic hardening of the ferromagetic layer. This actual topic is touched in the case of the Fe/GdH$_X$ multilayers. Here, the strength of the antiferromagnetic order below T$_N$ ~20 K can be changed by additional charging with hydrogen which modifies the electronic structure. The element selectivity of the dichroism measurement is an indispensable method to reveal the antiferromagnetic ordering at the Néel temperature of the GdH$_X$ sublayer separately.

The capability of the element selectivity of the circular dichroism will be demonstrated for soft magnetic Fe/Ce multilayers. The contribution of the Ce-5d magnetism to the hysteresis curves is determined. The role of the interfaces and their influence on the soft magnetic properties are shown and compared with two reference samples that are considerably harder.

To summarize, dichroism at the RE-L$_{2,3}$ edges, resulting from complex inter and intra-atomic interactions, is measured and analyzed in a phenomenological model for different well defined Fe/RE-multilayer systems. Not for the test's sake alone, but also to apply it to the investigation on topics of actual research interest, that

are connected with the new research areas, magnetoelectric engineering and spin electronics, and thus the use of the up to now in semiconductor electronics not-utilized additional degree of freedom: the spin of the electron.

0. 1 Scope of the work

The structure of the thesis is as follows:

Chapter 1: It contains a description of the techniques used for the preparation and characterization of the TM/RE multilayer samples. Experimental details concerning the measurements of the XAS and XMCD spectra, at the Laboratoire pour l'Utilisation de Rayonnement Electromagnétique (LURE) and European Synchrotron Radiation Facitlity (ESRF) are included in the last paragraph.

Chapter 2: The electronic properties of the Ce-4f-electron states (localized $\leftrightarrow$ itinerant) and the resulting electron correlation and the magnetic interactions in transition-metal(TM)-rare-earth(RE) compounds are discussed in the simple band model of Brooks [6] at first. In the second part, an introduction of the atomic description of the absorption process is given, and the origin of the XMCD and the sum rules and their applicability will be discussed. Finally, a simple phenomenological model for the description of the XMCD at the RE-$L_{2,3}$ edges is presented and discussed in view of actual discussions on the interpretations of the $L_{2,3}$ XMCD spectra at the RE edges.

Chapter 3: The metal-to-insulator transition in RE-hydrides is used as an object for studying the fundamental changes of the electronic properties of the REH$_X$ sublayer, induced by variation of the hydrogen concentration.

The modification of the magnetic polarization at the interface of multilayers of REH_X (RE: La, Ce) with Fe is studied across the metal-to-insulator transition in the REH_X sublayer by XMCD measurements. These measurements yield the penetration depth into the REH_X sublayer in the metallic and in the insulating state. The phenomenological model presented in chapter 2 is used as a tool to extract the characteristic parameters. In the case of the Fe/GdH_X multilayers, the antiferromagnetic order observed at ~20 K and is studied for different hydrogen concentrations x aswell.

Chapter 4: The gradual progression of the Ce 4f-states from itinerancy to localization, i.e. between the α and γ-like Ce configurations, is presented. The smooth progression is induced by increasing the content x of the s-p element Si in Fe/$Ce_{1-X}Si_X$ multilayers. It is the aim to study the impact of this effect on the Ce-L and M isotropic and XMCD spectra.

Chapter 5: The element selectivity intrinsic to the XMCD is used to explore the magnetic interactions that result in a very soft hysteresis observed for Fe/Ce-multilayer samples. The differences in the element-selective hysteresis data measured by means of XMCD at the Ce-L_2 edge and the magneto-optical Kerr effect, which represents the Fe magnetization, are discussed within two models. They explain the tilted orientation of the average Fe and Ce-5d magnetizations observed in the hysteresis curves at small magnetic fields.

12   Literature

1   G. Schütz, W. Wagner, W. Wilhelm, P. Kienle, R. Zeller, R. Frahm and G. Materlik, Phys. Rev. Lett **58**, 737 (1997)

2   B. T. Thole, P. Carra, F. Sette, G. van der Lahn, Phys. Rev. Lett. **68**, 1943 (1992); P. Carra, B. T. Thole, M. Altarelli, X. Wang, Phys. Rev. Lett. **70**, 694 (1993)

3   J. B. Goedkoop, A. Rogalev, M. Rogaleva, C. Neumann, J. Goulon, M. van Veenendaal and B.T. Thole, J. Phys. F. **7**, C2-415 (1997)

4   B. N. Harmon, A. J. Freeman, Phys. Rev. B **10,** 1979 (1974)

5   R. M. Galéra, S. Pizzini, J. A. Blanco, J. P. Rueff, A. Fontaine, Ch. Giorgetti, F. Baudelet, E. Dartyge and M. F. López, Phys. Rev. B **51**, 15957 (1995); J. P. Rueff, R. M. Galéra, S. Pizzini, A. Fontaine, L. M. Garcia, Ch. Giorgetti, E. Dartyge, F. Baudelet, Phys. Rev. B **55**, 3063 (1997)

6   M. S. S. Brooks, et al., J. Phys. Condens. Mater **1**, 5661 (1989), M. S. S. Brooks Physica B **172**, 95 (1991); B. Johansson, L. Nordström, O. Eriksson, and M.S.S. Brooks, Physica Scripta **T 39**, 100 (1991); M. S. S. Brooks and B. Johansson, in *Handbook of Magnetic Materials*, edited by K. H. J. Buschow (North Holland, Amsterdam, 1992), Vol. 7, p. 139

1. Experimental methods

In this chapter a description of the techniques used for preparation and characterization of the samples is given. It includes a short discussion of the beamlines.

1. 1 Sample preparation - the sputtering chamber

The samples are prepared by ion-beam sputtering in a UHV-chamber (figure 1.1) with a base pressure of $\sim 10^{-10}$ mbar. The residual gases are mainly CO and H_2. The working pressure of the Kaufmann ion source (Ion Tech) is $4 \cdot 10^{-5}$ mbar Ar (6N). This is two orders of magnitude lower than for magnetron sputtering systems. Inside the preparation chamber four target positions are available for 3" diameter targets with a purity of >99.99 for the transition metals and 99.9 for the rare earths. Each multilayer is grown automatically controlled by a quartz balance and a PC. Typical growth rates are 0.3-0.4 Å/s for the reactively grown hydride layers and 0.5-1 Å/s for the transition metals and pure rare earth targets. The energy of the Ar^+ ions is about ~ 1 keV.

The reactively grown hydrogenated samples LaH_X, CeH_X and GdH_X are sputtered in a hydrogen atmosphere of $6 \cdot 10^{-6}$ mbar H_2 (6N). It leads to a growth in the dihydride phase REH_X with $x=2-\delta$. An investigation by the resonant nuclear reaction $^1H(^{15}N, \alpha, \gamma)^{12}C$ revealed a stable hydride in the case of RE=La, Ce with $x \sim 1.5$ [1]. The solubility of H in Fe is very small.

Fe/Ce and Fe/Ce_XSi_{1-X} samples are prepared on substrates cooled to $l(N_2)$ temperature to avoid diffusion. The CeSi target is composed of a Ce target, that is

partly covered by a 0.5 mm thick Si wafer. A regular array of drilled holes aids to lead to a homogeneous $Ce_{1-X}Si_X$ alloy concentration over the whole sample area [2]. The concentration ratio was roughly estimated by the ratio of the Ce and Si surface areas times the sputter rate and measured precisely by Rutherford backscattering afterwards [3]. The error for the concentration yielded from the intensities of the backscattered α particles is of 2%. For the combined targets an enhancement of the sputter rate of the Si in comparison with the rate of the pure Si target has to be taken into account.

The substrates (Si(100), glass, Kapton or Mylar fixed on a copper frame [4]) are equally preacoated with a 40Å Cr or Pd buffer layer, to warrant the same growth and general characteristics of the samples [5]. Note: the texture of the Fe/REH_X multilayer is induced by the growth (as it will be discussed in chapter 3). The multilayer stack is covered with a 80 Å thick protection layer of Pd (Fe/REH_X multilayers) or Cr (Fe/Ce_XSi_{1-X} multilayers).

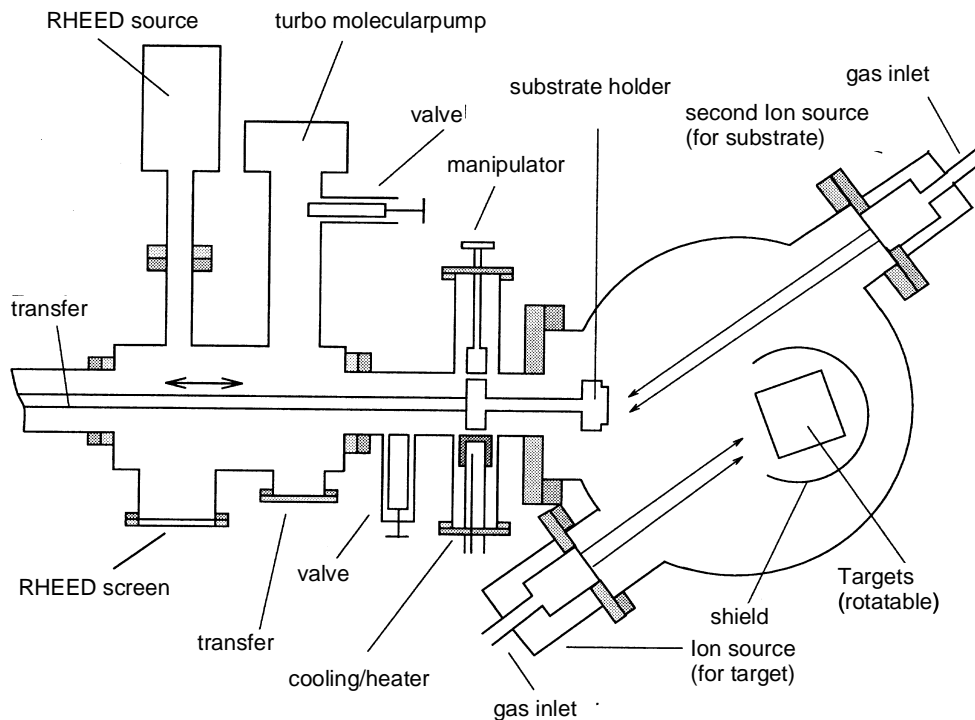*Figure 1.1. The schematic drawing of the UHV-chamber.*

Ar⁺

ballistic energy
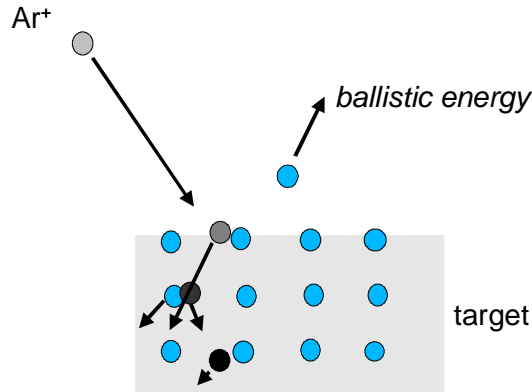
target

Figure 1.2. Schematic sputtering process. The Ar⁺ ion with an energy of ~1 keV deposits kinetic energy into the target and sputters the target material in a ballistic cascade

The growth is quite different compared to the epitaxial beam deposition technique. Here the energy of the deposited material is equivalent to the thermal energy (below 1 eV). Whereas the energies of the deposited atoms are quite higher for the ion-beam sputtering (above 10 eV). Therefore the interdiffusion may be stronger, but the deposited material is denser and the layers are smoother in general with a lower interfacial roughness. The schematic sputtering process is visualized in figure 1.2.

1. 2 X-ray diffraction

The structure of the multilayers is determined with a Phillips diffractometer (Cu-K$_\alpha$ radiation). The experiments are performed in $\Theta/2\Theta$-geometry for low scattering angles of 0.3 to 15°, where the measurement is sensitive to the chemical superstructure (length scale 10 to a few 100 Å), and in the range of 20 to 145°, for the determination of the crystal structure of the constituent layers (length scale 4 Å to 0.7 Å). In $\Theta/2\Theta$-geometry, the scattering vector is always perpendicular to the layer plane and thus oriented in the growth direction.

In the small-angle range, the optical density changes with the chemical modulation in the multilayer. In the optical theory, that includes the refraction for the grazing incidence [6,7], the optical density is transferred into a scattering potential reflecting the chemical periodicity, which is shown in figure 1.2 (middle). The interfacial roughness and diffusion are simulated by a rms (full width at half maximum) variation of the potential curve. The result of a simulation with a program written by De Haan [4] is shown schematically on the right: for small angles the whole intensity is reflected until a critical momentum transfer q_C is reached (~ 0.8° for the Fe/RE multilayers). For larger angles the scattered photons form standing wavefields at the Bragg condition. This results in an oscillation in the reflectivity corresponding to the chemical structure. For multilayers with a number of repetitions n>30 and small interface roughness the Bragg peaks are

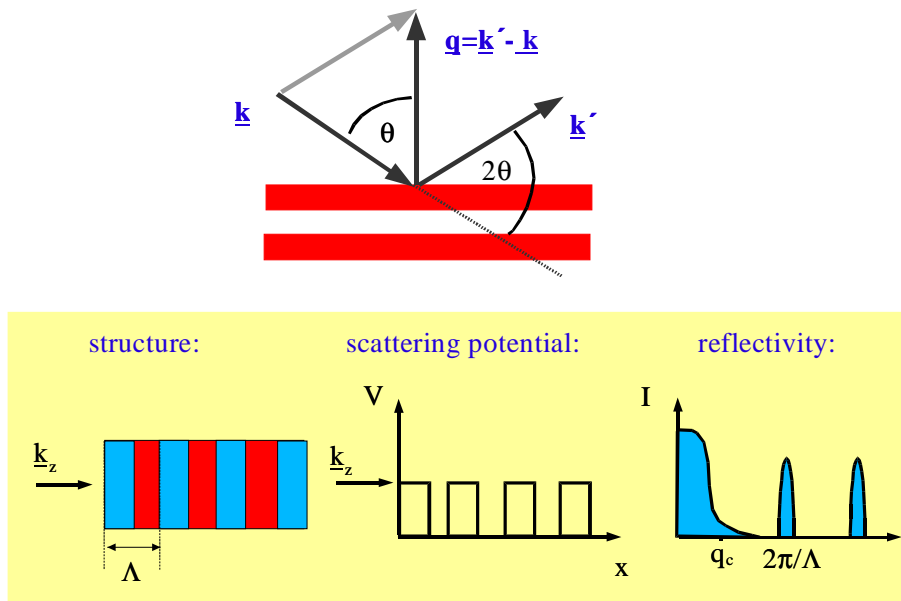*Figure 1.2. The scheme of the Θ/2Θ-scattering geometry is shown at the top. The scattering vector q is parallel to the layer normal. A chemical modulation profile results in an effective scattering potential V with the periodicity Λ as shown in the middle. Thus, the total reflection up to a critical momentum transfer q_C and the intensity at the multiple Bragg peak orders can be calculated.*

very narrow. The width corresponds to the number of layers that scatter coherently. For a higher roughness, the intensity of the Bragg peaks decreases faster for larger angles. This spectrum is superposed by broad oscillations generated by the capping layer (fringes), which are not shown in the schematic drawing. The thickness can be determined up to a precision better than 0.5 Å [8].
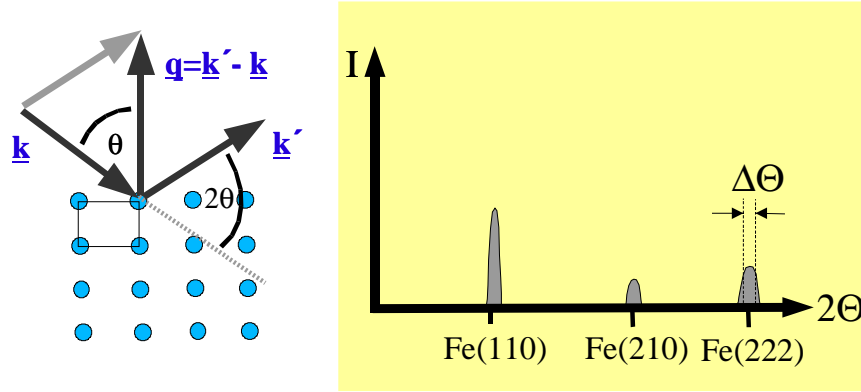
Figure 1.3. Scattering geometry for the Θ/2Θ-setup. In the large-angle region the lattice periodicity and the crystallite size is probed.

In the high-angle X-ray diffraction range, schematically shown in figure 1.3, the crystallinity of the thin-film structure is probed. From the position of the reflections, the lattice parameter is calculated and using the Debeye Scherrer formula the crystallite size D_{hkl} in growth direction can be estimated.

$$D_{hlk}\left[\mathring{A}\right]=\frac{K\,1.5418\left[\mathring{A}\right]}{\sqrt{\left(\frac{\Delta}{57.3}\right)^2-\left(\frac{\Delta_{Standard}}{57.3}\right)^2}\cos\Theta} \qquad 1.1$$

$\Delta(2\Theta)$ is the width of the peak, $\Delta_{Standard}(2\Theta)$ is a correction for the resolution that is measured with a Si standard. The value is ~0.08° for the Phillips diffractometer. K is the form factor of the crystallites. It is 0.9 for spheres and 1.84 for a two dimensional lattice like graphite. In the following, 0.9 is taken for the calculations.

The real value is expected to be somewhat above unity. For more detailed information see, for example, ref. [5].

1. 3 Magnetometry

The macroscopic magnetic properties of the multilayer samples are characterized by two standard methods that both have different advantages: the magneto-optical Kerr effect (MOKE) and vibrating sample magnetometry (VSM). The magneto-optical Kerr effect (figure 1.4, top) corresponds to a change in the polarization state of light reflected from a magnetic material. The polarization rotation (Kerr-rotation angle) is in the order of a few 1/100 degree. This method is a very sensitive tool even for measuring the hysteresis curves of thin films down to a thickness of a few monolayers. The penetration depth of the light is ~300 Å for the He-Ne-wavelength (632.8 nm). The Kerr-rotation angle is proportional to the magnetization, but the size and the sign of the signal depends on the angle of incidence and the wavelength. This was shown in depth sensitive experiments by Ferré et al. [9] or by calculations of the magneto-optical Kerr effect for Fe, Co and Ni by Johansson et al. [10].

The samples are measured in the longitudinal geometry (field in plane of incidence and in the layer plane). The Kerr rotation is measured with a photoelastic modulator setup (PEM-90, Hinds Instruments), probing the sample with a polarization modulated beam. One polarization component of the reflected beam is filtered by an analyzer, the intensity is measured and correlated to the modulation frequency [11,12,13,14]. Within this setup it is possible to measure the Kerr angle with a sensitivity of 10^{-4} degrees providing the possibility to resolve the hysteresis of a 6 Å thick Fe film. The angle of incidence is about 65° taken from the layer normal. The setup used is standard, with two magnetic field ranges, one from 0-1000 Oe with a Helmholtz coil, and an electromagnet for fields up to 16 kOe. An optical cryostat allows measurements at temperatures from 15-300 K.
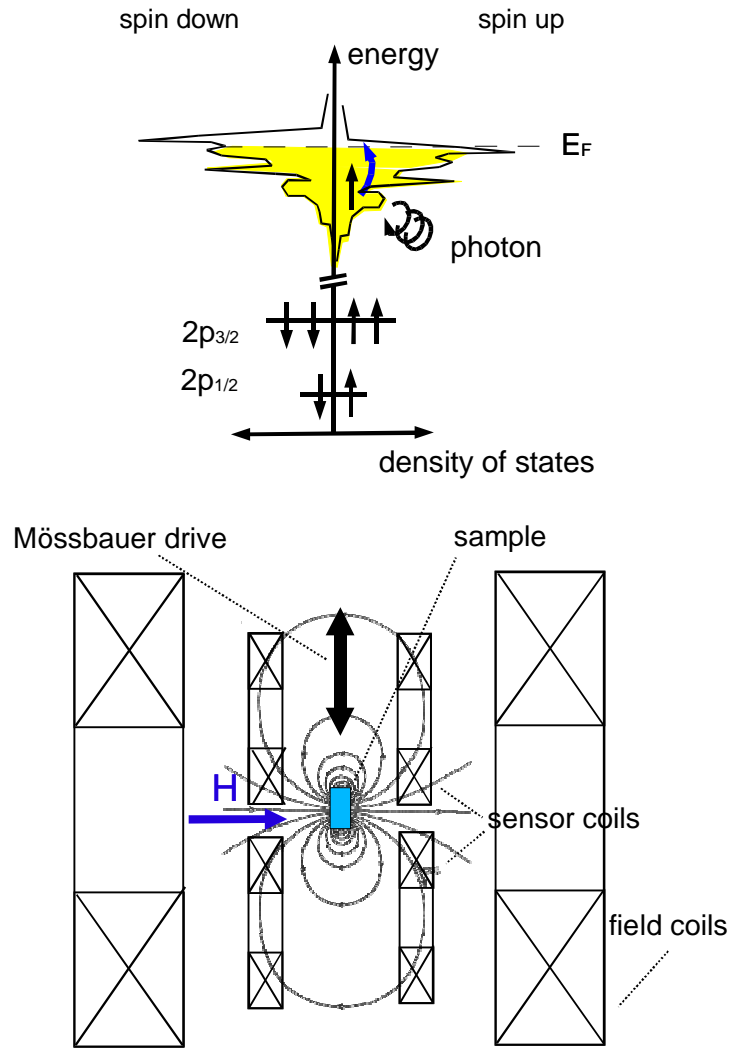
Figure 1.4. Top: inter-band transitions of the magneto-optical Kerr effect are shown schematically. They determine the absorption for right and left circularly polarized light. Bottom: Schematic setup of the vibrating sample magnetometer (VSM).

In figure 1.4 (bottom) the schematic setup of the vibrating sample magnetometer (VSM) is shown. The sample is periodically moved by a Mössbauer drive and induces a signal into the sensor coils via the dipole field. The field is applied horizontally by a superconducting split-coil magnet. The upper sensor coils are wound in the opposite sense. Thus, the signal from the dipole field of the sample is doubled and the signal induced by a change of the applied field vanishes. The

signal is calibrated with a reference Ni foil with the same geometry as the sample. In contrast to the MOKE the absolute magnetization is measured. In the case of the VSM the field is applied by superconducting coils in a field range up to 70 kOe. The temperature range is 4.2 - 300 K.

1.4 X-ray Magnetic Circular Dichroism (XMCD) - the beamlines

The X-ray absorption and XMCD-spectra are recorded in transmission mode to probe the entire volume of the multilayers. The absorption $\mu(E)=\beta(E)t$ (equation 1.2) is measured as a function of the energy. β is the absorption coefficient, $I_0(E)$ is the incident intensity and $I(E)$ is the intensity transmitted by an absorber with the thickness t.

$$\mu(E)=\beta(E)t=-\ln\frac{I(E)}{I_0(E)} \qquad\qquad 1.2$$

The XMCD is defined as the difference, between the absorption of a right and left circularly polarized X-ray beam by a magnetized sample, with $\mu_+(\mu_-)$ representing the absorption of circularly polarized X-rays with their angular momentum parallel (antiparallel) oriented to the ferromagnetically ordered moment

$$\Delta\mu_C=\mu_+ - \mu_- \qquad\qquad 1.3$$

The absorption spectra at the rare earth (RE) -$L_{2,3}$ edges are measured at the energy-dispersive beamlines ID 24 of the European Synchrotron Radiation Facility (ESRF, Grenoble) and D11 of the DCI storage ring of the Laboratoire pour l'Utilisation de Rayonnement Electromagnétique (LURE, Orsay). The relevant energy range that can be reached is between 5 and 25 keV. The resolution at the RE edges is 0.1-0.3eV.
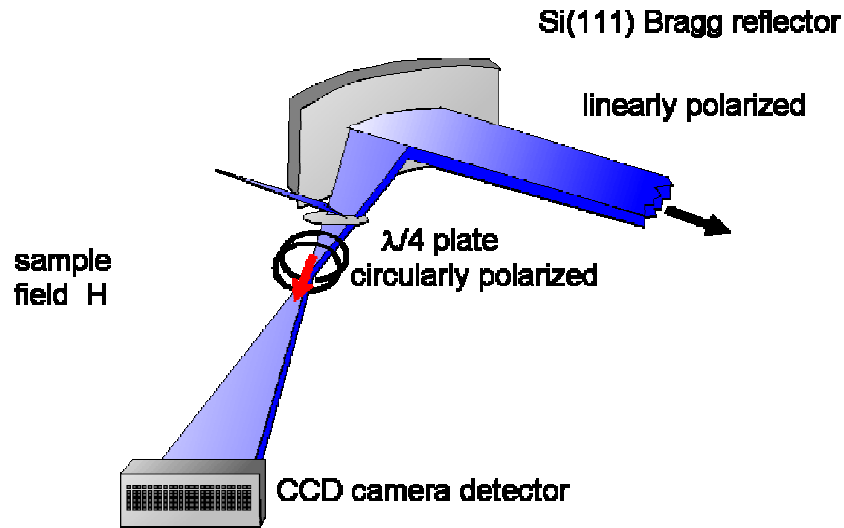
Figure 1.5. Schematic layout of the energy-dispersive experimental station at ESRF.

Because of the transmission geometry, the samples are grown on different substrates depending on the energy range of the absorption edge. For the measurements at the RE-L edges (energy range: 5-10 keV), the multilayers are deposited on a Kapton foil (12 µm) with a total thickness of 4000 Å. In the transmission experiment, ~ 12 pieces are stacked. This results in a total RE thickness of 2-4 µm and the increase of the absorption is ~0.3 to 0.4 at the absorption edge.

The principle of the setup is the same at both beamlines (figure 1.5): the first Bragg mirror focusses the beam on the sample position. Thus experiments, e.g. in a very small diamond pressure cell can be done. The focus at ID 24, for example has a diameter of ~ 20 µm with a flux of 10^{12} photons/s. Behind the sample the beam spreads again and is detected by a CCD based camera. The bending mirror close to Si (111) Bragg condition cuts and reflects X-ray pass band. Because of the energy dispersion the whole spectral range can be recorded simultaneously.

This is favorable for time dependent measurements. The calibration of the energy has to be done with a reference sample. Thus one obtains a gauge relation between camera pixel and energy.

The two beamlines differ in their flux (DCI is a first generation and ESRF a third generation synchrotron) as well as in their degree of circular polarization. At the beamline D11 the 'natural' circular polarization a few degrees above the positron orbit is used. This entails a loss in intensity. The circular polarization rate depends on the position of the slits behind the Bragg monochromator and is about 60%.
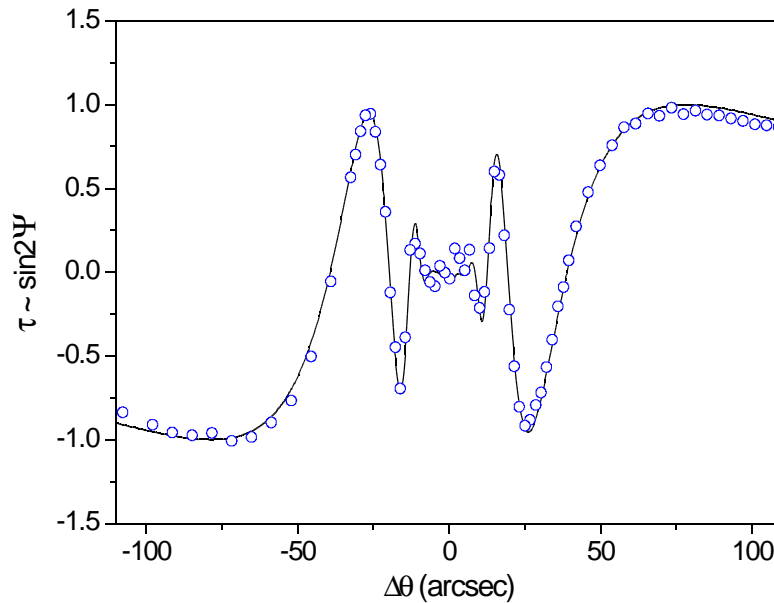
Figure 1.6. Polarization rate versus the offset of the position of the (111) Bragg angle of a diamond crystal in Laue geometry. The fit is calculated using the dynamical theory.

In the case of the energy-dispersive beamline ID 24 at the ESRF, a quarter wave plate (QWP, diamond plate, 707 μm thick) is inserted in Laue geometry close to the (111) reflection. The incident beam is linearly polarized and after passing the QWP, due to its birefringent properties at a special Bragg condition, circularly

polarized. The function of the polarization v.s. angle is plotted in figure 1.6 [15] for a scan around the diamond (111) Bragg condition. By flipping the angular positions the polarization can be flipped within 1 s. This technique is a key aspect for the measuring of element-selective hysteresis curves: at each magnetic field value of the hysteresis cycle the polarization can be flipped between the two positions and the difference spectra of the spectra corresponds to the XMCD.

The absorption spectra at the RE-$M_{4,5}$ edges of the and Fe-$L_{2,3}$ edges are recorded at the beamlines SU 22 and SU 23 of the Super ACO storage ring of LURE, respectively. For the absorption geometry in the soft X-ray range below 1000 eV the samples are deposited on a 1.5 μm thick mylar foil. The foil is fixed on a copper frame and coated with a thin Al-film on the back to obtain a better thermal contact. The transmission of this coated substrate films is about ~ 0.3. A total thickness of 150 Å is chosen for the RE part of the film. Its absorption is 0.12 at the M_5 edge and 0.02 in the pre-edge region. Both beamlines are scanning-monochromator-like. For SU 22 the natural circular polarization above the electron orbit is used. The monochromator is a Si double crystal. Here the polarization rate was 25% and 17% for the M_5 and M_4 edges respectively, depending on the energy. SU 23 is equipped with a so called Dragon monochromator (a bended Si monochromator). Here the polarization is 60%. For more detailed information see e.g. reference [16].

1   A. Weidinger, F. Klose, private communications

2   thanks to the knowledge of drilling Si wafers of Markus Peuker, Institut für Röntgenpysik, Universität Göttingen

3   measurements performed by Leena Rissanen, II. Physikalisches Institut, Universität Göttingen

4   Bond Seal Repair, Huntington Mechanical Laboratories

5   F. Klose , PhD thesis, Universität Göttingen (1993)

6   L. G. Paratt, Phys. Rev. **95**, 359 (1954)

7   V. O. de Haan, G. G. Drijkonigen, Physica B **198**, 24 (1994)

8   W. Lohstroh, PhD thesis, Universität Göttingen (1999)

9   J. Ferré, P. Meyer, M. Nylt, S. Visnovsky, D. Renard, J. Magn. Magn. Mater. **165**, 92 (1997)

10 T. Gasche, M.S.S. Brooks, B. Johansson, Phys. Rev. B **53**, 296 (1996)

11 S. N. Jasperson, S.E. Schnatterly, Rev. Sci. Inst. **40**, 761 (1969)

12 R. M. A. Azzam, *Ellipsometry and polarized light*, North Holland, Amsterdam, 1977

13 K. Sato, Jap. J. of Appl. Phys. **20,** 1981, 2403

14 M. Münzenberg, Diplomarbeit, Universität Göttingen (1997)

15 M. Bonfim, K. Mackay, S. Pizzini, A. San Miguel, H. Toletino, C. Giles, T.Neisius, M. Hagelstein, F. Baudelet, C. Malgrange and A. Fontaine, J. Synchrotron Rad. **5**, 750 (1998)

16 Guide Technique, LURE (1992), A.-M. Dias, Thesis, Université de Paris 6 (1997); A. Delobbe, Thesis, Université de Paris-Süd(1999); M. Arend, PhD thesis, Universität Göttingen (1998)

2. X-ray magnetic circular dichroism - magnetic interactions

This chapter will describe the origin of X-ray magnetic circular dichroism (XMCD) at the $L_{2,3}$ edges, especially with respect to the interpretation at the rare earth (RE) edges. Since the shape of the dichroic signal at the RE-$L_{2,3}$ edge is strongly connected to the magnetic interactions, this results in difficult mechanisms of the different magnetic interactions. However, they are especially interesting for illuminating the magnetic properties in multilayer systems. In the first paragraph, the magnetic interactions in transition-metal(TM)-rare-earth(RE) compounds will be described. Then, the origin of the XMCD and the sum rules and their applicability will be discussed, followed by a phenomenological model for the description of the XMCD at the RE-$L_{2,3}$ edges.

2.1 Cerium

Cerium is a fascinating element for studies of magnetism which is, as in the other RE elements, profoundly related to the nature of the 4f-electron states. Ce is a special case because the 4f states are at the borderline between localization and itinerancy. Both aspects can be realized, depending on the degree of mixing of the 4f and conduction-electron states, either in the γ or α-phase of pure Ce or in compounds with transition metals. Dramatic differences in the physical properties and very complex phase diagrams mirror the unlike ground state configurations [1]. Theoretical work on Ce metal has been focused mostly on the transition from the fcc γ-phase to the isostructural but much denser (~17%) α-phase, which may be driven thermally or by the application of pressure. I has become clear by now that a good account of this transition is obtained by a model treating the

4f-electron states as localized (nonbonding) in γ-Ce and itinerant (bonding) in α-Ce [2,3]. A strong hybridization of the 4f states with the conduction band makes α-Ce an archetype for a highly correlated system. The interest in this element is linked to the fact that α-Ce has a non magnetic ground state, but in compound with d-band transition metals, like $CeFe_2$ or $CeCo_5$ where Ce adopts an α-phase-like electronic structure, experiments [4,5] and theoretical work [6,7] reveal that its ground state is magnetically ordered with a magnetic moment on its 4f states. Key parameter which governs this behavior are the intra-atomic Coulomb interaction among the 4f states and the interaction between the 4f and the 5d states among themselves and with the surrounding environment in a given system through hybridization and exchange [8]. In view of these properties the recent studies in our laboratory on the multilayers combining Fe and Ce, Fe and $CeH_{2-\delta}$, intended to probe the local electronic structure and magnetism at the interfaces with Fe. The experiments were aimed at the 4f and 5d states. The latter ones are well known to tune the magnetic properties in the RE-TM systems. The experiments in this work were performed in the same context.

2.2 Magnetism in transition metal-rare earth compounds

Magnetism at TM-RE compounds has been successfully explained by the model of Brooks and Johansson [7] at the end of the 80's. The basic mechanism will be discussed in a simple picture of a rectangular shaped density of states (DOS). In the case of Fe with an electron configuration of $[Ar]\, 3d^6\, 4s^2$, only the 3d states and for the RE with an electron configuration $[Xe]\, (5d\, 6s)^3 4f^n$, the 5d RE and 4f states have to be taken into account. The p- and s bands do not have a structure and therefore they can be neglected in the discussion of the hybridization effects and magnetic interactions.

The 5d-RE and 3d-TM bands for the separated metals are shown in figure 2.1 at the left. The DOS of the 5d-RE states and 3d-Fe states is represented in black and white rectangles respectively. The energy of the RE-5d states is above the TM-3d states. The model for the ionic TM/RE compound is in the middle: the charge will be transferred to the TM-3d band. The filling with the electrons determines the Fermi energy (chemical potential) then. The situation for the metallic TM/RE compounds can be described successfully by the picture at the right. By hybridization the bonding bands below and the antibonding bands above the Fermi level show a mixed character. The degree of 3d-5d character is visualized via the content of the areas. It is governed by the energetic distance of the bands: in the case of a small energy difference the mixing of the quantum states is stronger.

In figure 2.2 the situation of the magnetic compound is discussed. Due to the spin splitting in the case of a ferromagnetic TM, the distance of the energy levels will be different for the spin-up and spin-down bands. The distance between 3d-majority spins and RE-5d band is larger than the energy distance between 3d-
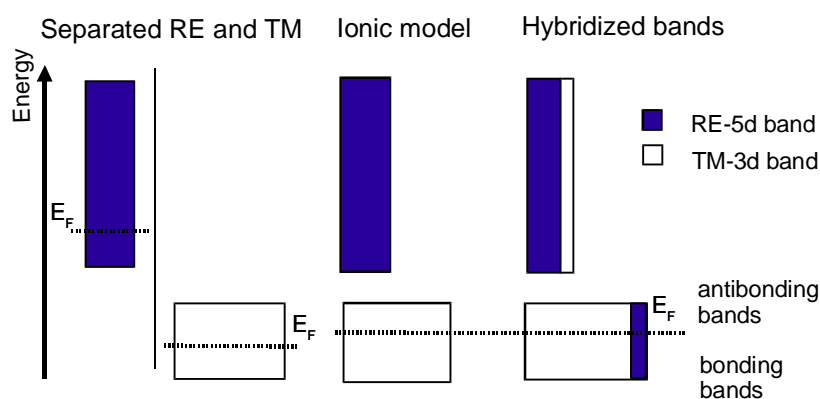

Figure 2.1. Model state densities (only d bands) for a TM-RE compound. On the left is the density of states for the separated metals, in the middle for an ionic and on the right for a metallic compound. On the right the situation for hybridized bands is shown. The character of the band is represented by the black and white coloring.
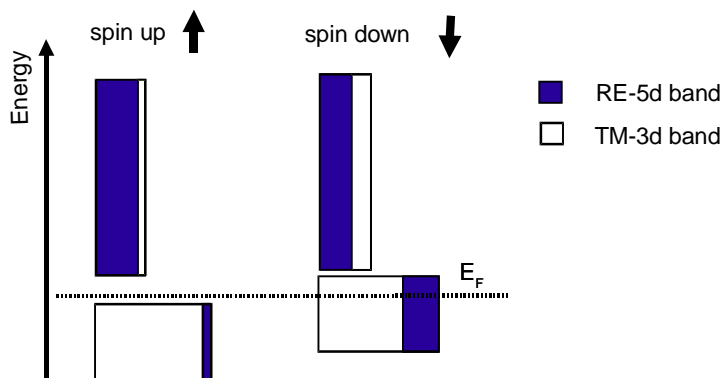
Figure 2.2. Spin up and spin down DOS for a saturated ferromagnetic situation. The degree of mixing differs for both spin orientations. The character of the band is represented by the black and white coloring.

minority spins and RE-5d band. Thus the mixing with the spin down electron states is stronger and as a result, for the majority bonding band there is a decrease of its 5d content. Hence the spin-up occupation of the 5d part becomes smaller than its spin-down occupation. This explains an antiparallel induced magnetic polarization on the RE-5d electrons with regard to the Fe.

For the compounds of Ce, which are related to the present work, the 4f states have to be included into the discussion. Their energy position is of particular importance. If they are situated between the bonding and the antibonding bands there is a little hybridization with the TM-3d states and the 4f states are localized. However, if the 4f states lie in an energy region with high 3d-state density, hybridization is important and may lead to a delocalization of the 4f-3d hybridized states. This is the case for $CeFe_2$ where the electronic configuration is α-like. Here the 4f states have to be included in the conduction band. The influence of the 4f-3d hybridization can be treated in the same way as the hybridization of the TM-3d and RE-5d band (figure 2.3). As a result, the induced magnetic moment on the
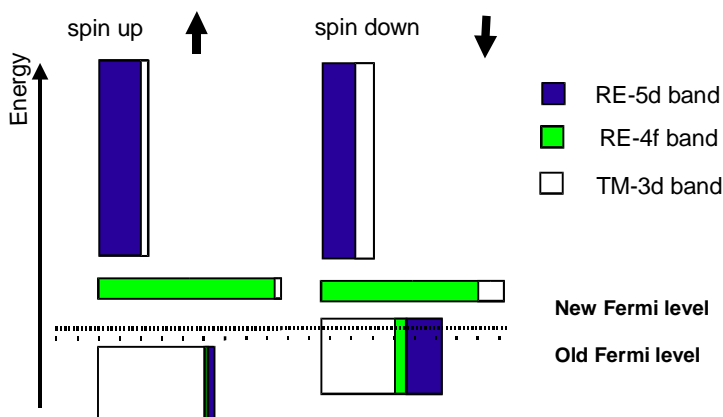
Figure 2.3. The same picture as shown in figure 2.2, but with the delocalized 4f-states in addition. The old Fermi level is the case for the localized 4f-electrons. The character of the band is represented by different gray scales.

4f-electron state is oriented antiparallel to the Fe magnetization. Second, the 4f-3d hybridization reduces the number of 3d spin up electrons and thus the magnetic moment on the Fe. The role of the itinerant 4f state can be clarified in this simple model qualitatively.

The localized 4f electron is the natural case for atomic-like radial 4f wavefunction. Then the magnetic polarization is governed by the intra-atomic magnetic exchange between 4f and 5d magnetic moments which is determined by the overlap of the 4f-spin and 5d-spin functions. This intra-atomic exchange forces the 4f- and 5d-spin moment to align parallel for all RE. The 4f-orbital moment is coupled to the 4f spin due to Hund's rule. A magnetic exchange interaction of the RE-4f moments between each other or of the RE-4f and the Fe-3d magnetic moment in a TM/RE compound can only be transmitted via indirect interaction, i.e. through the spin polarization of s or d conduction electrons. This spin polarization is known to oscillate and decreases with r^{-3} (distance r). The mechanism can be discussed in the RKKY-model (Ruderman-Kittel-Kasuya-Yosida).

The scheme for the different magnetic interactions, developed for the compounds, can be applied to the magnetic interaction at the TM-RE interfaces in the multilayer systems as well.

2.3 Introduction: XMCD

The first experiments which apply the element selective X-ray spectroscopy to investigate the magnetic properties of the electron valence states were done by G. Schütz et. al. [9] in 1988 using the photoeffect in the X-ray region. Before, she worked on radioactive nuclei in ferromagnetic host lattices proving the existence circularly polarized light in the radiation produced by sample inherent decay processes. A recently published review paper of Stöhr on the microscopic origin of the XMCD [10] will be shortly described here to discuss the basic phenomena and to give an introduction.

In X-ray absorption spectroscopy (XAS) the absorption $\mu(E)$, calculated as logarithm of the incoming intensity $I_0(E)$ in front of the absorber divided by the intensity $I(E)$ behind, is probed as a function of the energy E as it is defined (chapter 1.4, formula 1.2). In the single particle approximation the absorption is viewed as a excitation of a single electron: one electron absorbs the photon and is excited to a higher orbital as a result. For the RE, the electronic structure consists of the core levels 1s, 2s, 2p,.., 3d, and a valence band structure which is build up with a partial density of states with s, p, d, f symmetry. In the X-ray range, the absorption spectrum is characterized by a series of sharp steps. Each edge corresponds to the opening of an absorption channel, and the edges are identified with labels derived from their core-level designation: K, L, M, ... for core levels with the principal quantum number n=1, 2, 3,... .The spin of the hole left in the core level can be either parallel or antiparallel to the hole's angular momentum l,
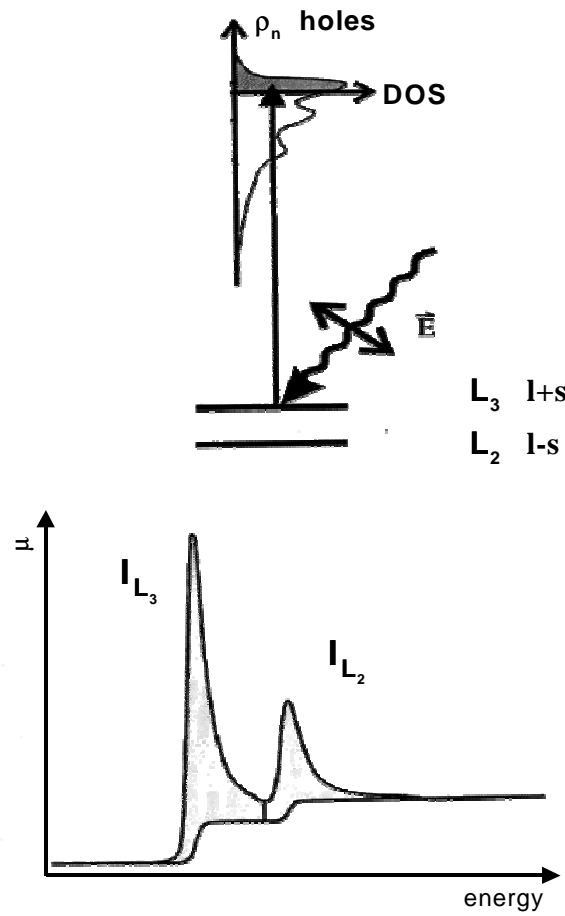
Figure 2.4. Transitions at the $L_{2,3}$ edges in a one-electron model: excitation of a photoelectron from the spin-orbit split 2p shell by a linearly polarized photon into the 5d-density of hole states. The sum of the white-line intensities I_{L3} and I_{L2} is proportional to the number of d holes [from reference 10].

leading to a difference in energy by the spin-orbit interaction of the core level. The XAS spectra from the core levels with $l \neq 0$ are therefore split in two parts, labeled as $L_{2,3}$ ($2p_{1/2}$, $2p_{3/2}$), $M_{2,3}$ ($3p_{1/2}$, $3p_{3/2}$), $M_{4,5}$ ($3d_{1/2}$, $3d_{3/2}$), ...

This is shown schematically for the L_3-absorption edge in figure 2.4 in the one-electron picture. For the specific energy of the L_3-absorption edge transitions

occur from the initial $2p_{3/2}$-core shell to the empty conduction-band states $\rho_n(E)$ above the Fermi energy. Thus, the absorption increases step-like, superimposed by a resonance with an enhanced absorption, called white line. The relation between the absorption $\mu(E)$ and density of hole states $\rho_n(E)$ is due to Fermis Golden Rule

$$\mu(E) = \omega\,\rho_n(E) \qquad\qquad 2.1$$

The transition probability ω depends on the overlap of wave functions of the core level state and valence state. Because of the preservation of the orbital moment, the orbital moment of the photoelectron has to change by $\hbar$. This is the first selection rule: the orbital moment l has to change by $\Delta l = \pm 1$. A change by -1 has a small transition possibility which is reduced by a factor ~20 compared to the change by +1. The initial s state probes the p states, transitions from the p states probe the d electron states and transitions with d initial states probe the f density of hole states. It results in the first sum rule: the intensity of the isotropic spectrum (the atomic absorption line) is directly proportional to the number of holes in the valence band.

2.4 XMCD and sign convention of the dichroic signal

The magnetic properties of the ferromagnetic TM are governed by the 3d valence electrons. These valence states are spin split due to the magnetic exchange interaction and the spin-magnetic moment m_S is given by the difference in spin-up $\rho_n^{\uparrow}$ and spin-down holes $\rho_n^{\downarrow}$: $m_S \sim \Delta\rho = \rho_n^{\uparrow} - \rho_n^{\downarrow}$. An orbital moment m_O arises from the spin-orbit interaction that is in the order of 50 meV. Both information are mirrored in the XMCD, that is calculated by the difference of the absorption for right circularly polarized light μ_+ and left circularly polarized light μ_- as defined in formula 1.3 (chapter 1.4).

The principle of the XMCD spectroscopy is to probe separately the spin-split hole densities with the excited photoelectron (figure 2.5). For the use of right (+ helicity) or left (- helicity) circularly polarized light, the angular momentum of the photon is parallel or antiparallel to the X-ray propagation direction and magnetization direction of the sample. Thus, right circularly polarized photons transfer the opposite moment to the excited electron as compared to the left circularly polarized light. The spin-orbit coupling results in different sign of
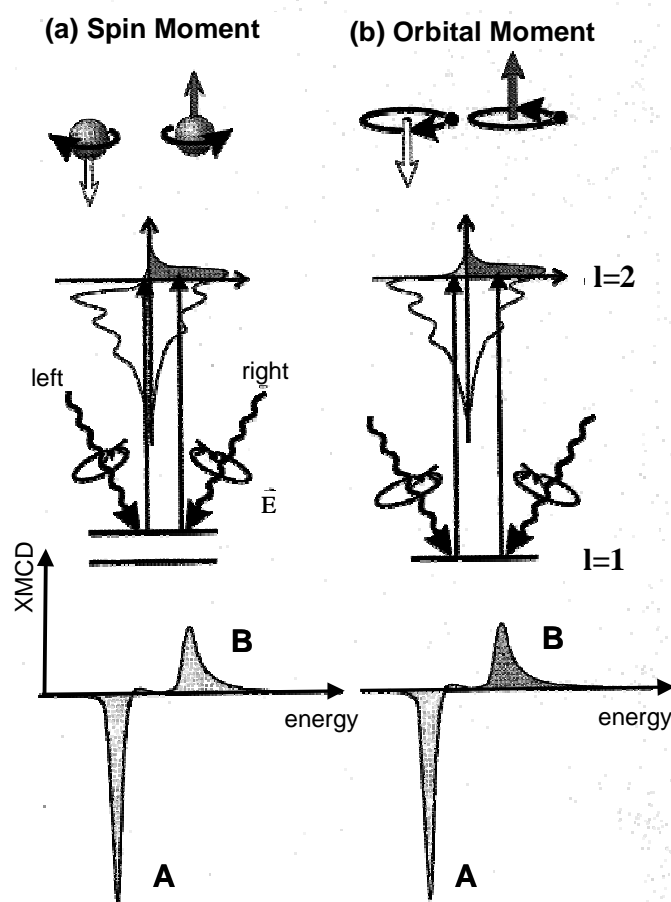

Figure 2.5. X-ray magnetic circular dichroism illustrated in a one-electron model. At the right the difference of the absorption for right and left circularly polarized light probes the spin moment (a) and orbital moment (b). The integrated intensities A and B determine the spin and orbital moment due to the sum rules [from reference 10].

l and s for the 2p core levels: l+s for the $p_{3/2}$-state and l-s for the $p_{1/2}$ state. Hence photoelectrons with opposite spins are created in the two cases. For the L_3 edge, a spin-up electron is excited with right circularly polarized light and results in the absorption μ^+, a spin-down electron is excited with left circularly polarized light and results in the absorption μ^-. The dipole selection rule for the spin conservation is $\Delta s = 0$. So in the case of a ferromagnetic transition metal magnetized parallel to the X-ray propagation direction, the difference $\Delta\mu = \mu^+ - \mu^-$ of $\mu^+ (\mu^-)$ probing $\rho_n^\uparrow (\rho_n^\downarrow)$ for the L_3 edge has a negative sign ($\Delta\rho_n = \rho_n^\uparrow - \rho_n^\downarrow < 0$). For the L_2 edge the dichroism has a positive sign, hence the quantity l-s is probed. The shape of the XMCD that is typically observed for Fe is shown in figure 2.5 at the bottom, where the integrated intensities at the L_3 edge is defined as A and as B for the L_2 edge. A and B will be used in the next chapter for qualitative analysis.

A change of the sign of the magnetic field is equal to a change of spin direction of majority and minority electrons and thus has the same effect as changing the helicity of the light.

2.5 Sum rules

Keeping this qualitative discussion in mind, it is possible to calculate the spin m_S and orbital moment m_O by taking the difference or the sum of the dichroic intensities at both edges. A tool for a derivation of the quantity is given by the sum rules calculated by Thole, Carra et. al. [11] for the atomic limit, and in a more elementary formalism by Altarelli [12].

The total angular momentum of the l-s coupled 2p state $|m_j\rangle = |m,s\rangle$ of the core electron is allowed to change due to the electric dipole selection rule by $\Delta j = \pm 1, 0$: $\Delta s = 0$ for the spin, the different Δm transitions are $\Delta m = +1$ and $\Delta m = -1$ for left and

right circularly polarized light and $\Delta m=0$ for parallel linearly polarized light. This is shown schematically in figure 2.6 for the L_3 edge [13]. The relative intensity for the transitions allowed is defined by the coupling of the photon momentum and the core-level electron. The strength of the transition is schematically represented by the arrow widths. Quantitatively, the transitions are plotted in a diagram in figure 2.7 [14].

In the upper panel the relative intensity is shown for the different momenta of the photon in the case of the L_3 edge. For left circularly polarized (LCP) light the -5/2 channel dominates, for right circularly polarized (RCP) light the 5/2 channel dominates. In the lower panel the sum LCP+Linear+RCP is plotted, which is proportional to the number of holes N and thus constant for all final states for the separated atom. The difference, which corresponds to the dichroism, depends
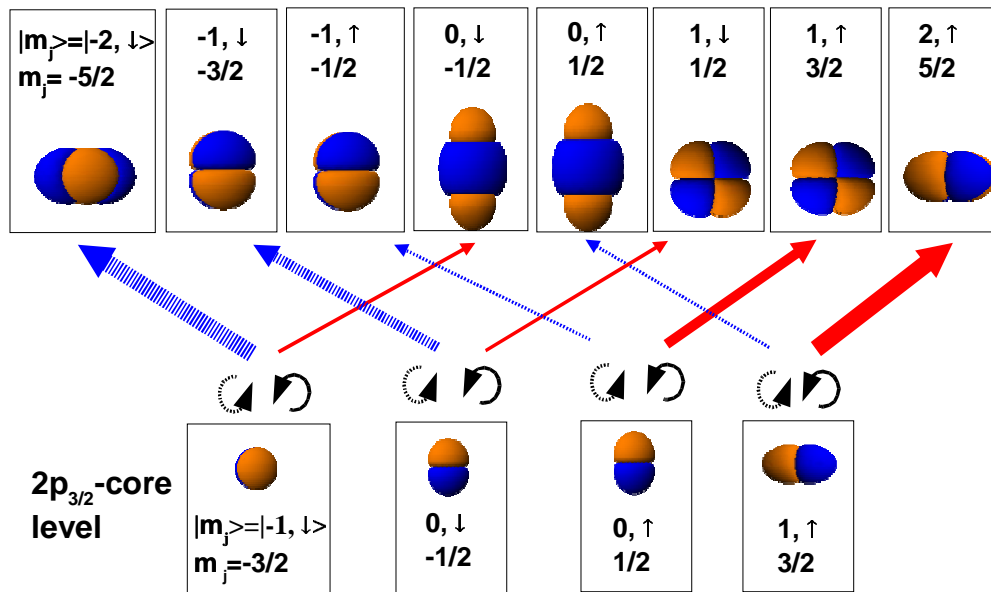
L_3 edge: d-valence level

Figure 2.6. Schematic diagram of the selectivity of the dichroic absorption at the L_3 edge. In the case of the incoming photon with helicity right (left), the transition rules allow only $\Delta m=+(-)1$ and $\Delta m=0$ for linearly polarized light (not shown). The orbitals are calculated with 'orbital viewer' [13].
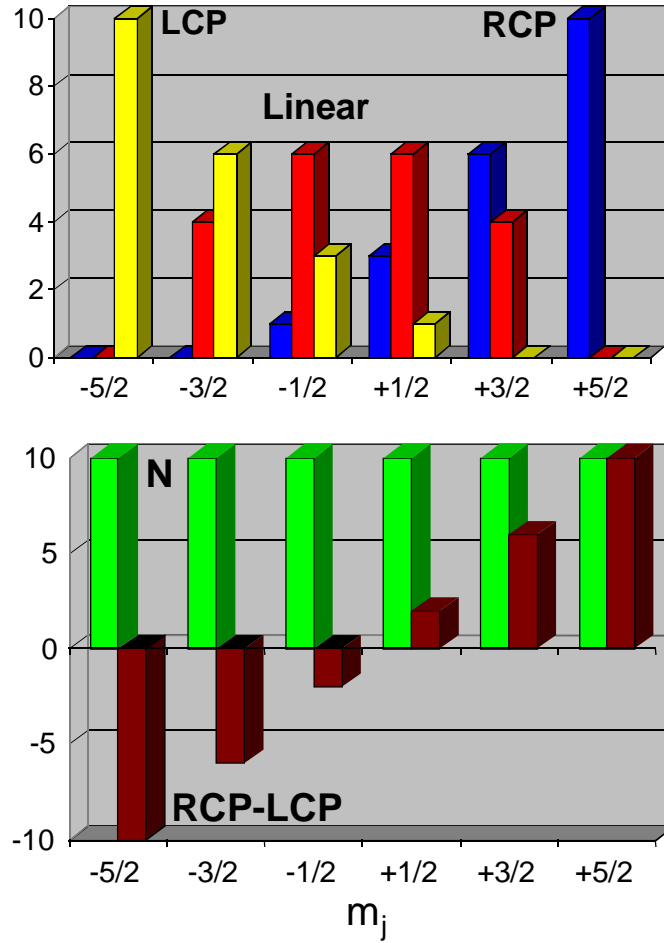
Figure 2.7. States probed with left polarized light (LCP), linearly polarized light and right polarized light (RCP) for magnetic valence levels m_j at the L_3 edge [14]. The highest value of $|m_j|$ has the strongest possibility for the circular polarization. In the lower graph the sum RCP+LCP+linear ~ N that is proportional to the number of holes N (first sum rule) and the dichroism RCP-LCP ~ m_j is plotted from the values above.

linearly on m_j of the valence state. Let us define the integrals of the XMCD A (at the L_3 edge) and B (at the L_2 edge) as drawn in figure 2.6. A and B have the opposite sign reflecting the opposite spin-orbit coupling. A sum rule links the spin moment to the measured intensity A-2B. If the valence shell possesses an orbital moment, it will act as an orbital momentum detector. By summing the intensities A (~l+s) and B (~l-s) the spin moment is eliminated.

Hence we have three sum rules.

$$[I_{L_3} + I_{L_2}]_\alpha = C(\rho_n + \rho_{n\,Q}^\alpha) \qquad\qquad 2.2$$

$$[A - 2B]_\alpha = \frac{-C}{\mu_B}(m_S + m_D^\alpha) \qquad\qquad 2.3$$

$$[A + B]_\alpha = \frac{-3C}{2\mu_B} m_O^\alpha \qquad\qquad 2.4$$

The first sum rule links the intensity of the white lines I_{L3} and I_{L2} with an isotropic hole term ρ_n and an anisotropic hole term $\rho_{n\,Q}^\alpha$, that depends on an angle α defined in figure 2.7 and reflects the anisotropy of the bondings and therefore anisotropic charge distribution. C is the square of the transition matrix element and is in the order of ~10 eV. The second sum rule, in principle, has the same form, with an isotropic spin term m_S and the anisotropic dipole term m_D^α (called $<T_Z>$ by other authors). The last sum rule links the sum of the dichroism to an angular dependent orbital moment m_O^α.

The angular-dependent charge distribution is reflected for example for d surface states. The orbitals that are generated in a cubic-symmetry crystal field differ in orientation: the d_{x2-y2} and d_{xy} orbitals are mainly in plane whereas the d_{3z2-y2}, d_{xz} and d_{yz} orbitals are mainly out of plane (see figure 2.8). Thus, by different occupancy of the orbitals at surfaces or interfaces, the number of hole states probed is angular dependent and is responsible for magnetic anisotropies as well.

The sum rules agree with the experiment only in the range of 10-20%. One problem is the consideration of a single ion (the atomic limit) for the calculation of the sum rules. A first attempt to include the electron-band states of solids was calculated by Benoist [15].

The general validation of the sum rules for the RE is not possible. There are

several problems that arise in the case of the RE-$M_{4,5}$ and RE-$L_{2,3}$ edges. In the single electron model, the core-electron is excited into the unoccupied continuum states of the system. The transition is viewed as taking place between the ground state and excited state of the separated atom. Additional corrections to the sum rule have to be included because of the discrepancy between the initial- and final-state picture. In the initial-states picture, an electron is excited and the transition probability and density-of-states is calculated with the wave functions before the disturbance by the photon. The relaxation and the new charge distribution in presence of the core hole is neglected. Thus the sum rules are not applicable straight forward in the case of the atomic-like 4f-final states at the RE-$M_{4,5}$ edges [16, 17]. Coulomb interactions in the 4f-shell and those between the 4f shell and the core hole as well as the spin-orbit coupling have to be included. Because of the localization of the 4f states, the effect of the band structure is negligible in this case. These atomic multiplett states can be calculated with Cowan's program [18]. Considering the applicability of the sum rules at the RE-$L_{2,3}$ edges, pre-edge features of the quadrupolar transitions and the dependence on the 2p-5d Matrix element on the orientation of the 5d moment and the 4f moment, thus the df-
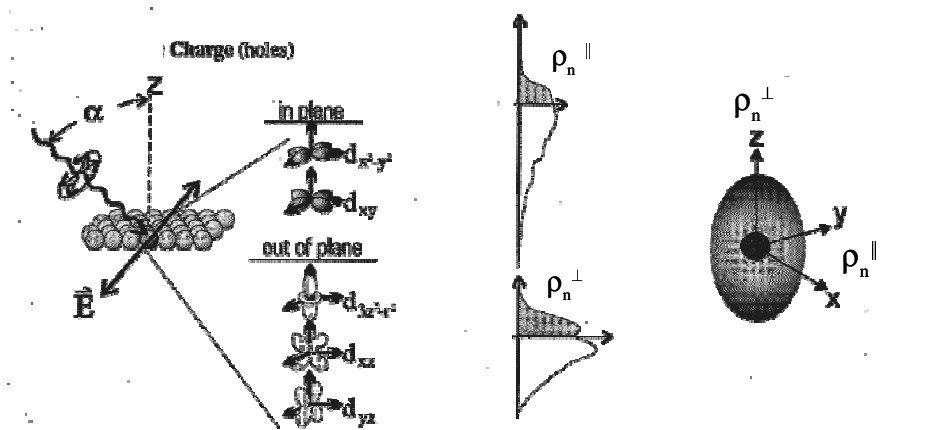

Figure 2.8. Schematic view of an atomic layer and symmetry of the d-electron orbitals on the left. On the right, the resulting number of steps for out-of-plane and for in-plane-states are drawn. This results in an anisotropy of the hole states ρ_n [from reference 10].

Coulomb interaction changes the spectra dramatically and will be discussed later on.

2.6 XMCD spectroscopy at the RE-L$_{2,3}$ edges

The electronic structure of the RE is characterized by the interaction between the electrons in the 4f orbitals and in the broad 5d band. In the Fe/REH$_X$-multilayer system, the magnetic polarization is induced into the non magnetic REH$_X$ sublayer by direct hybridization of the Fe-3d and RE-5d bands discussed in the model of Brooks in chapter 2.2. The induced magnetic polarization of the 5d valence band electrons results in a difference in spin-up and spin-down hole states $\Delta\rho_n$ in the ground state then. But the intensity measured in the XMCD spectroscopy at the RE-L$_{2,3}$ edges results not only from the polarization of the 5d-electrons in the ground state but also from a dependence of the 2p-5d matrix elements on the relative orientation of the 5d- and 4f-magnetic moment [19,20]. Therefore band effects and the Coulomb interaction between 4f and 5d states have to be included into the interpretation of the spectral line shape and the intensity ratios observed in the L$_2$/L$_3$-XMCD intensity ratios. There are three effects involved:

(1) the induced magnetic polarization of the ground state

(2) the intra-atomic df-Coulomb interaction and band effects that change the transition probabilities

(3) the pre-edge features arising from quadrupolar transitions [21], which are weak in the intensity of the absorption spectrum but can have a strong influence on the line shape of the XCMD-spectrum.

The interplay of (i) and (ii) was used to explain the L$_2$/L$_3$-intensity ratios of the XMCD that were observed especially in insulating compounds. The ratio is expected to be -2 in the case of the dipolar 2p→5d transitions, with negligible spin-orbit coupling in the final state and thus a negligible orbital moment of the
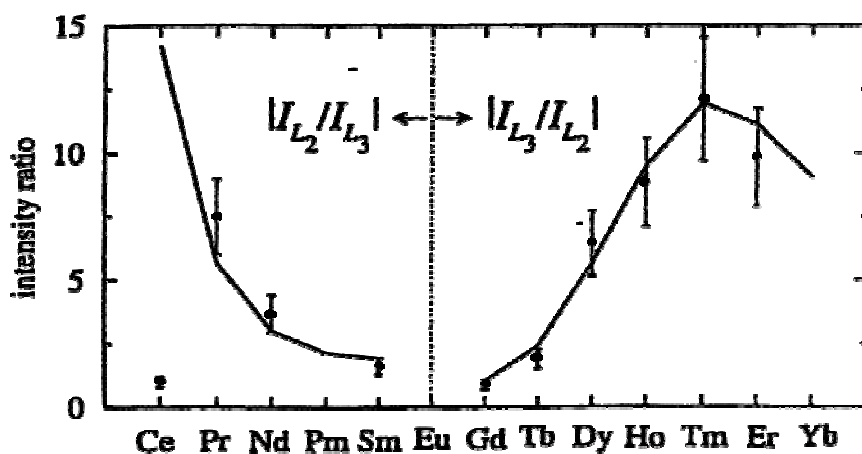
*Figure 2.9. Experimental |L₂/L₃|-XMCD intensity ratios for the light and the
reciprocal fraction for the heavy rare earth [27]. The solid line is obtained
by a calculation including the breathing effect by 4f-5d exchange
interaction [30,31]. The CeFe₂ compound is special since Ce has an α-like
electronic configuration with delocalized 4f-states*

valence states [22]. However, the observed values are quite different. A table of
experimental $I(L_2)/I(L_3)$-branching ratios is given for example in reference [23].
The ratios vary from <0.02 to 6 (Nd) and even 100 for Nd_2CuO_4 is reported. For
the Ce systems, the most prominent example is $CeRu_2Ge_2$ in the Ce^{3+} electronic
configuration, where the L_2/L_3 ratio is about 40 [24]. The ratio and XMCD spectral
shape is similar to the case of $Fe/CeH_{2-\delta}$ multilayers at low temperatures [25]. In
general an enhancement of the dichroic signal at the L_2 edge is observed for those
RE elements with a less than half-filled 4f shell. An enhancement of the XMCD at
the L_3 edge is observed for the RE elements with more than seven 4f electrons
[26]. This was systematically examined by Ch. Giorgetti for the intermediate
compounds $REFe_2$ and RE_2Fe_{17} [24,27]. The results are shown in figure 2.9. Note
that for the light RE, the ratio $|I(L_2)/I(L_3)|$ and for the heavy rare earth the ratio
$|I(L_3)/I(L_2)|$ is plotted.

The results gave rise to systematic theoretical investigation carried out in the
groups of Kotani (Tokyo) and Harada (Okayama) as well as of M. van Veenendaal

et al. at the ERSF (Grenoble) [28,29,30,31]. This led to a phenomenological model for the XMCD at the $L_{2,3}$ edges of the RE, with similar basic parameters. A rigorous theoretical description of the $L_{2,3}$ XMCD is not available, therefore this model will be used to analyze the experimental spectra of the multilayers. It will be simplified here by reducing the number of parameters to two. Since there is no unique terminology, the parameters will be denoted α and β[1]. The model takes into account the influence of the 4f electrons on the spectral shape of the XMCD at the $L_{2,3}$ edges by a modification of the transition probability, parameterized by α, and a spin splitting in energy, parameterized by β. A condition required for the application of the two parameter model is the effect of lifetime broadening of the core level. The white line can be described essentially by a Lorentzian then, as it will be discussed in detail in the next chapter.

2.7 The description of the white line

In the early period of X-ray spectroscopy the spectra were recorded with energy dispersive spectrometers on photographic films. The X-ray transitions from inner shells into the partially filled valence states exhibit sharp lines in analogy to the optical transitions. Therefore these intense excitations were called white lines. The core-hole lifetime depends on the relaxation process and results in a broadening of the white-line width by 3-5 eV in case of the RE-$L_{2,3}$ edges. The lifetime of the X-ray exciton is 10^{-15}-10^{-16}s in comparison to 10^{-12}s for the optical exciton. The effect on the spectral shape of the absorption edge observed is called lifetime broadening and is shown in figure 2.10.

Two schematic 5d density-of states (DOS), one rectangular and a more complex structure (a $\sin^2(E)$-function), with two different widths (3.5 eV and 4 eV), are convoluted with a Lorentzian with the width of $2\Gamma=4$ eV. A broadening of the 5d DOS results, for the simplified rectangular shape of the hole states at the top in
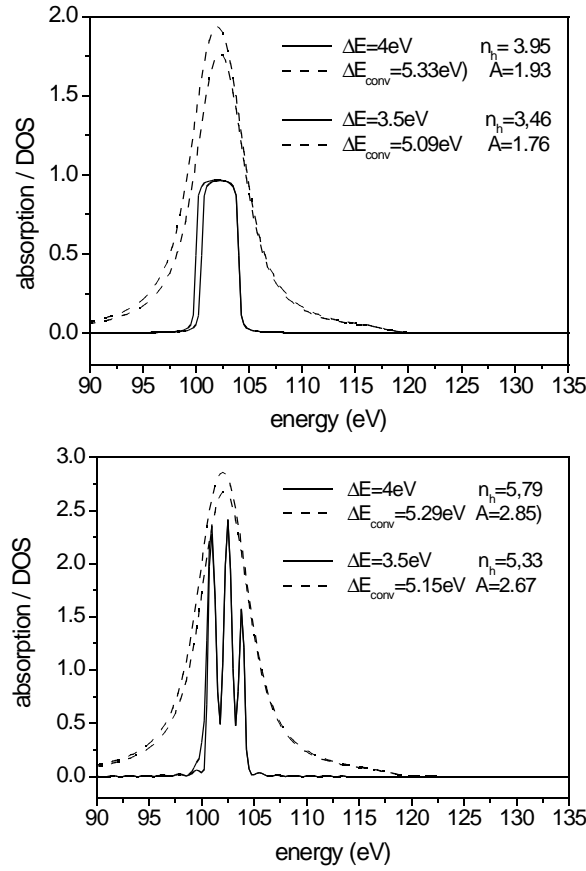
Figure 2.10. Effect of lifetime broadening on the white-line shape. At the top a simple rectangular 5d DOS with the width ΔE=4 eV and 3.5 eV is convoluted with the Lorentzian with 2Γ=4 eV. The results of the analysis are shown in the insets: n_h is the number of holes of the initial DOS (continuous line), $ΔE_{conv}$ and A are the width and the amplitude of the resulting white line (dashed line).

figure 2.10, in an increase of the white line, but due to a broadening of the DOS, the increase of the white line height alone does not reflect the total increase of the number of holes. The parameters are given in the inset. The more realistic 5d DOS, with the same difference in width is convoluted with the same Lorentzian function (figure 2.10, bottom). Here, the increase of the white line does not reflect the full increase of the number of holes, either. This is due to a change in width of the resulting curve. The number of holes is proportional to the total spectral

weight $A_L \cdot 2\Gamma$, where A_L is the amplitude and 2Γ the width of the resulting Lorentzian. The shift of the maximum in energy that is observed for the rectangular shape is a factor two smaller than the shift of the initial 5d DOS. The resulting white line structure can be analyzed or described with multiplett lines that are convoluted with a Lorentzian function. So it should be sufficiently accurate to analyze the white line resonance with a Lorentzian L(E) description with the amplitude A_L and width 2Γ. The position in energy is given by E_0.

$$L(E) = A \left(1 + \left(\frac{E - E_0}{\Gamma} \right)^2 \right)^{-1} \qquad\qquad 2.8$$

This approach is discussed in detail by Röhler [32] and can be applied very successfully to mixed valent systems [33]. In essence, one can simplify the analysis of the $L_{2,3}$ edge resonance in a first quantitative approach with a Lorentzian function. With keeping this knowledge in mind it is possible to study the difference of the white lines measured for left and right circularly polarized light by taking the difference of two white lines (Lorentzians) respectively.

2.8 The α-β-model

2.8.1 The parameter α

The parameter α is introduced in order to explain the anomalous enhancement of the XMCD at the L_2 edge for the light and the L_3 edge for the heavy RE, which was discussed in chapter 2.6. To give an idea, the effect ('breathing' effect) already mentioned can be explained very shortly: the probability for the 2p→5d electric dipole transition is proportional to the overlap of the 2p initial-state and 5d-radial function in *real space*. The 4f-5d exchange splits the spin bands radially with the result, that the band with the spin parallel to the 4f spin is contracted at the

positions of the 2p orbitals. In this way a spin dependence is introduced in the transition matrix element for the transitions of the spin-up (spin-down) state, $M^{\uparrow}(M^{\downarrow})$.

The effect was observed first by Harmon and Freeman [19]. They calculated the spin polarized 5d-valence band of Gadolinium by the augement-plane-wave method. The case of Gadolinium is special because of the 4f moment, which is essentially a spin moment. The authors conclude from their calculations that the 5d spin-up electrons experience a net exchange attraction by the spin-up 4f electrons that pulls them radially inwards. The spin-down radial function of the 5d states has a zero exchange interaction with the 4f electrons in Gd and hence is not affected. This is clearly seen in figure 2.11 for the calculation in the atomic case: the spin-up radial function is less extended. The difference between the spin-split radial function is marked in the overlap region with the 4f orbital.
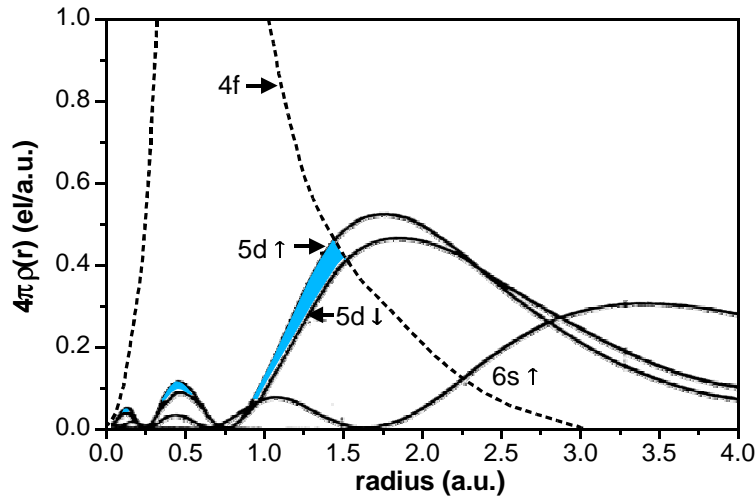

Figure 2.11. Calculation of the spin-split 5d wavefunctions [19]. The 5d band is spin split because of the 4f-5d interaction: the spin-up radial function is contracted whereas the spin down-radial function is not affected.

A qualitative approach introducing the enhanced transition probability is given by Lang et. al. [34] and Galéra et al. [35]. To the lowest approximation the XMCD measured can be written essentially by a combination of the difference of the matrix elements, $\Delta M = M^{\uparrow} - M^{\downarrow}$ and the difference in the density of hole states, $\Delta \rho_n = \rho_n^{\uparrow} - \rho_n^{\downarrow}$ that will be defined as the 'effective' polarization α.

$$\alpha \equiv \frac{M^{\uparrow} \rho_n^{\uparrow} - M^{\downarrow} \rho_n^{\downarrow}}{M \rho_n} \qquad\qquad 2.9$$
$$= \frac{1}{2}(\frac{\Delta M}{M} + \frac{\Delta \rho_n}{\rho_n})$$

$\Delta \rho_n$ is in the range of a few percent at the $L_{2,3}$ edges of the RE-$L_{2,3}$ edges, whereas ΔM can rise to 20-30 % [34]. The magnitude scales with the 4f-spin momentum and thus it largest for Gd among the RE. A net moment oriented parallel to the X-ray propagation direction should result in a negative sign of the XMCD at the L_3 edge as discussed in chapter 2.3 ($\Delta \rho_n$ is negative). Hence the XMCD may be essentially determined by ΔM, the sign of the XMCD is just reversed due to an enhancement of $M^{\uparrow}$. More general, this means that a transition to a band with fewer unoccupied states may produce a larger absorption due to the stronger transition probability. This is shown schematically in figure 2.12.

In the Fe/GdH$_X$ multilayer system at room temperature the GdH$_X$ sublayer orders not magnetically itself. Here the difference $\Delta \rho_n$ is positive since the 5d-RE magnetic moment is coupled antiparallel to the 3d-Fe moment at the interface. The 5d spin function, which is parallel to the 4f spin, is contracted and the $M^{\downarrow}$ matrix element is enhanced, thus ΔM is negative.

The 'breathing effect' can be generalized to the full 5d-4f Coulomb interaction in the final state including the 4f-orbital momentum into the calculation. Van

Veenendaal et al. [30] find that the L_2/L_3-XMCD intensity is proportional to the 5d-4f Coulomb interaction which varies across the RE series and differs strongly at the L_2 and L_3 edges. Their result approaches the trends of the variation of the XMCD signals at the L_2 and L_3 edges observed experimentally (figure 2.9).

More in detail, the group of van Veenendaal states that the extreme ratios observed can be understood by assuming a mixing of d states with different n [30]. The mixing results in an effective radius reduction by the 'breathing effect'. They calculate the interaction strength by 5d-4f Slater exchange integrals and obtain the result that the interaction couples electrons which differ by $\Delta j=0, \pm 1$. Thus the strength of the breathing for the same 4f moment is different at both edges: in the case of the L_3 edge, the $5d_{5/2}$ states are probed and thus the interaction term is
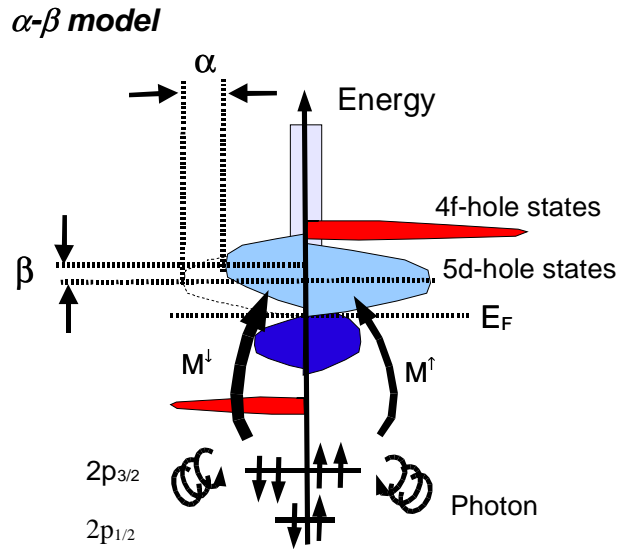
Figure 2.12. Schematic viewgraph of the α-β model. The essential information of the XMCD signal consists of the lifetime broadened white line with an amplitude A_L and a width 2Γ. It can be essentially simulated with two Lorentzian functions, one for the white line for spin-up holes, one for the spin-down holes, which have a difference in the relative amplitude, α, and shifted in energy, β. α appears as the effective polarization.

strong with $4f_{7/2}$ state. At the L_2 edge, the $5d_{3/2}$ state is probed and thus the interaction term is strong with $4f_{5/2}$ and zero with an $4f_{7/2}$ electron. In general, the interaction is small for states that do not have their spin and orbital moment coupled in the same way $j=l\pm s$, which explains the observed trend quite satisfyingly.

2.8.2 The parameter β

The parameter β reflects a splitting in energy of the 5d spin-up and spin-down states. In opposite to the contraction of the radial wave function in real space this is a shift in the *k-space*. The factor β explains the dispersive line shape visible in the spectra of several, essentially insulating RE compounds [31]: the difference of two Lorentzian L(E) that are shifted in energy by a value β is derivative-like, $(L(E)-L(E-\beta))/\beta \sim dL(E)/dE$, if β is small in comparison to the halfwidth 2Γ.

The final state configurations of the $2p{\to}5d$ transitions $2p^{\downarrow}4f\,^{n\uparrow}5d^{\downarrow}$ and $2p^{\uparrow}4f\,^{n\uparrow}5d^{\uparrow}$ differ in energy through the $2p$–$4f$ and $5d$–$4f$ exchange interactions of the final state. Multiplett calculations of Goedkoop et al. [31] predict a $\mp(\pm)$-dispersion at the $L_2(L_3)$ edge [24]. This is in agreement with their data and can be explained by an opposite sign of the photoelectron at both edges.

We then arrive at the following formulas for fitting the dichroic signals $\Delta\mu_C$ at the $L_{2,3}$ edges as a function of the energy E:

For the L_3 edge it results in

$$\Delta\mu_C(E, A_L(\alpha), 2\Gamma(\beta)) = L(E, A_L, 2\Gamma) - L(E-\beta, A_L(1-\alpha), 2\Gamma+\beta) \qquad 2.10\,a$$

and because of the reversed sign of the spin of the photoelectron for the L_2 edge
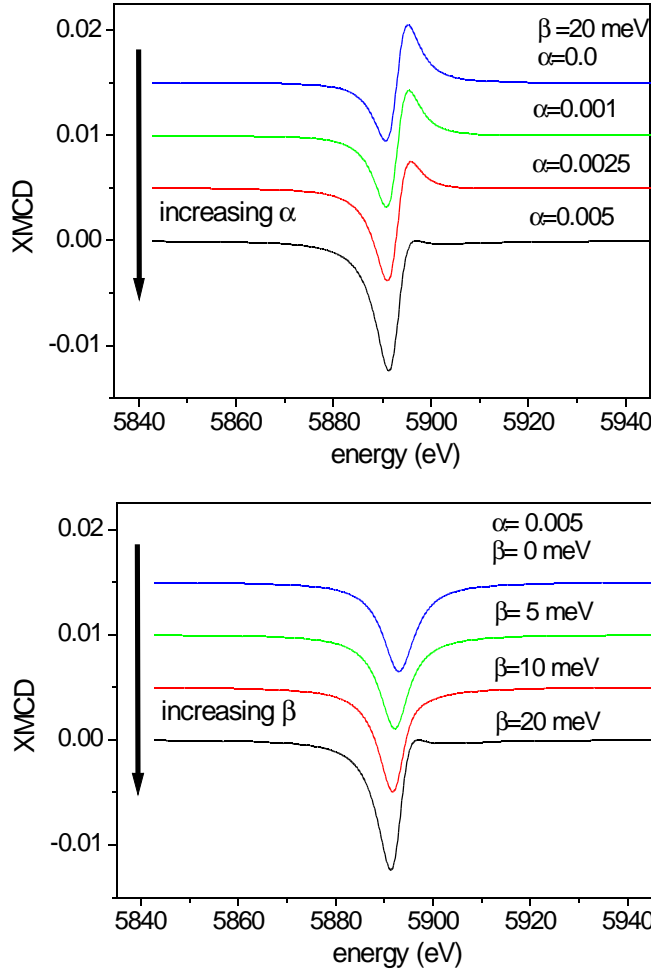
Figure 2.13. Effect of the parameters α and β. At the top β and at the bottom α is kept constant. For a strong α value the white line is mirrored, in the case of the strong β the XCMD gets derivative like. The curves are calculated with the parameters for the La-L$_2$ edge.

$$\Delta\mu_C(E, A_L(\alpha), 2\Gamma(\beta)) = -L(E, A_L, 2\Gamma) + L(E-\beta, A_L(1-\alpha), 2\Gamma+\beta) \qquad 2.10\,b$$

The two Lorentzian in equation 2.10.a,b describe the white-line resonances for the two spin orientations. Thus the shape of the Lorentzians is governed by the amplitude A_L and $A_L\cdot(1-\alpha)$, and the widths 2Γ and $2\Gamma+\beta$. A_L and 2Γ are known from the absorption spectra. The two parameters that diminish the shape of the

XMCD $\Delta\mu_C(E)$ are the parameters α and β, representing the difference in amplitude and the energy shift for the two spectra. Note that the modification of the white-line width by $2\Gamma+\beta$ for one kind of spins is included for the case of La and Gd, but not for Ce.

The effect of the interplay of α and β is shown in figure 2.13 for a set of parameters, starting with pure-derivative like curve with $\alpha=0$ for the first case at the top and with a pure mirror of the white line with $\beta=0$ at the bottom. The parameters are varied gradually up to the dichroic signal with the parameters $\alpha=0.005$ and $\beta=20$ meV in both cases. The range of $\Delta\mu_C$ is in the order of 1%.

1   See *Handbook on the physics and the chemistry of the Rare Earths*, edited by K.A. Gschneider, Jr. and L. Eyring (North Holland, Amsterdam, 1978), Vol. I

2   O. Eriksson, R. C. Albers, A.M. Borning, G. W. Fernando, Y. G. Hao, and B. R.Cooper, Phys. Rev. B **43**, 3137 (1991)

3   D. Gustafson, J. McNutt, and L. O. Roellig, Phys. Rev. **183**, 435 (1969); U. Kornstädt, R. Lässer, and B. Lengler, Phys. Rev. B **21**, 1898 (1980)

4   Ch. Giorgetti, S. Pizzini, E. Dartyge, A. Fontaine, F. Baudelet, C. Brouder, Ph. Bauer, G. Krill, S. Miraglia, D. Fruchard, and J.-P. Kappler, Phys. Rev. B **48**, 12 732 (1993)

5   J. P. Schillé, F. Bertram, M. Finazzi, C. Brouder, J.-P. Kappler, and G. Krill, Phys. Rev. B **50**, 2985 (1994)

6   J. Trygg, J. M. Wills, B. Johansson, and O. Eriksson, Phys. Rev. B **50**, 4200 (1994)

7   M. S. S. Brooks, et al., J. Phys. Condens. Mater **1**, 5661 (1989), M. S. S. Brooks, Physica B **172**, 95 (1991); B. Johansson, L. Nordström, O. Eriksson, and M. S. S. Brooks, Physica Scripta **T 39**, 100 (1991); M. S. S. Brooks and B. Johansson, in *Handbook of Magnetic Materials*, edited by K. H. J. Buschow (North Holland, Amsterdam, 1992), Vol. 7, p. 139

8   O. Gunnarson and K. Schöhammer, in *Handbook on the physics and chemistry of the rare earths*, edited by K. A. Gschneider jr., L. Eyring, S. Hüfner (North Holland, Amsterdam, 1987), Vol. 10, p. 103

9   G. Schütz, W. Wagner, W. Wilhelm, P. Kienle, R. Zeller, R. Frahm and G. Materlik, Phys. Rev. Lett **58**, 737 (1997)

10   J. Stöhr, J. Magn. Magn. Mater. **200**, 470 (1999)

11   B. T. Thole, P. Carra, F. Sette, G. van der Lahn, Phys. Rev. Lett. **68**, 1943 (1992), P. Carra, B. T. Thole, M. Altarelli, X. Wang, Phys. Rev. Lett. **70**, 694 (1993)

12   M. Altarelli, Phys. Rev. B **47**, 597 (1993)

13   'orbital viewer' written by David Manthey 1997, http://www.orbitals.com/orb

14   H.A. Dürr, private communication

16   J. Goedkoop, Thesis, University of Nijmegen (1989)

17   M. van Veenendaal, R. Benoist, Phys. Rev. B **58**, 3741 (1998)

18   R. D. Cowan, *The Theorie of Atomic Spectra* (University of California Press, Berkeley, 1981)

19   B. N. Harmon, A. J. Freeman, Phys. Rev. B **10,** 1979 (1974)

20   X. D. Wang, T. C. Leung, B. N. Harmon, and P. Carra, Phys. Rev. B **47**, 9087 (1993)

21   P. Carra, M. Altalrelli, Phys. Rev. Lett. **64**, 1286 (1990)

22   J. L. Erskine, E. A. Stern, Phys. Rev. B **12**, 5016 (1975)

23   D. Watson, E.M. Forgan, W.J. Nutall, W.G. Stirling, Phys. Rev. B **53**,726 (1996)

24   F. Baudelet, Ch. Giorgetti, S. Pizzini, Ch. Brouder, E. Dartyge, A. Fontaine, J. P. Kappler and G. Krill, J. Electron Spectrosc. Relat. Phenom. **62** (1993) 153

25   M. Arend, PhD thesis, Universität Göttingen (1998); M. Arend, W. Felsch, G. Krill, A. Delobbe, F. Baudelet, and E. Dartyge, J.-P. Kappler, M. Finazzi and A. San Miguel-Fuster, S. Pizzini and A. Fontaine Phys. Rev. B **59**, 3707 (1999)

26   J. P. Hill, A. Vigliante, D. Gibbs, J. L. Peng, and R. L. Greene, Phys. Rev. B **52**, 6575 (1995)

27   Ch. Giorgetti, PhD thesis, Univ. de Paris-Sud (1994)

28   T. Jo and S. Imada, J. Phys. Soc. Jpn. **62**, 3721 (1993)

29   H. Matsysama, I. Harada, A. Kotani, J. Phys. Soc. Japan **66**, 337 (1997), H. Matsuyama, K. Fukui, H. Maruyama, I. Harada, A. Kotani, J. Magn. Magn. Mater. **177-181**, 1029 (1998)

30   M. van Veenendaal, J. B. Goedkoop, and B. T. Thole, Phys. Rev. Lett. **78**, 1162 (1997)

31   J. B. Goedkoop, A. Rogalev, M. Rogaleva, C. Neumann, J. Goulon, M. van

32   J. Röhler, in *Handbook on the physics and chemistry of the rare earths*, edited by K. A. Gschneider jr., L. Eyring, S. Hüfner (North Holland, Amsterdam, 1987), Vol. 10, p. 453

33   M. Arend, PhD thesis, Universität Göttingen (1998), O. Schulte, PhD thesis, Universität Göttingen (1996)

34   J. C. Lang, X. Wang, V. P. Antropov, B. N. Harmon, A. I. Goldman, H. Wan, G. C. Hadjipanayis, K. D. Finkelstein, Phys. Rev. B **49**, 5993 (1994)

35   R. M. Galéra, S. Pizzini, J. A. Blanco, J. P. Rueff, A. Fontaine, Ch. Giorgetti, F. Baudelet, E. Dartyge and M. F. López, Phys. Rev. B **51**, 15957 (1995); J. P. Rueff, R. M. Galéra, S. Pizzini, A. Fontaine, L. M. Garcia, Ch. Giorgetti, E. Dartyge, F. Baudelet, Phys. Rev. B **55**, 3063 (1997)

3. Metal-to-insulator transition in Fe/REH$_X$ multilayers: measurement of the interface polarization with XMCD

For the RE-hydrides (REHx), a metal-to-insulator transition is observed by increasing the hydrogen concentration towards the trihydride (x=3). The metal-to-insulator transition in RE-hydrides is a nice object for studies: a fundamental change of their electronic properties can be induced simply by variation of the hydrogen concentration. Here the modification of the magnetic polarization of the interface in multilayers of REH$_X$ (RE: La, Ce) with Fe will be studied across this transition by XMCD measurements. For this, the H concentration in the RE hydride multilayers is gradually increased, starting from the as prepared dihydride REH$_{2-\delta}$. The α-β model presented in chapter 2.8 will be used as a tool to extract the characteristic parameters. In the case of the Fe/GdH$_X$ multilayers, the antiferromagnetic order observed at 20 K is studied for different hydrogen concentrations x. At first, theoretical aspects and the band structure will be discussed in chapter 3.1-3.3.

3.1 The metal-to-insulator transition

The metal-to-insulator transition in REH$_X$ can be seen in some nice experiments directly, if a thin REH$_X$-film is charged in an hydrogen atmosphere of about 1 to 1000 mbar. The film changes from metallic reflecting to transparent for the visible light. The process can be reversed by pumping the surrounding hydrogen atmosphere. The effect is known as 'switchabel mirror' and has been observed at first in the group of Griessen [1]. They are in collaboration with Philips [2], who plan to construct new optical switching elements using this novel technique.
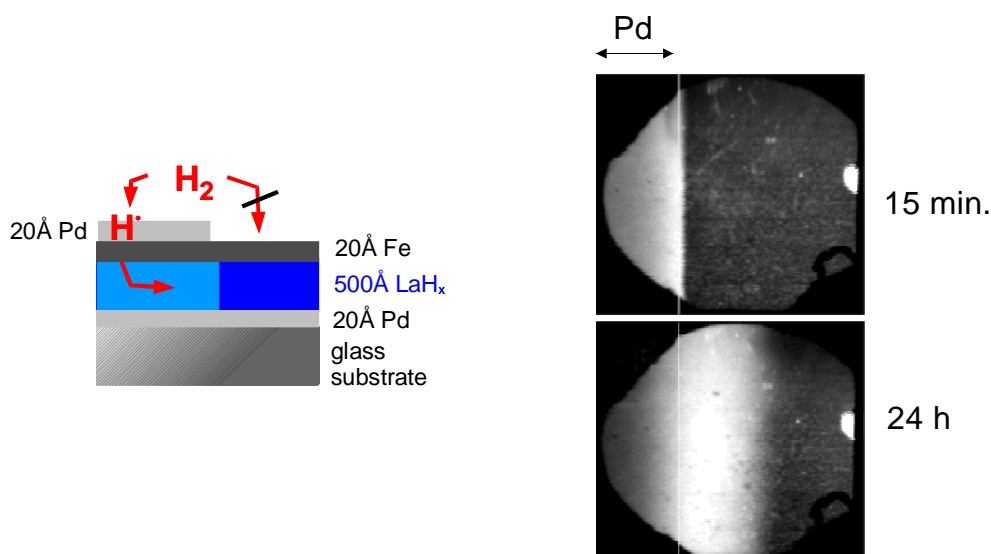
Figure 3.1. Left: schematic profile of the sample. A LaH$_X$-thin film is sputtered on the glass substrate, covered with Fe film as protection layer and coated at one side with Pd on the top. Right: the transmission in the visible light is shown measured with a CCD-camera with a diffuse light source at the back of the sample, after charging in a hydrogen atmosphere of 100 mbar H$_2$ for 15 min and 24 h respectively [3].

Figure 3.1 describes an experiment performed in our laboratory [3]. At the left the profile of the thin film sample is shown. The LaH$_{2-\delta}$ film prepared by reactive sputtering is in the metallic phase and so reflecting. Only one side is covered with Pd. The Pd cover layer cracks the surrounding molecular H$_2$ and transfers atomic H to the LaH$_{2-\delta}$ film. The optical transmission of the thin film is studied with a CCD-camera. As H diffuses into the part of the LaH$_{2-\delta}$ covered with Pd, the metal-to-insulator transition is directly observable by the transmittance of the light. After 24 h the diffusion front has proceeded into the Fe-covered part on a length of about 2 mm, and a diffusion profile is visible in form of a brightness contrast. By the use of this experimental setup the diffusion constant can be studied. Some more elaborate electromigration experiments reveal the bare nature of the H ion inside the REH$_X$ [2]: the charge is negative due to strong correlation effects. This supports the recent theories of the metal-to-insulator transition in these systems as it will be discussed later on.
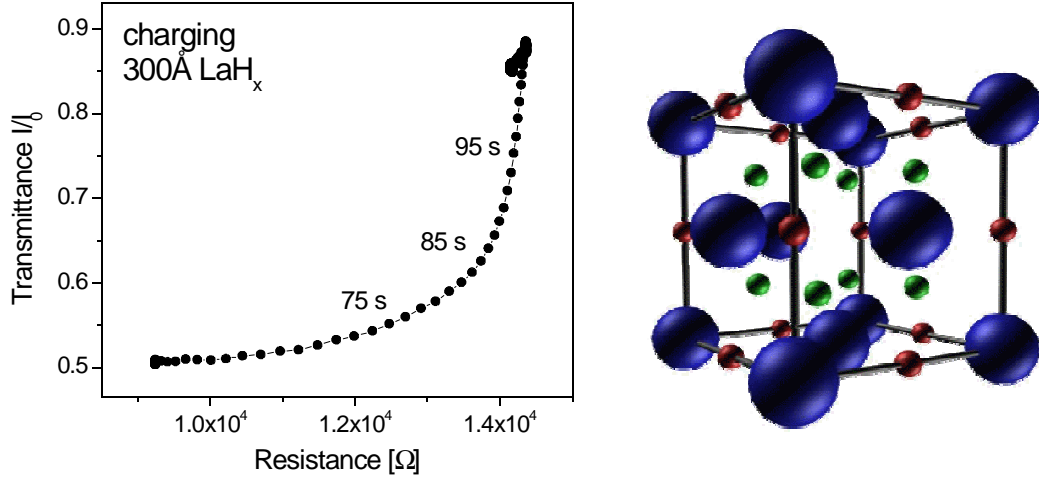
Figure 3.2. Left: charging process for a 300 Å thick LaH$_x$ film. The transmittance is shown as a function of the change of the resistance. Right: LaH$_X$ lattice with interstitial sites occupied by the H (small spheres).

The metal-to-insulator transition has a dramatic influence on the conductance as well, that decreases of over three orders of magnitude [1]. In figure 3.2 the transmittance of a He-Ne-laser beam through a 300Å thick LaH$_X$ layer is plotted as a function of the resistance. The charging process at 100 mbar takes about 25 s. At first the resistance is increasing. Subsequently the transmittance changes rather sharp while the resistance stays almost constant. The time scales vary somewhat for different samples. They depend on the hydrogen pressure, the thickness of the Pd and LaH$_X$ layers and on the surface quality of the PdH$_X$.

The dramatic difference in the physical properties is a result of the change in the electronic structure with transition from the dihydride REH$_2$ phase to the trihydride REH$_3$ phase. The first direct measurements of the electronic density of states have been performed by Peterman et al. [4]. They studied the electronic structure of LaH$_X$ in the composition range $1.9 \leq x \leq 2.9$ with photoelectron spectroscopy in the energy range of $10\,\text{eV} \leq h\nu \leq 50\,\text{eV}$. They observed a gap of 2 eV in the trihydride which, for a long time, was not reproducible by classical band structure

calculation methods that do not include electron correlation effects.

3.2 Crystal structure of the RE hydrides

The phase diagram of the REH_X is given in figure 3.3. For the light RE shown in the left diagram, the crystalline structure is in general fcc, it does not change with the hydrogen concentration. The solubility of hydrogen in the RE is generally very low (α-phase). For higher concentrations the hydrogen occupies the tetrahedral sites in the crystal structure, which are all occupied in the dihydride REH_2 (β-phase). The lattice constant for the pure rare earth is smaller and increases within the REH_2 phase by 10% (example: La(fcc): 5.30 Å, LaH_2(fcc): 5.67 Å, Ce(fcc): 5.14 Å, CeH_2(fcc): 5.57Å).

With further charging the trihydride REH_3 is reached (γ-phase) in which the additional hydrogen is located on the octahedral sites. Here the lattice does not expand anymore. The lattice constant of the trihydride is slightly smaller than that of the dihydride. For the heavy RE the situation is more complicated due to the
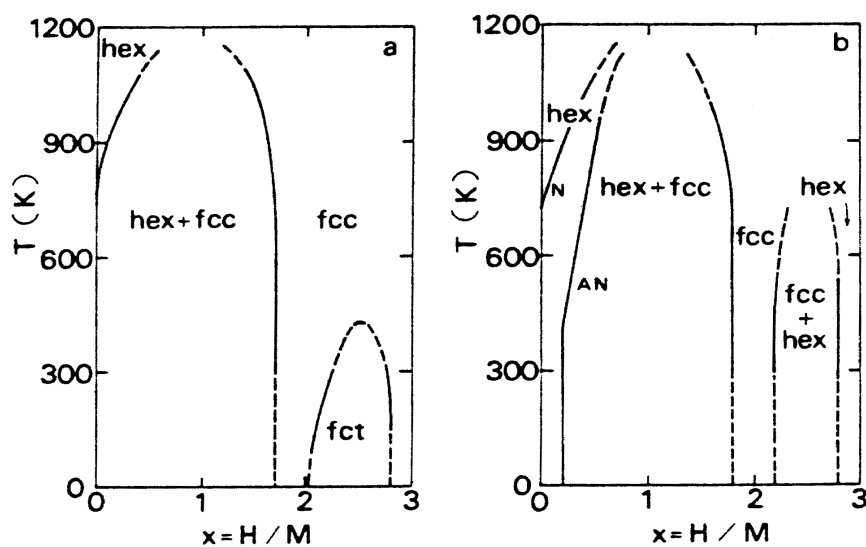

Figure 3.3. Diagram of the different structural phases for the light RE at the left and for the heavy RE at the right.

drastic changes of the crystalline structure with the hydrogen content. As a reference see for example [5,6].

3.3 Band-structure calculations

Calculations of the electronic structure of the RE hydrides, which are consistent with the insulating properties, in particular with the bandgap of ~2eV of the trihydride, have to take the strong electron correlations into account.

In principle this problem is well known for the transition metal oxides e.g. CoO or La$_2$CuO: they are not metallic as expected from classical mean field band structure calculations. The simple overlap of the electron orbitals in a crystalline lattice does not include the strong electron correlations that suppress the charge fluctuations required for a metallic character as it is discussed in [7].

The first calculations for La hydride by Gypta and Burger [8] using the augement-plane-wave method (AWP [9]) without taking into account electron correlation effects revealed a gap of 0.5 eV, that was too small compared with the experimental values. Selfconsistent calculations of Misemer and Harmon [10] did not show the true bandgap, either. But they discussed a charge transfer to the H 1s orbitals which is responsible for the different electronic properties, qualitatively: Lanthanum has the valence configuration 5d^{1}6s^2. In LaH$_X$ bands form with s-like or d-like character. The orbitals at the La site split into the triplett t$_{2g}$ and the doublet e$_g$ orbitals in the cubic crystal symmetry. In the case of the dihydride LaH$_2$, there are two bands below the Fermi level. They are composed essentially of states with s-like character on the tetrahedral hydrogen sites and d orbitals with t$_{2g}$ symmetry on the La site that point along the [111] axis towards the tetrahedral hydrogen places. All s electrons are bound by the hydrogen, leaving one electron in the bands of primarily La-d character. The Fermi energy is within the La-5d conduction band and the material is metallic. In the case of the trihydride, with the

occupation of the octaheadral sites by hydrogen, a third band forms below the Fermi level. This band consists predominately of s and La-e_g orbitals, since the e_g orbitals point towards the [100] directions in which the octahedral sites are located.
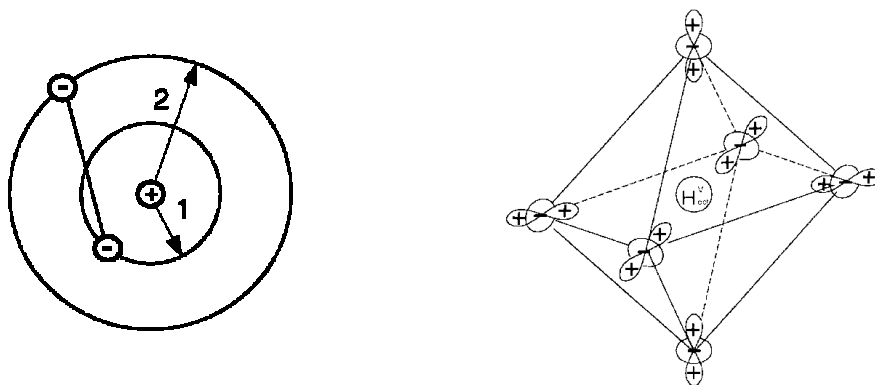

Figure 3.3. Left: the electron correlation of the H⁻-ion, two electrons bound to a proton. Right: La-5d-e_g orbitals surrounding the octahedral place. They point toward the octahedral H-vacany place.

The effect on the electron correlations was introduced recently by Ng et. al. [11] into the calculations of La hydride as a prototype of this systems and have improved the theoretical understanding considerably. The authors have developed a many-body theory based on a H⁻-ion electron correlation. Each proton located on an octahedral place is surrounded by two correlated electrons (figure 3.3). The calculations reveal that LaH_3 may be viewed as a Kondo insulator, with each H atom binding two electrons in a local unit cell, one primarily on the H orbital and one the neighboring La orbitals. This special correlation is stabilized by the surrounding t_g orbitals pointing towards the octahedral site. LaH_3 may be viewed as a band insulator owning strong electron correlations that open a gap between H⁻ derived valence band and the metal-like conduction band as well. The gap calculated is in agreement with the experiments [4].

The metal-to-insulator transition in the substoichiometric phase $LaH_{3-\gamma}$ takes place when the highly localized states centered at the H vacancies start to substantially
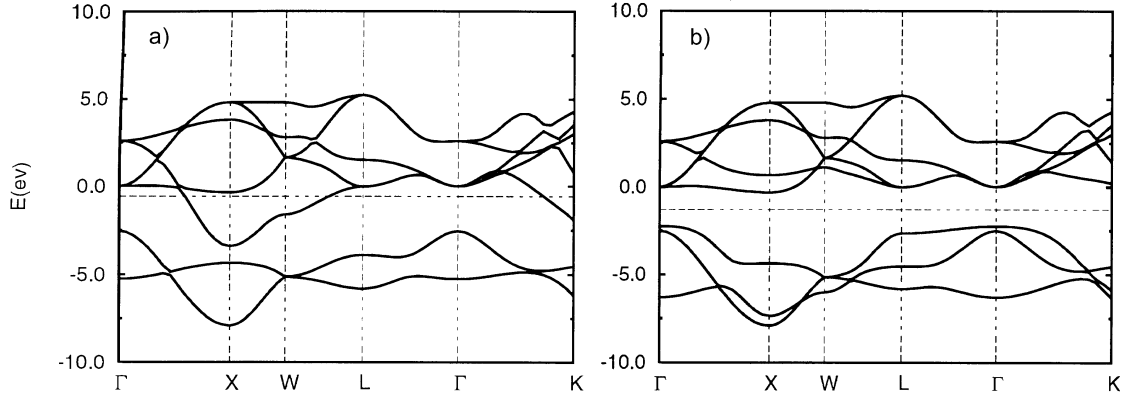
Figure 3.4. Band structure calculation (s and d bands) by Ng et. al. [11] for LaH$_X$ with x=2 for a) and x=3 for b).

overlap with each other for $\gamma \sim 0.25$. Thus a consistent picture of the electronic band structure has emerged for this hydrides by now (figure 3.4), that is in reasonable agreement with photoemission spectroscopy [4].

A similar theoretical approach by Eder [12] based on a Kondo-lattice-like effect yields essentially to the same results. The authors show that the key aspect is related to the large change in the H 1s orbital radius upon occupation with one or two electrons. It is translated into an electron-electron correlation, a strong occupation dependent hopping process that results in the formation of a local singlet-like bound state, involving one electron of the hydrogen and one of the surrounding metal orbitals. This means that the ground state of the trihydride corresponds closely to that of a Kondo insulator.

Quite generally, this anionic model of the hydride is consistent with electromigration experiments which found a negative charge for the diffusing H-species [2] as already pointed out above.

3.4 Chemical structure of the multilayers Fe/REH$_{2-\delta}$

The magnetic properties of a material are closely related to its structure. For the multilayers this information is obtained measuring the X-ray diffraction at large angles, which yields the crystal structure of the sublayers and at low angles, which yields the quality of the interfaces (roughness, interdiffusion) and the bilayer thickness (chapter 1.2). Results are presented in figure 3.5 and 3.6. The thickness of the multilayer stack is ~4000 Å for all samples.

The crystal structure of the REH$_{2-\delta}$ and Fe sublayers is quite similar for the three multilayer systems (figure 3.5). All REH$_{2-\delta}$ layers grow in a fcc structure with (111) texture, i.e. with their densest plane in the layer plane. The REH$_{2-\delta}$ -crystallite peaks are visible up to the 3rd order. The Fe layers grow in bcc structure with (111) texture. This is unusual since the densest plane for this structure is the (110) plane. This orientation is stabilized by the small mismatch of the lattice parameters at the interfaces which amounts only a few %. The width of the Bragg peaks gets sharper with increasing the thickness of the REH$_{2-\delta}$ layers. The crystallite size in the growth direction agrees with the sublayer thickness.

The small-angle X-ray reflection spectra of the multilayer structures are shown in figure 3.6. The solid lines are fits to the measured reflectivity profiles with the program of de Haan [13]. The chemical periodicity Λ can be determined with an error <0.5 Å. The deviation of the layer thicknesses from the nominal ones are below 1 Å, except for the GdH$_{2-\delta}$ sublayers with a deviation below 2 Å. The interfacial roughness extracted by the fit of the small-angle reflectivity is 3.0-3.5 Å for RE=Gd and 2.0-2.5 Å for RE=La and Ce. Thus, the roughness is below one monolayer. Oscillations from the small-angle region modulate the first order peak REH$_{2-\delta}$(111) and are observed especially for the thicknesses REH$_X$=50 Å.
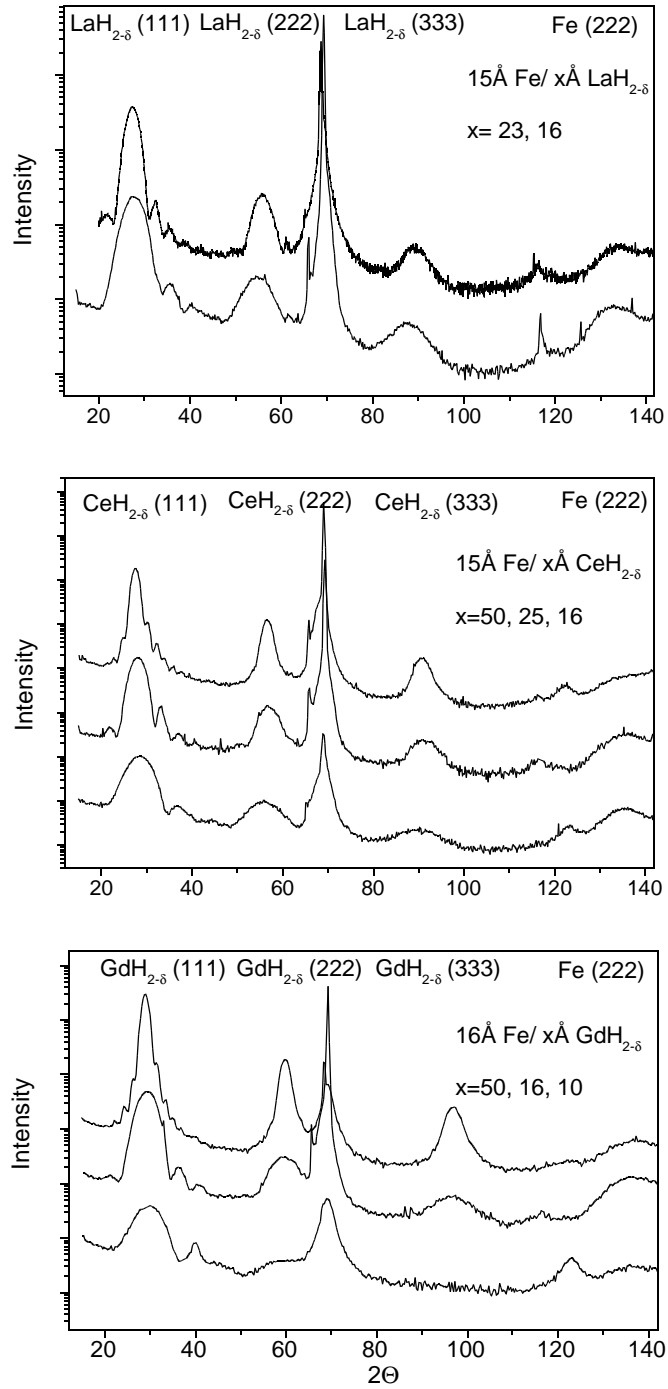
Figure 3.5. X-ray high-angle diffraction spectra of the Fe/REH$_X$ multilayers with fixed Fe thickness. Even for a small thickness of a few monolayers a crystalline structure is observed.
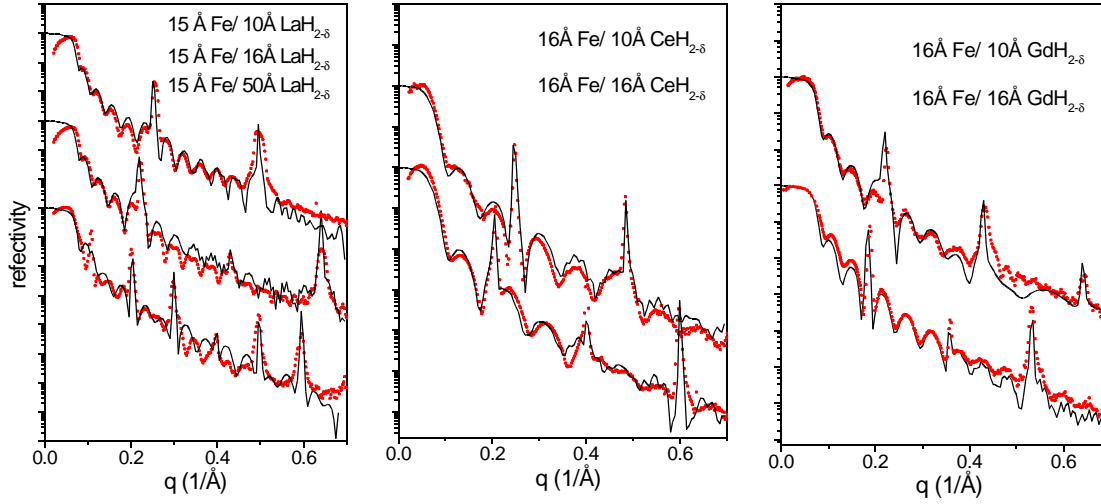
62

Figure 3.6. Small-angle X-ray diffraction spectra for the different Fe/REH$_X$ multilayers. The data are shown by small circles, the solid line is a fit with the de Haan program [14]. Sharp peaks of the chemical superstructure are visible even for small bilayer thicknesses of Λ= 26Å. The number of bilayer repetitions is 150 (Λ=26Å), 125 (Λ=32Å) and 62 (Λ=55Å).

By additional hydrogen charging only minor structural changes are observed. The change of the lattice parameter is below the instrumental resolution. In the small-angle limit, the data for a Fe/LaH$_X$ multilayer reveals a small increase of the interfacial roughness by 0.2(1)Å [14].

3.5 Conduction measurements on the Fe/REH$_X$ multilayers: evidence for the metal-to-insulator transition

It is important to demonstrate that the isolating state is reached in the REH$_X$ constituents of the multilayers by increasing the hydrogen content towards the trihydride even for REH$_X$ films thinner than a few nm. This is ascertained by measurements of the conductance.

Experiments on a single LaH$_X$ film have shown that information is difficult to obtain for the current-in-plane (CIP) geometry [3]. For LaH$_X$ thicknesses below 500 Å, the current is carried by the Pd seed and cover layers. Second the

roughness of the LaH$_X$ film changes with its thickness if it exceeds 150 Å. Thus the conductance of the LaH$_X$ film cannot be separated unambigously. A better choice would be a current-out-of plane geometry for the conductivity measurement. But for this case the film structure has to be in the submicron size for a measurable voltage drop on 20Å thick LaH$_X$ layer and therefore has to be patterned by lithography. In the case of the measurement of the optical transmittance, the effect of the Pd cover and buffer layer can be substracted very well. The metal-to-insulator transition is clearly observed for LaH$_X$ films thicker than 50 Å. Changes of the transmission coefficient range from 0.1 to 0.7 [3].

In principle, the problems are very similar for conduction measurements on multilayers using the CIP geometry. But due to the total thickness of 4000 Å of the multilayer stack, the influence of the Pd cover and buffer layers is controllable. The experiments do not reveal the absolute values of the conductivity but provide the trend. In particular, the conductance of the REH$_X$ layers should decrease less with increasing hydrogen content in the hypothetical case that an interfacial region dissolves less hydrogen.

Plotted in figure 3.7 is the evolution with time of the multilayer conductance normalized by the initial value for different LaH$_X$-layer thicknesses and steps of hydrogen charging. Starting from the as-prepared samples with LaH$_{2-\delta}$, hydrogen is introduced into the chamber in steps of 1, 10, 100 and 1000 mbar as in the dichroism measurements later on. At each pressure charging is performed during 8 min. Then the chamber is evacuated to investigate the reversibility of the hydrogenation process. Three points are of special interest: the charging time until the insulating state of LaH$_X$ is reached, the change in the conductance and the outgassing process.

At the highest H$_2$ pressure (1000 mbar) it can be assumed that the insulating state of the RE hydride is reached. Extrapolation of the graphs in figure 3.7 for the
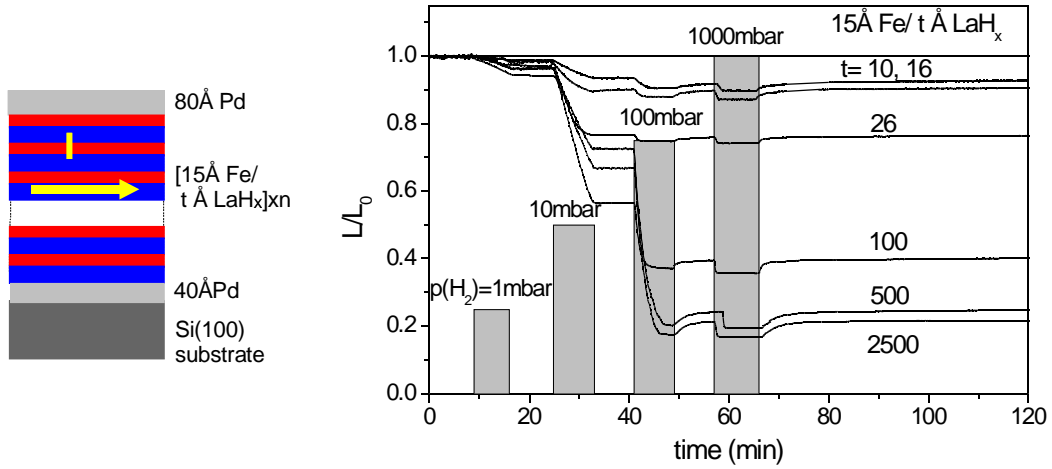
Figure 3.7. Measurement of the conductance on Fe/LaH$_X$ multilayers with fixed Fe-layer thickness in the current-in-plane geometry (left). The conductances L are normalized to the initial value L$_0$ prior to hydrogen charging and plotted for different LaH$_X$ thicknesses t as a function of the time (right). The filled curve represents the H$_2$ charging steps (as described in the text).

conductance values at 1000 mbar results in the relation plotted in figure 3.8 which shows the charging time to reach the isolating state in LaH$_X$ for the different charging pressure on a double logarithmic scale. If the charging pressure increases by a factor of ten, the charging time decreases by one order of magnitude. These values depend on the surface properties of the samples. A transmission experiment on a stepped sample, i.e. with a step-like increase of the LaH$_x$ thickness in one direction and a step-like increase of the Pd-cap layer thickness in the orthogonal direction, revealed that the charging time depends on both thicknesses. Another critical parameter is the reactivity of the Pd layer which is indispensable for oxidation protection and hydrogen charging: it may be covered with adsorbates which impede the catalytic functionality.

To analyze the change in conductance of the multilayers observed by charging at 1000 mbar H$_2$ to saturation (figure 3.8, bottom), one can take the bulk conductance
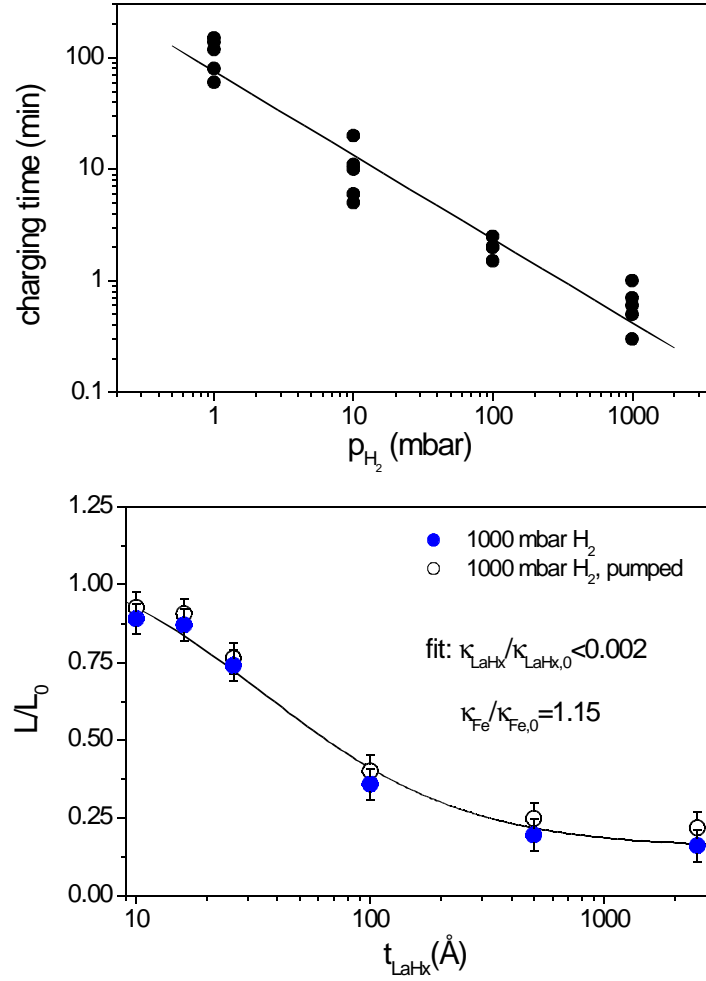
Figure 3.8. Charging time to reach the isolating state plotted as a function of the H$_2$ pressure (top). Note the logarithmic scales. At the bottom, the change in conductance is plotted, normalized to the initial value. Filled circles are with 1000 mbar H$_2$ atmosphere, the open circle represent the non reversible part.

values of the elements for a rough estimation. The specific conductivity behaves like $\kappa_{Fe} : \kappa_{La} : \kappa_{Pd}$ to 10:1:10. This means that if in the insulating state the LaH$_X$ layer ceases to contribute to the conductance of a Fe/LaH$_X$ multilayer the overall conductance in CIP geometry would decrease by $1/11 \approx 9\%$ for a thickness ratio t_{Fe}:t_{LaHx} of 1:1. In the case of a thickness ratio of t_{Fe}:t_{LaHx} of 15:500 the conductance decrease would be $50/65 \approx 77\%$. In fact this is observed in the measured

conductance data in figure 3.7.

The values shown in figure 3.8 are fitted by the simple relation

$$\frac{L}{L_0} = \frac{\sum t_i \kappa_i}{\sum t_i \kappa_{i0}} \qquad\qquad 3.1$$

where κ_{i0} and κ_i are the conductivities of the multilayer constituents in the as prepared state and in a H_2 atmosphere of 1000 mbar. The fit yields a decrease in the conductance ratio of the LaH_X layer by hydrogen charging to a value lower than 0.002. This means, an increase of the resistance of at least a factor of 500, which indicates that the LaH_X layers become insulating. Note that for a better fit of the data an increase of the Fe-layer conductance by a factor of 1.15 has to be assumed which may indicate an interface effect. The metal-to-insulator transition occurs even in the thinnest LaH_X layer of only 10 Å even at the interface: if not the conductance ratio L/L_0 should get to one. As it can be seen in figure 3.8, the decrease in the conductance of the Fe/REH_X multilayers measured for the thinnest REH_X layers is always about 10 to 15 %.

Additional information about the interface properties can be extracted from the outgassing process: a typical example for the thicker REH_X layers is shown at the top in figure 3.9 which presents the temporal evolution of the resistance of the multilayer [30Å Fe/ 23Å CeH_X]x40. As in the case of the LaH_X samples, the metal-to-insulator transition is observed between 10 and 100 mbar. The change in the resistance is about 14% which is expected for the Fe/REH_X thickness ratio of about one. Apparently no hydrogen is dissolved at 1 mbar H_2 pressure which indicates the influence of the surface condition. If the decrease of the resistance after pumping the H_2 at 1000 mbar from the charging chamber is fitted with a sum of exponential decays, it is possible to extract different time scales on which the
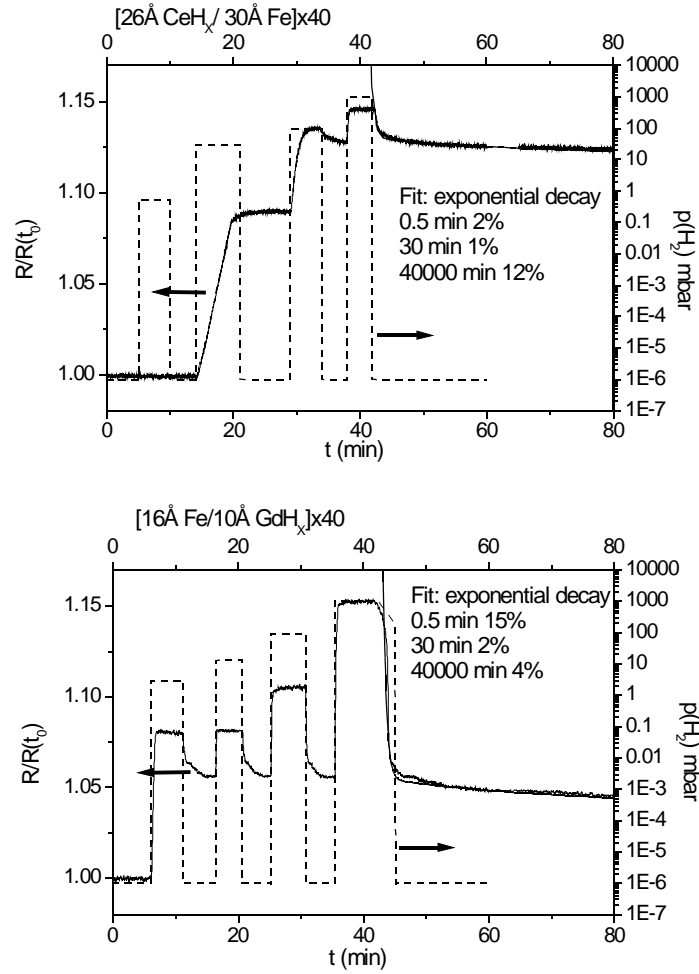
Figure 3.9. Charging process for two multilayers, Fe/CeH$_X$ at the top and Fe/GdH$_X$ at the bottom. The charging pressure is shown with the dashed line. A fitting with multiple exponential decay functions allows to determine the outgassing time scales. The fitting values are given in the inset of the layer.

outgassing takes place: two fast processes within 0.5 and 30 min with to 1% and 2% contributions and a long-time contribution extended over ~4·10^4 min or 28 days with a contribution of 12% change in the resistance. Thus, the main contribution is not reversible on a long time scale. For the sample [16Å Fe/ 10Å GdH$_X$]x40 (figure 3.9, bottom) the reversible part is much higher. If one takes into account the interface roughness of 3Å rms this corresponds to 1.5-2 Å at each

interface of the 10 Å GdH_X layer. This effects about 40% of the whole layer thickness. It seems that this intermixed or rough interface region can be charged to the metal-to-insulator transition, but if the chamber is evacuated, the decharging process is fast for the interfacial region that contributes with 17% to the change in resistance and only 4% change of resistance contributes with the longer timescale.

Concerning the sensitivity of the interfaces of the REH_X sublayers to the concentration of hydrogen at the interfaces, the number of non occupied octahedral sites in the trihydride can be quite large before the material becomes metallic. The metal-to-insulator transition occurs at x~2.8 [6]. A closure of the gap at the interface of the trihydride due to interfacial stress can be excluded. In the case of the $Fe/CeH_{3-\delta}$ interface, for example the misfit is 3% ($a_{Fe(222)}$=0.828Å, $a_{Ce(222)}$ =1.609) which may lead to a compression 0.972. For this values the gap is only slightly reduced [12]. The effect of a charge transfer at the interfaces will be discussed in the next chapter.

3.6 Metal induced gap states

The second effect, concerning the contribution of the Fe/REH_X interface to the conductance, besides a lack of stoichiometry due to structural changes at the interfaces, is the introduction of metal-like states into the energy gap of the insulator at the metal/insulator interface [15]. They determine the position of the Fermi level and the offset of the conduction and valence band (corresponding to a Schottky contact). These evanescent states decrease exponentially from the interfaces, in analogy to the exponentially decreasing states calculated for a simple well potential with a height which is higher than the Fermi energy. Thus, in the band structure at the interface, imaginary k states have to be considered. Butler et al. calculated the electronic structure of Fe/Ge/Fe and Fe/GaAs/Fe layers [16].

They find a charge transfer from the Fe to the Ge and a small magnetic polarization (<0.07 μ_B). The DOS of the majority electrons for 5 layers of Ge rapidly decreases but is still significant in the middle of the Ge layer. For neither of the spin-channels they observe a gap. They claim that the gap can be underestimated by the calculation technique used (local spin density approximation).
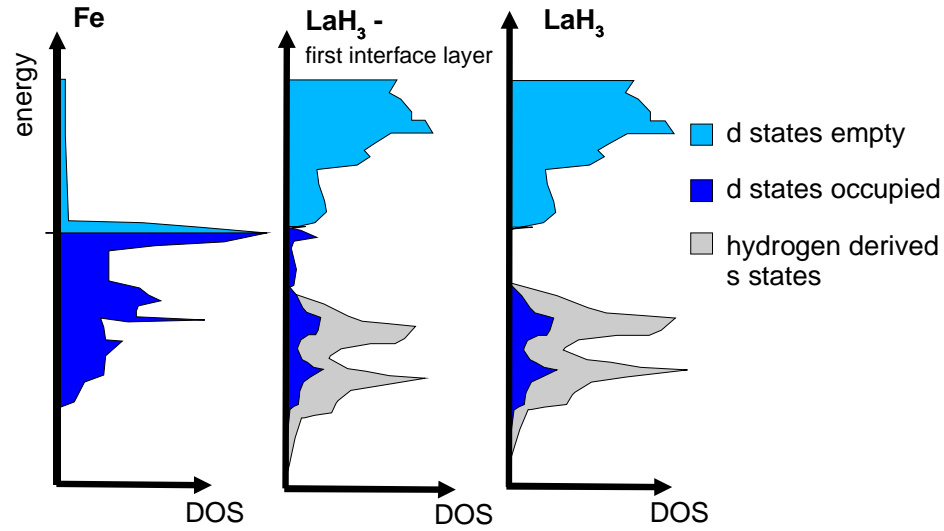

Figure 3.10. Schematic density of states for Fe [17], first insulating interface layer, and LaH$_3$ from Mismer and Harmon [10] (with correction of the band gap).

Stoeffler et al. [18] calculated the nature of the electron states injected into the band gap of the insulator, their spin-polarization, and the depth of penetration of the metal-like electron states into the barrier for the metal/oxide superlattice Co/Al$_2$O$_3$. They observe spin polarized states in the band gap for the first oxide layer that decrease exponentially.

The situation of metal induced gap states for the Fe/LaH$_{3-\gamma}$ interface is shown in figure 3.10. However, in the case of the REH$_{3-\gamma}$, the impurity rate (concentration

of H vacancies γ) can be quite high before a closure of the energy gap is observed: even for a concentration $\gamma=0.25$ the insulating character is preserved because of the strong localization of the vacancy states. In contrast, in doped semiconductors an increase of the conductivity is observed for 10^{-3} P-impurity states introduced in Si.

3.7 Change of the white line: discussion for the LaH$_X$ and CeH$_X$ sublayers

From the first sum rule one expects that the number of hole states in the 5d band of the RE is reflected in the white-line intensity. The increase of the hydrogen concentration leads to a charge transfer from the 5d-t$_g$ orbitals to the hydrogen derived bands which increase the number of 5d holes. On the other hand the opening of the gap of 2 eV at the metal-to-insulator transition must not be reflected necessarily in a shift of the white line due to its strong broadening by the core-hole as it is discussed in chapter 2.7 more in detail.

The white-line is estimated by the deconvolution of the absorption spectra in a lifetime broadened step function (arctan) and a Lorentzian according to the model of Röhler [19]. An example is shown in figure 3.11 for the lower two spectra, the Fe/La and Fe/Ce multilayer (dotted lines). A general trend is observed. The analysis results in a white-line amplitude of 0.85 for the 30Å Fe/ 60Å La multilayer. For the dihydride in the 15Å Fe/ 100Å LaH$_{2-\delta}$ multilayer the white-line amplitude is ~1.5 and increases to ~1.7 for the trihydride 15Å Fe/ 100Å LaH$_{3-\gamma}$ multilayer. These values are directly proportional to the number of 5d hole states because of the constant width 2Γ of the Lorentzian. The case of the Ce and its hydrides is plotted at the right. Ce is a special case since in these multilayers the electronic structure changes from an α-like configuration for the pure metal, indicated by the two-peak configuration in the absorption spectra to a γ-like
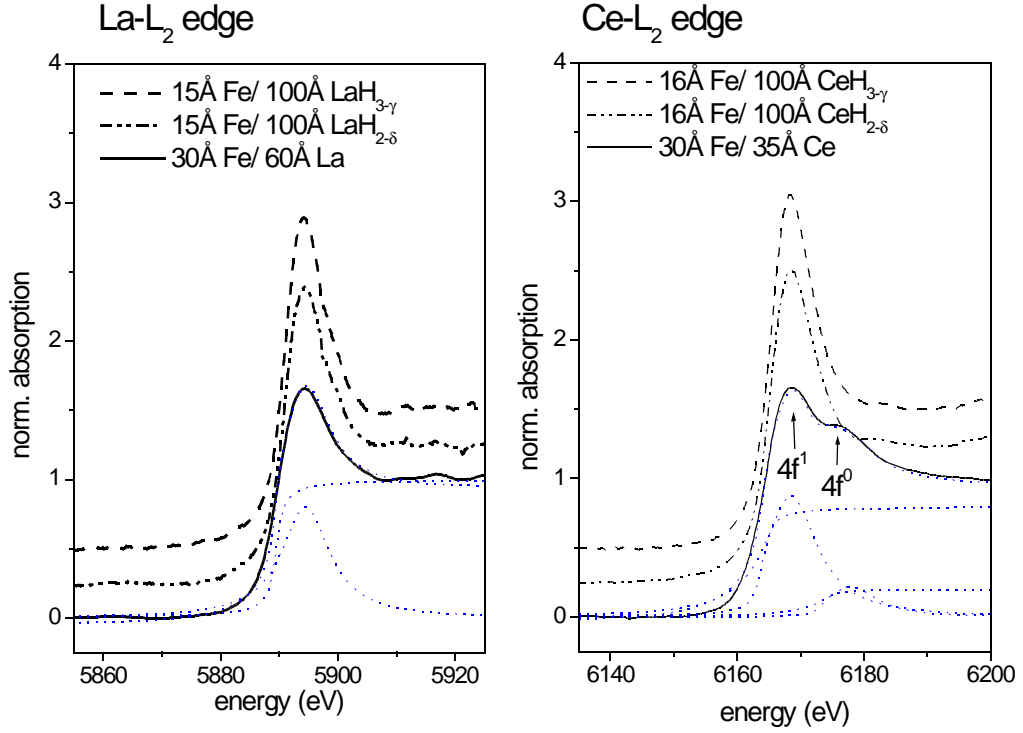
Figure 3.11. RE-L$_2$ edge absorption spectra for Fe/LaH$_X$ and Fe/CeH$_X$ multilayers. Curves are normalized to the jump at the absorption edge. Dottet lines: examples for the deconvolution of the spectra according to the model of Röhler [19] shown for the lower two spectra.

configuration in the hydrides (with only one peak in the absorption spectra). The first maximum has a white-line amplitude of 0.95, the white-line height for the 16Å Fe/ 100Å CeH$_{2-\delta}$ multilayer is ~1.5 (dihydride) and ~1.8 (trihydride).

The detailed analysis is very difficult if the thickness of the REH$_X$ sublayer is varied. A proof for a charge transfer was not possible. But using the Pauling electronegativity for a first glance, Fe has a value of 1.83 and the RE have values from 1.1 to 1.2, one expects a charge transfer at the interfaces from the RE to the Fe. Indeed the experiments show the trend that the white line is more intense for the thinner layers than for thicker REH$_X$ sublayers. But since there is a considerable angular dependence of the white-line intensity one has to be careful with a conclusion. More detailed measurements have to be done. In the following, only the magnetic interface polarization transfer will be discussed.

3.8 Magnetic interface polarization of the 5d states in the metallic and the insulating REH$_X$ sublayers

3.8.1 Multilayers Fe/LaH$_X$

The magnetic interface polarization of the La-5d states is probed by measuring the XMCD at the L$_{2,3}$-absorption edges of La at room temperature. The dichroic spectra are measured at ID 24 at the ESRF, as described in chapter 1.4. A typical data set for the L$_2$ edge is shown in figure 3.12 at the top. During the experiment the sample is exposed to a hydrogen atmosphere of a chosen constant pressure. After an hour of waiting time to warrant a well-defined situation, the spectra are measured. No further change in the dichroism signal could be determined, as expected from the measurement of the resistance. All signals are characterized by a strong negative peak on the low-energy side and a small positive contribution at the high energy side. Generally, a decrease of the dichroic signal with the increase of the charging pressure is observed. The decrease happens rather abrupt at a special charging pressure indicating the transition from the dihydride to the trihydride as it was observed in the conductance measurements before. It is astonishing that the magnetic polarization of the 5d electrons does not disappear in the insulating state.

The phenomenological model discussed in chapter 2.8 is used to extract the parameters α and β. The values of the height and width of the white line are generally taken as an average value obtained from the fits of the white lines due to the model of Röhler (chapter 2.7, 3.7). The height of the white line A$_L$ is set to 1.9, the width 2Γ is 8 eV. One Lorentzian is slightly reduced in width by the value of β, in order to fit the rather sharp drop to negative values at the low energy side of the XMCD signal (equation 2.10a,b).
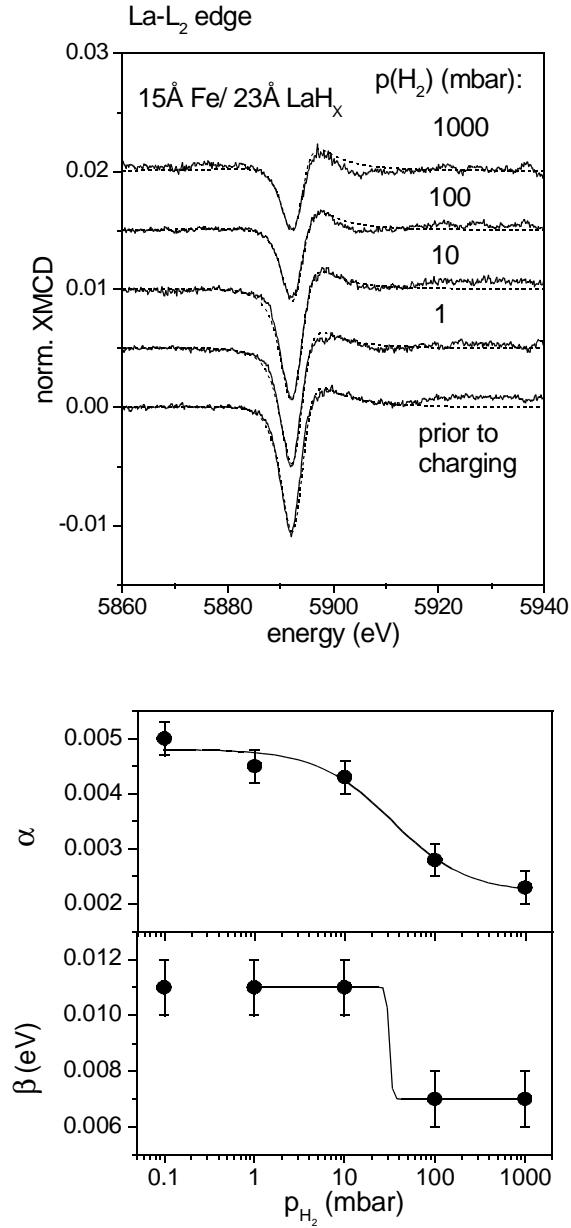
Figure 3.12. Decrease of the dichroism at the La-L$_2$ edge of a multilayer 15Å Fe/ 23Å LaH$_X$ for different charging pressures after 1h of charging with hydrogen. Dashed line: fit due to the α-β model. The metal-to-insulator transition is observed between 10 mbar and 1000 mbar. At the bottom the values extracted from the fit are plotted as a function of the applied hydrogen pressure.

The evolution of the parameters α and β with the charging pressure is presented in figure 3.12. The parameter α decreases rather smoothly through the metal-to-

insulator transition of LaH$_X$, whereas β shows an almost step-like decrease. This is reflected in the shape of the dichroism signal. The value of α determines the height of the negative peak. If α decreases faster than the parameter β, the influence of β on the shape of the XMCD signal becomes more important and the positive feature at higher energies rises. A sort of derivative-like character of the XMCD spectra becomes more pronounced.
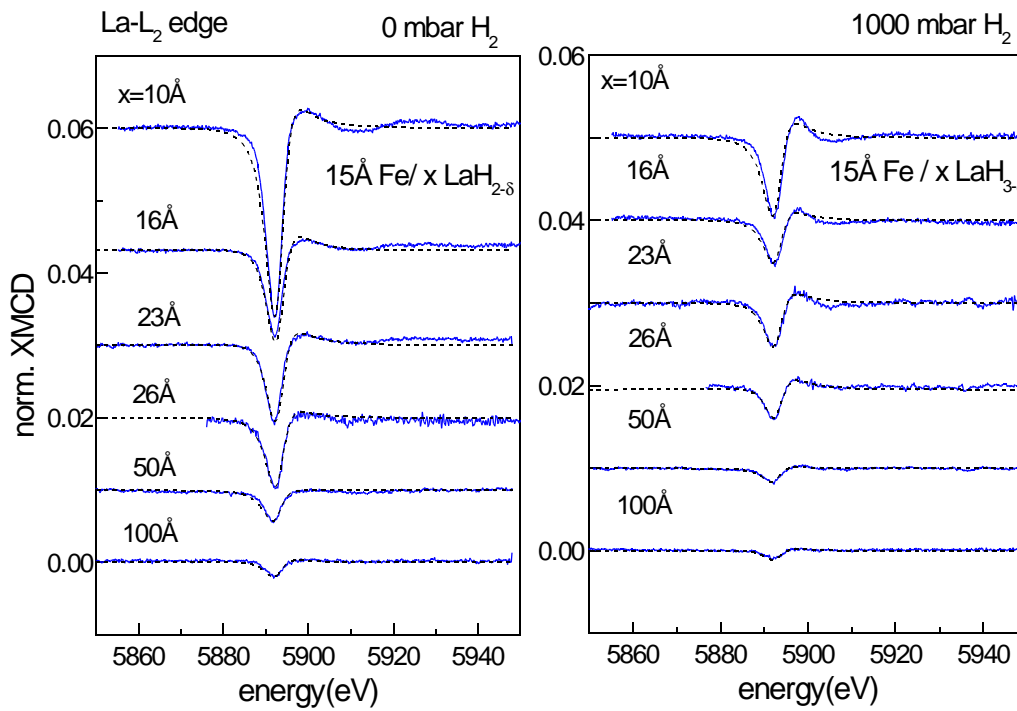

Figure 3.13. XMCD spectra at the La-L$_2$ edges in the Fe/LaH$_X$ multilayers. The Fe thickness is kept constant. On the left for the metallic dihydride prior to charging and on the right for the insulator.

In figure 3.13 the dichroic spectra at the La-L$_2$ edges are plotted for different LaH$_X$ thicknesses of metallic and insulating LaH$_X$. The XMCD measurements are an integrative method and therefore average over the whole layer. Thus the signal decreases with increasing thickness: as expected, the Fe polarizes only the interface by direct 3d-5d polarization. In addition, there is no significant change in shape. The dichroic signals of the thinnest and thickest layer, t_{LaHx}=10 Å and

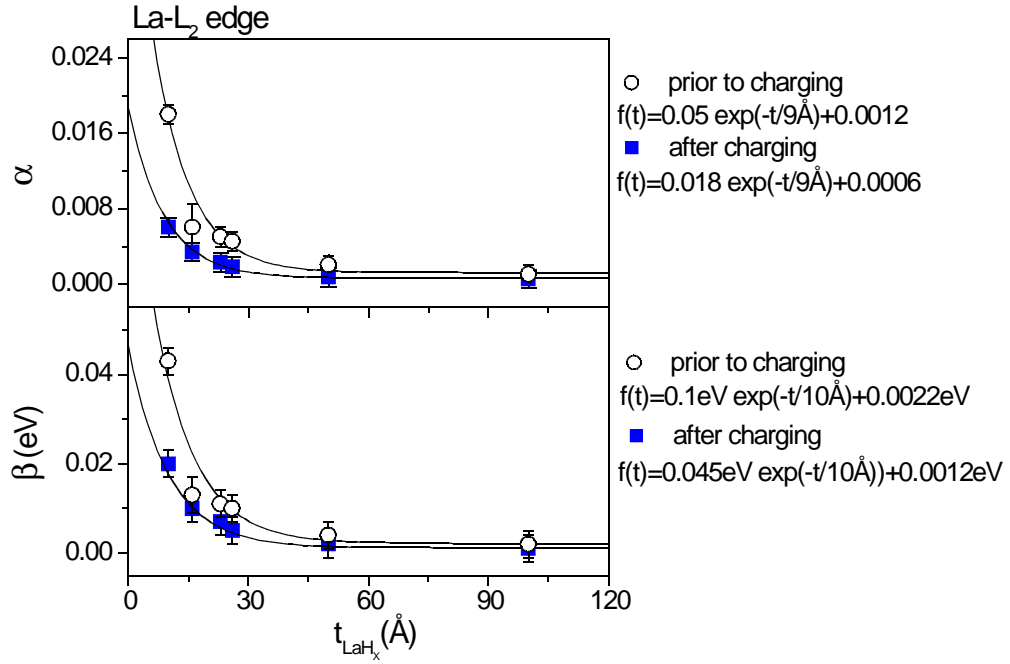*Figure 3.14. Results of the analysis of the XMCD spectra. α and β are plotted as a function of the LaH$_X$ sublayer thickness. For the metal the values are plotted with circles, for the insulator the values are plotted with squares. The lines are fits with an exponential decay model, the values are shown on the right.*

100 Å, have essentially the same profile, they are only reduced in size by a factor of ~10. If the multilayers are charged with hydrogen, the XMCD signal is reduced by a factor of two but does not vanish. The derivative-like character becomes more pronounced. As it can be seen in figure 3.13, the fit of the XMCD spectra with the presented model is quite good. A discrepancy is observed for the samples with thinner LaH$_X$ thicknesses above the absorption edge: a flat oscillation is superimposed to the measured signal. This can be seen best in the XMCD signal of the uncharged sample with the thinnest LaH$_{2-\delta}$ sublayer thickness. The effect can be attributed to nearest neighbor scattering at magnetic atoms [20].

The parameters α and β extracted from the analysis are plotted in figure 3.14. They decrease strongly as a function of the thickness. As the thickness is doubled,

the polarization decreases by a factor of approximately two. The similar decrease of both parameters reflects the fact already discussed above, that the line shape of the dichroic signal does not change as a function of the thickness. The parameters between the metallic and the insulating LaH_X sublayers differ by a factor of two for the α and less for the β. This slightly different behavior is responsible for the somewhat more dispersive character of the insulator spectrum. The measurements reveal something previously unexpected: the length scale on which parameters α and β decrease is the same for metal and insulator. This means, that the mechanism for the magnetic polarization of the La-5d states has to be similar for both phases. For a qualitative analysis of the penetration depth of the interface polarization, an exponential decay function is fitted to the data in figure 3.14. This is the natural ansatz for the extension of atomic wavefunctions (see metal/insulator interface, discussed in chapter 3.7). A polarization that is restricted to the interface would result in an reciprocal thickness dependence, which does not fit to the data points.

The formula used as well as the parameters are shown in the inset of figure 3.14. It consists of an exponential decay plus an additional constant which corresponds to a polarization throughout the whole LaH_X layer. The decay length of α or β resulting from the analysis is the same and amounts to approximately 9Å and is identical for metallic and insulating LaH_X. This means a decrease of the polarization by a factor of two from the initial value immediately at the interface on a length of 6 Å assuming a symmetric profile. To give an idea of the order of magnitude of the parameters: the polarization extrapolated to the direct interface is 0.05 for the metal and 0.018 for the insulating LaH_X; the residual values throughout the whole layer are $1.2 \cdot 10^{-3}$ for the metallic and $6 \cdot 10^{-4}$ in the insulating state. For β, at the direct interface, 100 meV for the metal and 45 meV for the insulator is estimated.
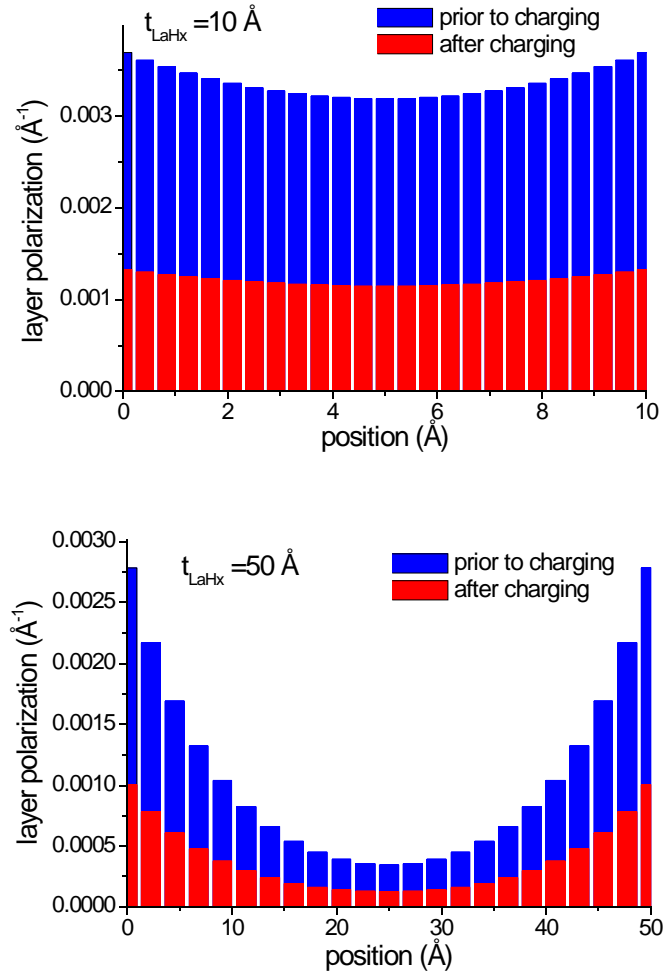
Figure 3.15. Profiles of the magnetic 5d polarization as a function of the position in the LaH$_X$ sublayer. The curves are calculated from the thickness dependence of the parameter α as described in the text. The thickness of the LaH$_X$ sublayer is 10 Å for the upper profile, and 50 Å for the lower profile.

Within this simple approach, it is possible to construct an image of the magnetic polarization profile of the 5d electrons in the LaH$_X$ sublayers, displayed in figure 3.15 for two LaH$_X$ thicknesses, 10Å and 50Å. In fact, since in La the 4f states are not occupied the parameter α is supposed to be a direct measure of the Fe-induced magnetic polarization of the 5d states ($\alpha=\Delta\rho=\rho_n^{\uparrow}-\rho_n^{\downarrow}$, see formula 2.9). The model profile deduced here is the simplest profile that results in an exponential thickness

dependence of the parameter α: the derivative of the exponential decay function approaching the middle of the LaH_X layer from both sides, located at x=0 and x=t. α' is the contribution to the polarization per Å, A is the value of the polarization at the interface, t_0 is the decrease length and t is the thickness of the layer.

$$\alpha'(x) = \frac{A}{2t_0}(e^{-\frac{x}{t_0}} + e^{-\frac{(x-t)}{t_0}})$$ 3.1

These profiles are just a simple image and must not reflect the real variation of the polarization in detail, but they show a considerable amount of polarization even in the middle of the LaH_X layer. In case of the 10 Å thick layer the polarization decreases only by 10%, in case of the 50 Å thick layer by 90%.

Two points are worth to be mentioned: the induced magnetic polarization on the La (in the order of 1-2%, figure 3.14) is by a factor 20 smaller than the Fe-layer polarization with about 30% and has the opposite sign [21]. Thus, the induced magnetic polarization is about a factor of 20 smaller with the opposite orientation, as it is expected by the model of Brooks discussed in chapter 2.2.

The origin of β has to be ascribed to the magnetic exchange interaction between Fe and La that shifts one spin species in energy, since 5d4f-exchange interactions of the final state [22] are absent in the case of La.

To obtain further information, the α-β model has been applied also to the XMCD spectra measured at the La-L_3 edge in the multilayers. Fits are shown for two 16Å Fe/ t Å LaH_X multilayers with the LaH_X thicknesses t=23Å and 50Å (figure 3.16). At the L_3 edge, the predominating maximum is positive and the dispersion changes from $\mp$ observed at the L_2 edge to $\pm$ at the L_3 edge. This is expected since the spin of the photoelectron changes the sign (chapter 2.8). In the case of the sample with the LaH_X thickness t=23Å, the parameter α for the La-L_3 edge is $1.2 \cdot 10^{-3}$ for the
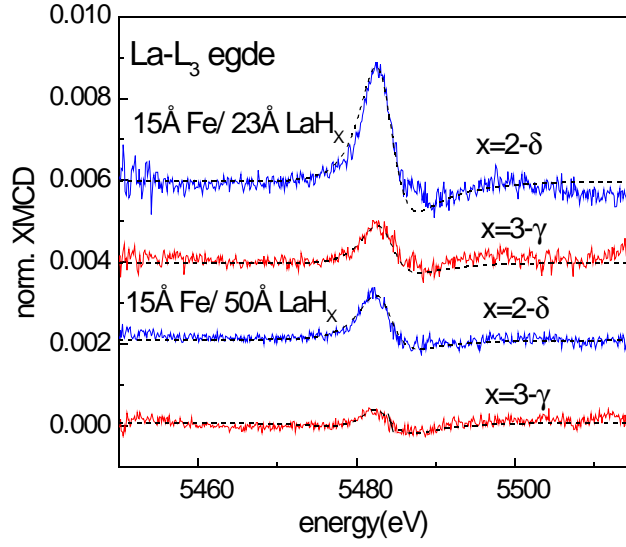
Figure 3.16. XMCD spectra at the La-L$_3$ edge for two Fe/ LaH$_X$ multilayers for the metallic and the insulating state. Dashed curve: fit with the α-β model.

metallic and $4\cdot10^{-4}$ for the insulating LaH$_X$ sublayer. This compares to the values $5\cdot10^{-3}$ and $2.3\cdot10^{-3}$ at the L$_2$ edge for the same sample. For the parameter β the values are 4 meV and 1.5 meV for the L$_3$ edge and 11 meV and 7 meV for the L$_2$ edge. If α and β are compared for both edges, a stronger decrease is observed for both parameters at the L$_3$ edge. In addition, at the L$_3$ edge a reduction of the parameter α by ~4 and of the parameter β by 2.5-3 is observed after the charging process. The reduction of α is distinctly larger than the value obtained at the L$_2$ edge. This different influence of the metal-to-insulator transition on the parameters α and β results in the more derivative-like line shape of the XMCD at the L$_3$ edge. A difference is expected since different final states are probed. As described in chapter 2, for the L$_2$ edge the 5d$_{3/2}$ and for the L$_3$ edge the 5d$_{5/2}$ valence states are probed in the absorption experiment. These states differ in their hybridization with the 3d states of Fe. Here it is important now to address the character of the electronic bonding.

In the crystal lattice bonds form and so orbitals are directed in a well defined way. As discussed in chapter 3.3, the triplett t_{2g} orbitals point towards the tetrahedral places. These states are essentially not affected by further hydrogen charging process from the dihydride to the trihydride, when the octahedral sites are increasingly occupied. The e_g orbitals point along the octahedral places and stabilize the H^--ion configuration. Consequently these states are more affected by the further charging. Furthermore the t_{2g} orbitals form the bonds with the Fe atoms, hence they are polarized directly. For a simple explanation of the different dichroic signals at the L_2 and the L_3 edge it has to be noted that t_{2g} orbitals have a stronger $j=3/2$ character [23] and thus for the L_2 edge a stronger polarization α will be measured. But since these orbitals point along the tetrahedral places, α will not vary strongly by the charging process. Because of their $j=5/2$ character, the e_g orbitals are affected stronger by the transition from the $LaH_{2-\delta}$ to $LaH_{3-\gamma}$, and thus the parameters α and β show a stronger variation due to the further hydrogen charging for the L_3 edge. The value of the parameter β, that is a kind of 3d-spin-5d-spin exchange in this simple qualitative discussion, will depend on the overlap of the 3d-Fe and 5d-La orbitals. For a detailed analysis the character of the interface hybridization has to be calculated and compared to the results presented.

Concerning the application of ferromagnet (FM)/ insulator/ ferromagnet (FM) structures as a magnetic tunnel junction, the studies on the magnetic interface polarization of Fe/LaH_X multilayers reveal interesting details. The functioning of a tunneling magnetoresistance element is shown in figure 3.17. The spin polarized tunneling current depends on the density of states at the Fermi energy and the magnetic orientation of both electrodes. In the antiparallel orientation the resistance increases. In the simple approach of Julliere's model [24] the polarization of the electrodes P_1 and P_2 determine the change in resistance:

$$\frac{\Delta R}{R} = \frac{R_{AP} - R_P}{R_{AP}} = \frac{2 P_1 P_2}{2 - P_1 P_2} \qquad\qquad 3.2$$

But the comparison with the experimental data reveals many examples where this simple approach yields a wrong value [25], especially if the direct spin-polarized electrode/insulator interface is modified [26]. In the case of Co/Al$_2$O$_3$/Py, an oxide at the direct interface of the Co that could be induced during the oxidation process of the barrier changes even the sign of the magnetoresistance [27]. In the experiments on Fe/LaH$_X$ multilayers, the metallic or insulating character of the barrier layer LaH$_X$ can be varied by hydrogen charging from the metallic LaH$_{2-\delta}$ to the insulating LaH$_{3-\gamma}$. The results reveal a considerable polarization of the La-5d hole states even two monolayers away from the Fe/LaH$_X$ interface, which has the opposite sign as the polarization of the 3d-Fe states. Furthermore the penetration
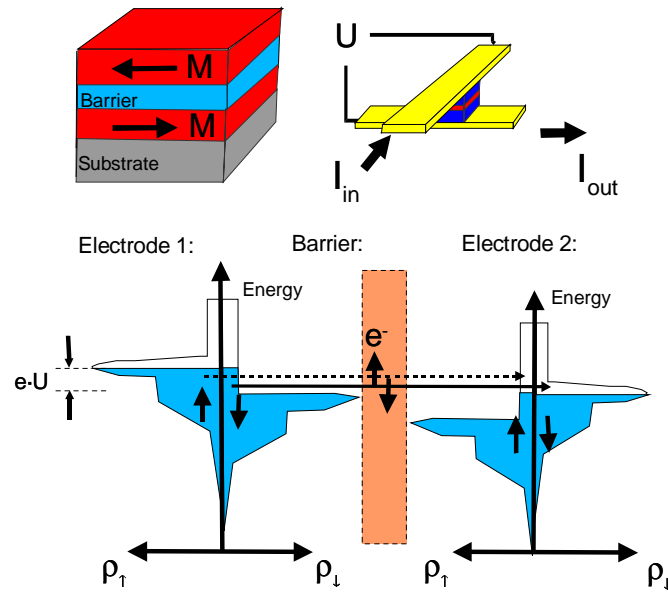

Figure 3.17. Schematic viewgraph for the magnetic tunneling resistance and illustration of Julliere's model. Upper part: layer structure with two magnetic electrodes in antiparallel orientation and the four point geometry for the resistance measurement. Lower part: spin dependent tunneling for antiparallel aligned electrodes.

depth of the magnetic polarization into the LaH_X layer is not modified by the metal-to-insulator transition. Note that this induced magnetic polarization interface states influences the tunneling current as well as the spin-polarized electron states of the FM electrode.

3.8.2 Multilayers Fe/CeH$_X$

Magnetic dichroism at the Ce-$L_{2,3}$ edges is more complex than in the case of the La-$L_{2,3}$ edges due to the presence of the 4f electron. In Fe/CeH$_X$ the electronic structure of the Ce is γ-phase like, i.e. the 4f states are localized (chapter 2.1). This can be seen at the L_2 edge of Ce which shows a single white line (figure 3.11). The interaction of the Ce-5d states with the localized Ce-4f electron leads to a strongly correlated system.

Figure 3.18. presents XMCD spectra measured at 300 K at the Ce-L_2 edge of several Fe/CeH$_X$ multilayers as a function of the thickness of the CeH$_X$ sublayer, for the metallic $CeH_{2-\delta}$ dihydride and for the insulating $CeH_{3-\gamma}$. In addition to the main negative signal at the edge there is the signature of an electronic transition 10 eV above the edge. Its origin cannot be a quadrupolar transition 2p $\rightarrow$ 4f since its signature must be expected below the edge because of a 4f-core hole interaction (chapter 2.6). Measurements for different orientations of the X-ray beam with respect to the sample normal reveal that this extra signal has neither dipolar nor quadrupolar angular dependency[1]. Hence its origin remains obscure, it must be connected with the 4f-electronic states since it is absent in the Fe/LaH$_X$ multilayers. For a separation from the first transition at the absorption edge, the second transition is fitted with a Lorentzian function. The XMCD signal at the

---

[1] *The measurements are performed by varying the orientation of the X-ray beam and the layer normal for different magnetic field values. Since magnetic easy axis of the sample is in plane at RT, for magnetic fields values smaller than the magnetic saturation field, the magnetization component in plane varies and thus the angle between magnetization and X-ray propagation direction as well.*
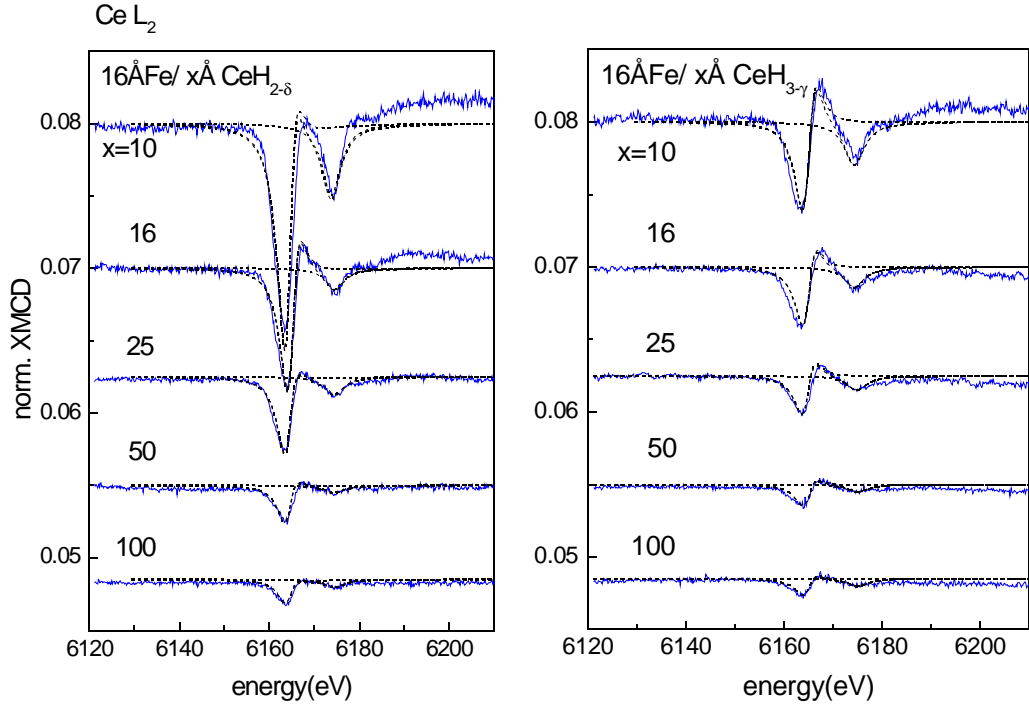
Figure 3.18. Dichroic spectra at the Ce-L$_2$ edges in the Fe/CeH$_X$ multilayers with metallic (right) and insulating (left) CeH$_X$ sublayers measured at room temperature. Solid lines are separate fits for the first and second transition.

edge is analyzed with the α-β model as in the case of the Fe/LaH$_X$ multilayers. An amplitude A_L of 1.6 and a width 2Γ of 10 eV for both spin orientations. This is a little bit broader than that of the white line for which 2Γ is about 9 eV. As it can be seen in figure 3.18 the measured dichroic spectra are well represented by the model, in the case of the as prepared samples with metallic CeH$_X$ and in the case of the samples in a 1000 mbar H$_2$ atmosphere where the CeH$_X$ sublayer becomes insulating. As in the case of the La hydride sublayers, there is a finite magnetic polarization in the insulating CeH$_X$. The XMCD signals decrease rapidly with increasing thickness of CeH$_X$: with doubling the thickness, the dichroism decreases by a factor of two. As for the case of the Fe/LaH$_X$ multilayers for a given CeH$_X$ thickness a reduction of the XMCD by a factor of two is observed
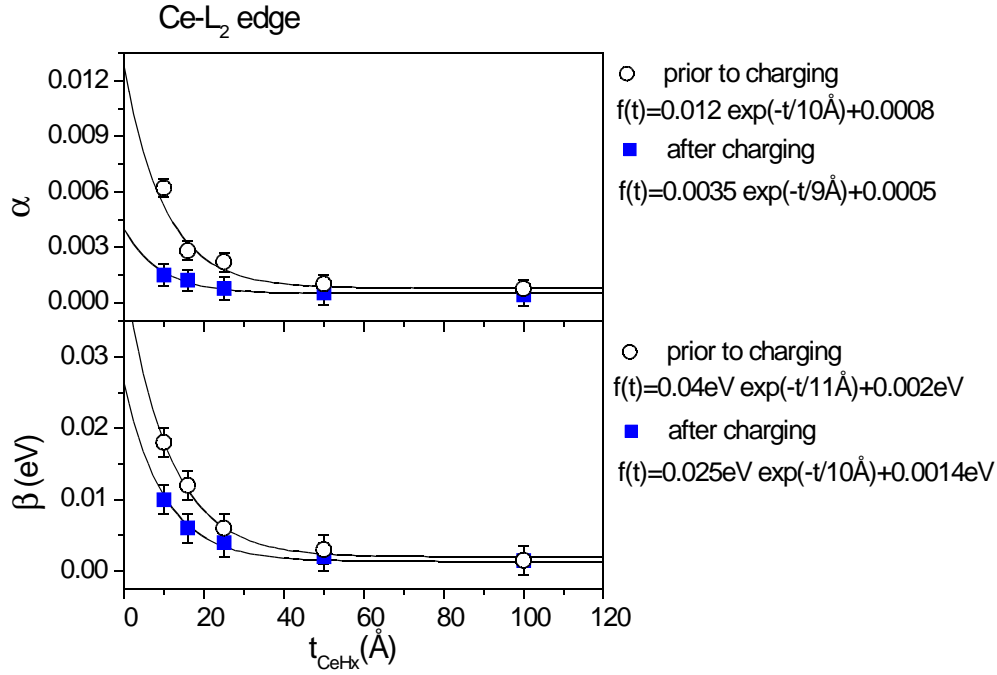
Figure 3.19. α and β resulting from the fits of the XMCD signals at the absorption edge as a function of the CeH$_X$ sublayer thickness. For the metal the values are plotted with circles, for the insulator the values are plotted with squares. The lines are fits with an exponential decay model, the values are shown on the right.

when the CeH$_X$ becomes insulating. This holds also for the second transition.

The parameter α and β resulting from the fits are presented in figure 3.19. They reflect the characteristic points of the evolution of the dichroic spectra. Both parameters decrease exponentially on a length scale of about 10 Å, quite similarly as in the Fe/LaH$_X$ multilayers. Upon the metal-to-insulator transition α decreases by more than a factor of three from $1.2 \cdot 10^{-2}$ to $3.45 \cdot 10^{-3}$, if the values extrapolated to the interface are taken. β decreases from 40 meV to 25 meV. The stronger reduction of α as compared to β pronounces the derivative-like characteristic of the XMCD.

In the same way as for the Fe/LaH$_X$ multilayers (chapter 3.8.1) a profile representing the variation of the parameter α across the metallic and insulating CeH$_X$
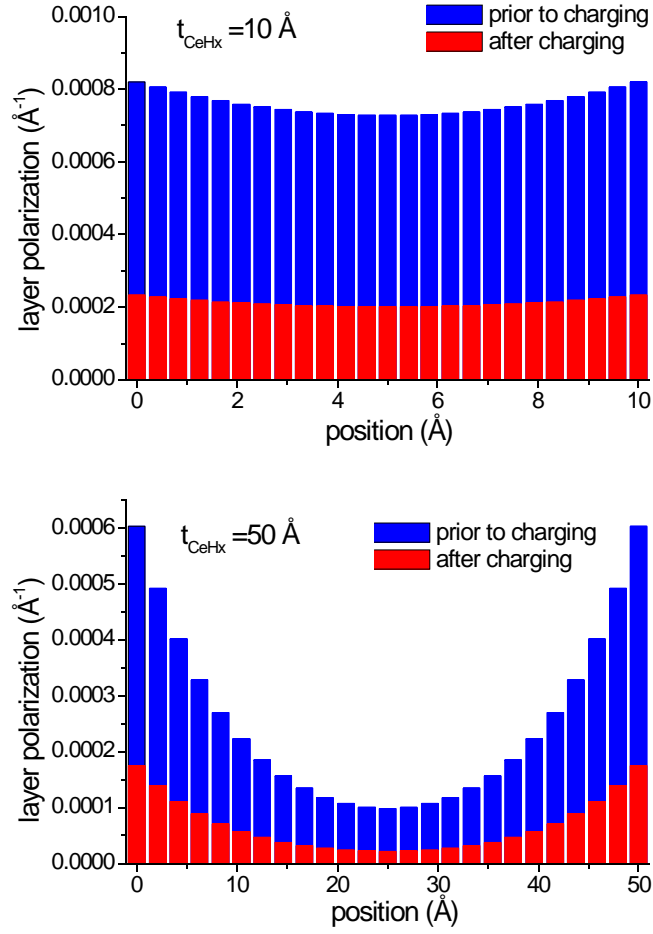
Figure 3.20. Variation of the layer polarization as a function of the position in the CeH$_X$ sublayer. The layer thickness is 10 Å for the upper profile, and 50 Å for the lower profile. In the case of the CeH$_X$ subayers the absolute value is not simply related to the magnetic polarization of the 5d states. The curves are calculated from the thickness dependence of the parameter α as described in the text.

sublayer (figure 3.20) is calculated. Note that here, in contrast to the Fe/LaH$_X$ multilayers, α is not simply related to the magnetic polarization of the 5d band but depends also on the spin dependence of the 2p→5d matrix element due to 4f-5d exchange interaction (see chapter 2.8.1). As it can be seen α decreases by 7% and 75% in the middle of the 10Å and 50Å thick CeH$_X$ sublayer.

The dichroic signal at the Ce-L$_3$ edge in the Fe/CeH$_X$ multilayers is shown in

figure 3.21. It has the opposite sign in comparison with the Ce-L_2-edge dichroic signal (figure 3.18) and also a double peak structure. In the metallic state of the CeH_X sublayers the peak at the absorption edge is slightly asymmetric indicating a non-zero β value. For the insulating CeH_X sublayer there is a slight negative contribution on the high-energy side of this peak. This indicates a stronger decrease of α than of β upon the transition to the isolating phase of CeH_X as it was observed for the Ce-L_2 edge as well.
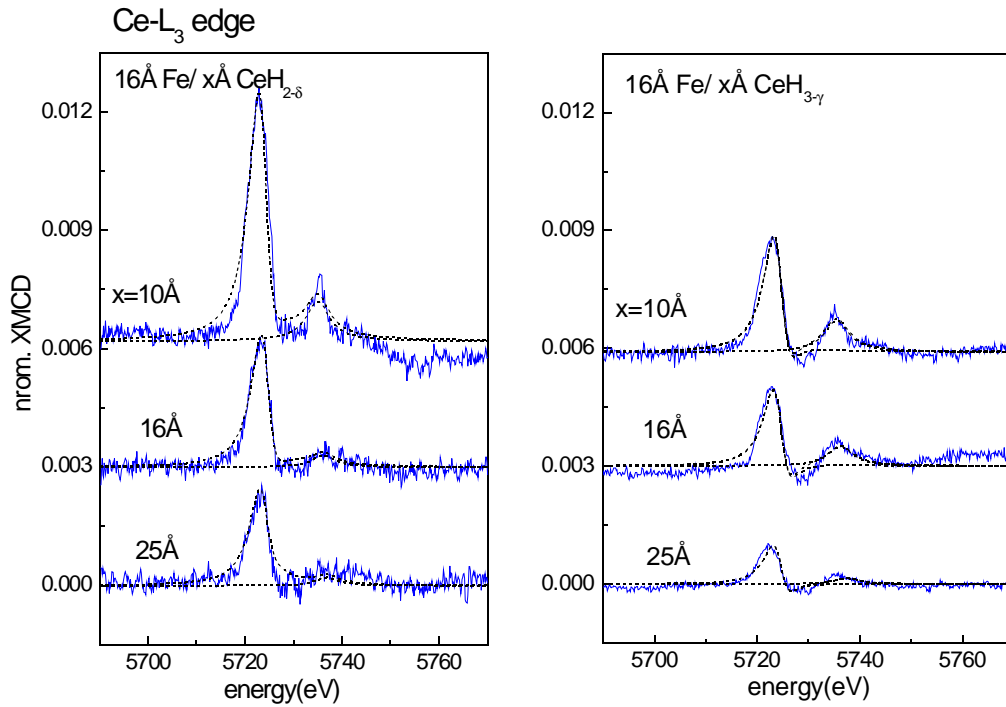

Figure 3.21. XMCD spectra at the Ce-L_3 edge in the Fe/CeH_X multilayers. Left: metallic dihydride prior to charging. Right: insulating trihydride, charged in an atmosphere of 1000 mbar H_2. Dashed lines are fits for the first and second transition.

The parameters α and β deduced from the fits of the Ce-L_3 XMCD spectra are shown in plot 3.22. They follow an exponential decay function with the same decay length of ~9Å in the metallic and in the insulating CeH_X (note that there are only three data points so it is a rather rough estimation). α drops by a factor of two
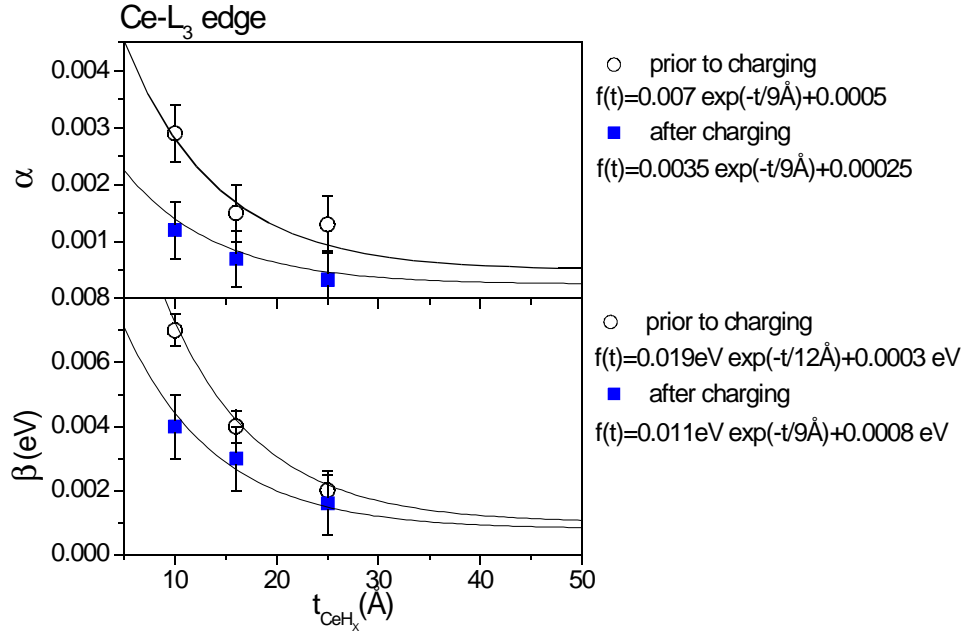
Figure 3.22. α and β as a function of the CeH$_X$-sublayer thickness. For the metal CeH$_{2-\delta}$ the values are plotted with circles, for the insulator CeH$_{3-\gamma}$ the values are plotted with rectangles. The lines are fits with an exponential decay model, the values are shown on the right.

by the charging process as compared to a factor of three at the Ce-L$_2$ edge. For this reason the derivative-like feature of the spectra is more pronounced at the Ce-L$_2$ edge. This is the opposite behavior observed for the LaH$_X$ sublayers.

The ratio of the XMCD intensities $I(L_2)/I(L_3)$ in the case of the Fe/CeH$_X$ multilayers at room temperature (RT) is around -2. This indicates that the 4f-5d interaction in Ce is weak at RT. This changes dramatically at low temperatures.

From the studies above not much information on the influence of the 4f-5d interaction on the dichroism at the L$_{2,3}$ edges is revealed. Therefore the temperature dependence of the XMCD signal at the Ce-L$_2$ edge is studied more in detail for a Fe/CeH$_X$ multilayer to shed light on the origin of the dramatic change in the L$_2$/L$_3$ branching ratio observed previously [28] and to investigate the influence of the metal-to-insulator transition on the spectral shape of the XMCD.
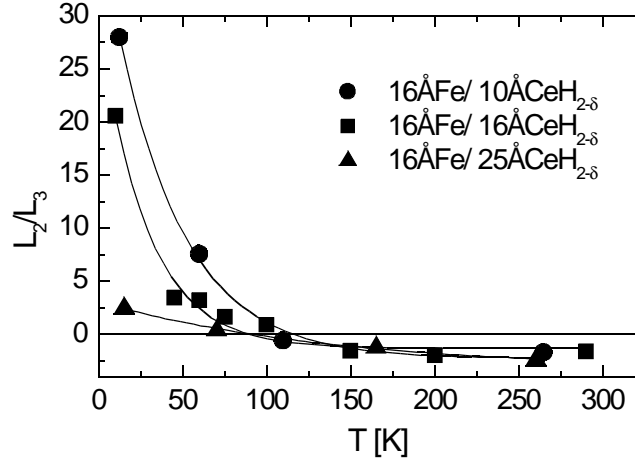
Figure 3.23. Branching-ratios L_2/L_3 in the Fe/CeH$_X$ multilayers with metallic CeH$_X$ measured as function of the temperature (from ref. [29]).

The graph of the change in the L_2/L_3 ratio as a function of temperature is replotted in figure 3.23. The branching ratios are -2 at room temperature indicating a weak 4f-5d interaction as pointed out above. With decreasing temperature the XMCD signal at the L_2 edge changes the sign whereas it stays positive at the L_3 edge. This results in a change of the sign of their ratio. As discussed in references [28,29] this variation points out an increased 4f-5d interaction at low temperatures due to an increased ordered 4f moment. It is related to the orientation transition of the macroscopic magnetization of the multilayers from in-plane at high to out-of-plane at low temperatures. But this will not be discussed further in the text. I will limit myself to the discussion of the analysis of the dichroic signals with the help of the α-β model.
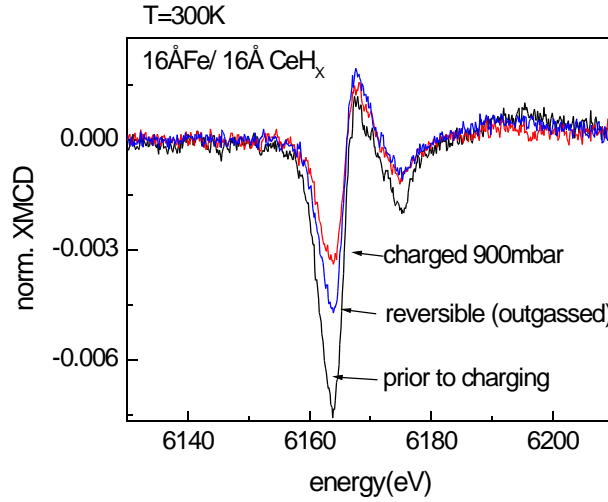
Figure 3.24. XMCD signal for a 16Å Fe/ 16Å CeH$_X$ multilayer with different hydrogen content in the CeH$_X$ sublayer. Three situations are shown: prior to charging, charged in a H$_2$ atmosphere of 900 mbar and after evacuation. If the hydrogen is pumped out of the charging chamber, the dichroism rises again.

For the cooling experiments a closed cycle cryostat is used. The sample is charged with hydrogen inside the cryostat. Before cooling to low temperatures the hydrogen has to be pumped off. This leads to some loss of hydrogen in the CeH$_X$ sublayer. Therefore the contribution of the reversible part within an outgassing period has to be checked. To warrant a well-defined situation, the XMCD was measured at RT until the signal does not increase anymore. Then, a stable condition with an outgassing time of ~29 days is reached as described chapter 3.5. The data are taken from low to room temperature. No further outgassing is observed in the time scale of the experiment if the size of the signal is checked again at the end of the measurement. The different XMCD signals measured at RT of the sample in the as-prepared state, charged with a pressure of 900 mbar H$_2$ and after evacuation of the cryostat are compared in figure 3.24. The measurements reveal a reduction of the XMCD by a factor of 0.4 for the charged and 0.6 for the outgassed state. These values correspond to the reversible change of the resistance
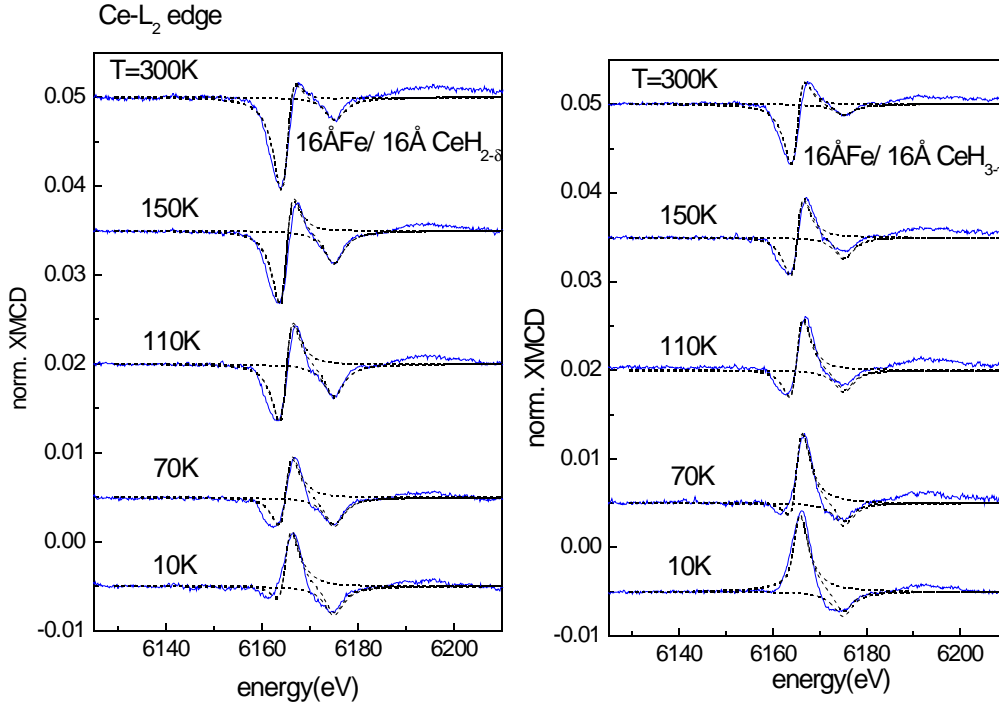
90

Ce-L$_2$ edge

Figure 3.25. Dichroic spectra at the Ce-L$_2$ edge for the 16Å Fe/ 16Å CeH$_X$ multi-layer. Metallic dihydride CeH$_{2-\delta}$ prior to charging (left) and the insulator CeH$_{3-\gamma}$ (right) as a function of the temperature. Dashed lines are fits for the first and second transition.

observed on a short time scale as it is extracted from the fit of the decrease of the resistance with a sum of exponential decays as described in chapter 3.5.

The evolution of the dichroic spectrum at the Ce-L$_2$ edge as a function of temperature is shown in figure 3.25, for the as prepared CeH$_{2-\delta}$ at the left and for the sample with additional hydrogen, CeH$_{3-\gamma}$, on the right. The signals change drastically with decreasing temperature. While the feature 10 eV above the absorption edge remains constant, the XMCD signal at the edge changes sign from predominately negative at RT to predominatly positive for T=10 K. At 110 K it is entirely derivative like. The comparison with the spectra for the metallic and the additionally hydrogenated CeH$_X$ reveals the unexpected result that for the insulating CeH$_X$ sublayer a larger XMCD is observed at 10 K than for the metallic
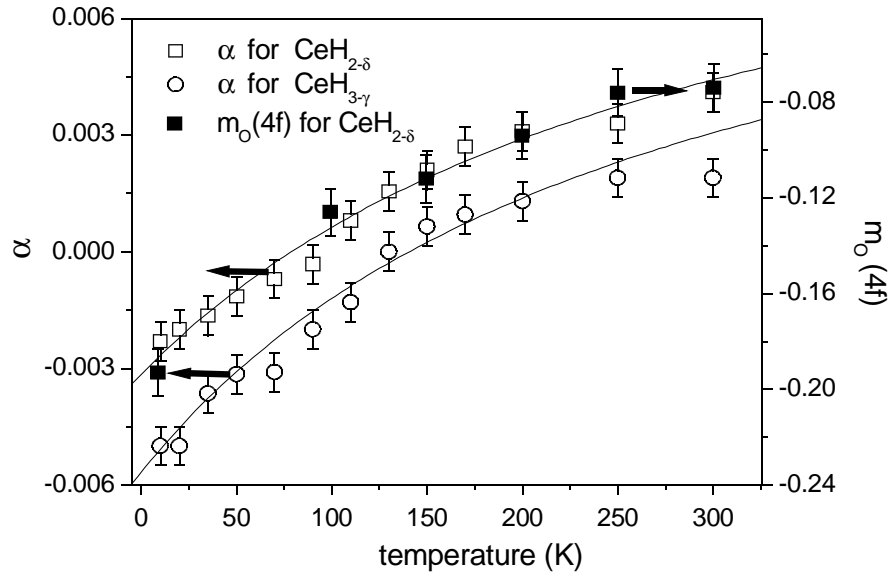
Figure 3.26. Temperature dependence of α for the 16Å Fe/ 16Å CeH$_x$ sample. The value of the Ce-4f orbital moment $m_O(4f)$ is plotted for a comparison with the value of α. The lines are guides to the eyes using a hyperbola function.

state. The analysis with the α-β model is shown in the dashed lines. The parameters for the Ce-L$_2$ absorption edge are A$_L$=1.5 and 2Γ=10 eV. It is obvious that at lower temperatures the small negative contribution to the XMCD spectrum at the edge can be fitted in size but does not correctly match the shape. This must be a result of different widths of the spin-up and spin-down density of hole states not taken into account here. The effect is symmetric at both sides of the dominating positive contribution to the XMCD signal, in contrary to the influence of the value of β that results in an antisymmetric shape of the XMCD.

The temperature dependence of the parameters α and β extracted from the fits of the XMCD signals is displayed in figures 3.26 and 3.27. The parameters vary in a different way. α decreases monotonically towards low temperatures and changes sign from positive to negative. This is expected since the 4f-5d interaction

becomes more important due to the breathing effect discussed in chapter 2.8.1. The contraction of the majority-spin-radial 5d function, for which the spin is oriented parallel to the 4f spin enhances the transition probability into this state and thus gives a negative contribution ΔM to the α value. This competes with the contribution of the spin polarization of the 5d states, i.e. the difference in unoccupied spin-up and spin-down Ce-5d states $\Delta\rho_n$ (chapter 2.8.1, equation 2.9) and leads to a point of compensation where α vanishes. It is interesting to compare the temperature dependence of α with that of the Ce-4f orbital magnetic moment $m_O(4f)$ of the 16Å Fe/ 16Å $CeH_{2-\delta}$ multilayer (figure 3.25a). This quantity has been previously derived [30] from XMCD measurements at the Ce-$M_{4,5}$ edges and represents the major part (190%) of the localized Ce-4f magnetic moment. The data show a very nice correspondence which is a clear evidence that α mirrors the 4f-5d interaction via the influence on the transition probabilities. Note that the Fe sublayer magnetization varies only by about 10% in this temperature range. Apparently ΔM and $\Delta\rho$ are in the same order of magnitude. At the point of compensation, α equals zero and β generates the purely derivative-like XMCD spectrum at the edge, in the case of the dihydride $CeH_{2-\delta}$ at a temperature of 110 K and in the case of the trihydride $CeH_{3-\gamma}$ at a temperature of 150 K (figure 3.25).

The effect of the metal-to-insulator transition can be described very simply in this model. The charging process pulls the complete curve of α to negative values by a constant, temperature independent shift of approximately $1.5 \cdot 10^{-3}$. Thus the crossing of the temperature axis occurs at different temperatures. This is an explanation for the stronger positive XMCD observed for the insulating $CeH_{3-\gamma}$ in comparison with the XMCD measured in the $CeH_{2-\delta}$ state at low temperatures.

Not as clear is the origin of the temperature variation of the parameter β (figure 3.27) that is deduced from the measurements. β stays constant down to far below RT and shows a step-like decrease at 85K and 45K for the metallic and insulating
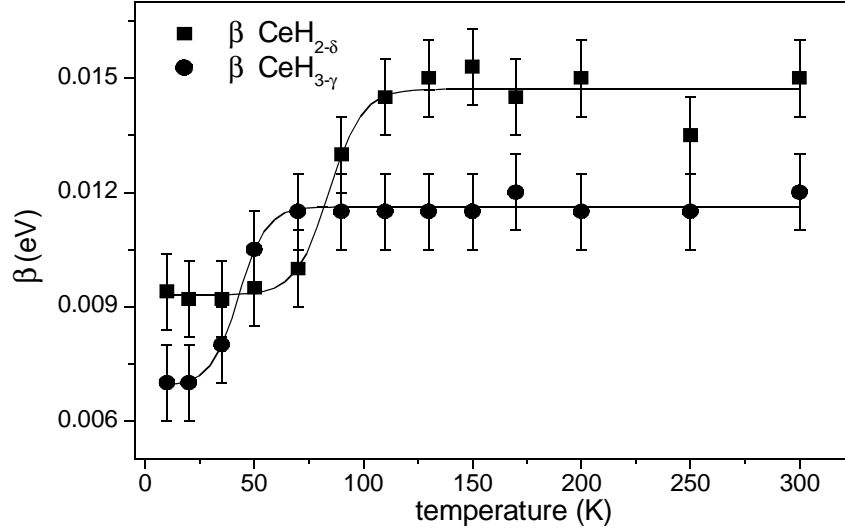
Figure 3.27. Temperature dependence of the parameter β for the 16Å Fe/16Å CeH$_x$ sample. The lines are a guide to the eyes using a sinosodial stepfunction.

CeH$_X$, respectively. However, with increasing 4f-5d interaction at low temperatures one would expect an increase of β. H$_2$ charging reduces β in the temperature independent regimes by 3 meV.

Thus, additional hydrogenation of the as prepared Fe/CeH$_{2-δ}$ multilayers modifies the value of the 4f-5d interaction. In figure 3.28 the XMCD signals at the Ce-M$_{4,5}$ edges measured at 10 K are plotted for two multilayers with different CeH$_X$-layer thicknesses in the as-prepared state and in the hydrogen charged CeH$_{3-γ}$ phase. The spectra are measured at beamline SU 22 (Super ACO, Orsay). The total RE thickness of the multilayer stack is 150 Å as described in chapter 1.4. These spectra probe directly the Ce-4f moment.

The values at room temperature are below the instrumental resolution of the beamline. For the 16 Å thick CeH$_X$ sublayer no change of the signal could be detected upon charging. This may be attributed to the loss of the additional hydrogen in this particular sample in the vacuum of the experimental chamber. But for
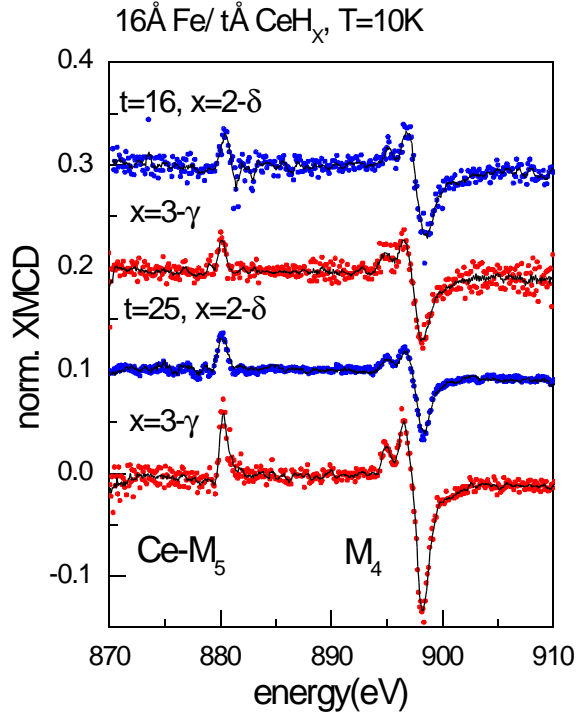
Figure 3.28. XMCD spectra at the Ce-M$_{4,5}$ edges of a 16 Å Fe/ tÅ CeH$_X$ multilayer plotted for two different CeH$_x$ thicknesses, 16Å and 25Å, prior to and after hydrogen charging, measured at 10K.

the sample with 25Å thick CeH$_X$ after adding hydrogen one observes a huge increase of the XMCD at the M$_4$ and M$_5$ edge by a factor of two for the sample charged with additional hydrogen. This is related to the increase of the XMCD signal at the Ce-L$_2$ edge at 10 K (figure 3.25). A higher 4f magnetic moment results in a change ΔM and in a shift of α towards negative values.

Thus the temperature dependence of the parameter α extracted from this rather simple model can be explained by the 'breathing' effect. The 4f-5d exchange interaction is responsible for the astonishing L$_2$/L$_3$ ratios (figure 3.24) and the failure of the sum rule in the case of the Ce-L$_{2,3}$ XMCD spectra of the Fe/CeH$_X$ multilayers.

3.8.3 Multilayers Fe/GdH$_X$: interface polarization and antiferro-magnetic ordering

Gadolinium metal is a ferromagnet with a Curie temperature somewhat above room temperature. Its 4f shell is half filled and in agreement with Hund's rules, presents a pure spin moment. Hydrogenation leads to a drastic change of magnetic order. Bulk GdH$_2$ is an antiferromagnet with a Neél temperature near 20 K [30]. The aim of the present study is to investigate the magnetic polarization of the Gd 5d states in multilayers Fe/GdH$_X$ near the interfaces, across the paramagnetic-antiferromagnetic phase transition and its modification when GdH$_X$ becomes an insulator.

The data shown in figure 3.29 are the XMCD spectra at the Gd-L$_2$ edge for metallic and insulating GdH$_X$ in the multilayers. As in the cases before, the Fe thickness is kept fixed at 16Å and the GdH$_X$ thickness is varied. The data are measured at RT where GdH$_X$ is paramagnetic. The XMCD signal is up to 7% of the absorption egde which is considerably higher than in the case of LaH$_X$ or CeH$_X$ discussed in the preceding chapters.

For insulating GdH$_{3-\gamma}$ we observe a general decrease of the XMCD by a factor of two. There is essentially no modification of the line shape. The structure at energies above the absorption edge may be a result of multielectron excitations, similar to compounds of RE and TM [31]. These multielectron excitations will be disregarded in this work.

For the analysis with the α-β model the following parameters are used: the white-line amplitude is A$_L$=1.7 and the width of the Lorentzian is 2Γ=8 eV. The parameters α and β are plotted in figure 3.30. The α values are all negative and
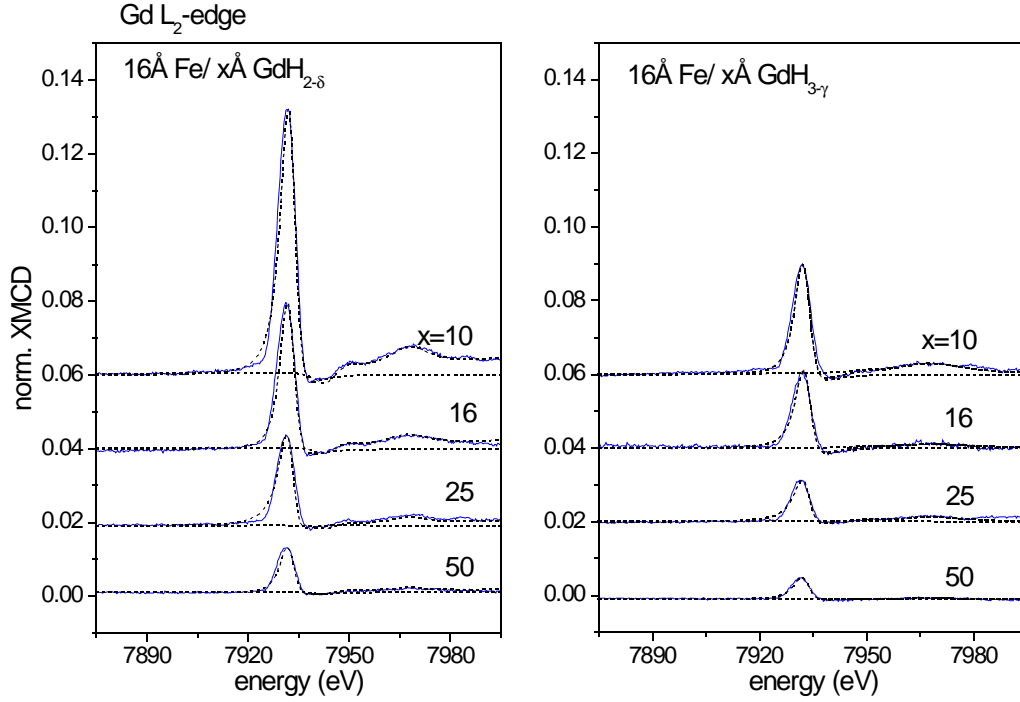
Figure 3.29. XMCD spectra at the Gd-L_2 edge in the Fe/GdH$_X$ multilayers at RT. Left: metallic dihydride prior to charging. Right: the insulating hydride charged in 1000 mbar H$_2$ atmosphere. Dashed lines: analysis with the α-β model and separation of the multiple scattering part at higher energies.

decrease on a length scale of 9 Å similar to the other Fe/REH$_X$ multilayer systems. The values extrapolated to the interface are -0.10 for the metallic and -0.04 for the insulating GdH$_X$. The parameter β is negative as well and the values at the interface are -170 meV and -55 meV. β decreases more slowly from the interface than the value of α. The decay length is 12 Å for the metallic and even 15 Å for the insulating GdH$_X$ sublayer. The dichroism at the L_3 edges not shown here is about a factor of two smaller and has the opposite sign. It is superposed with small oscillations resulting from the Fe-K edge and therefore the α-β model is not applicable. Derivative-like features could not be detected for metallic or insulation GdH$_X$, neither at the Gd-L_2 nor the Gd-L_3 edge.

It is an interesting observation that the signs of the dichroic signals at the $L_{2,3}$ edges
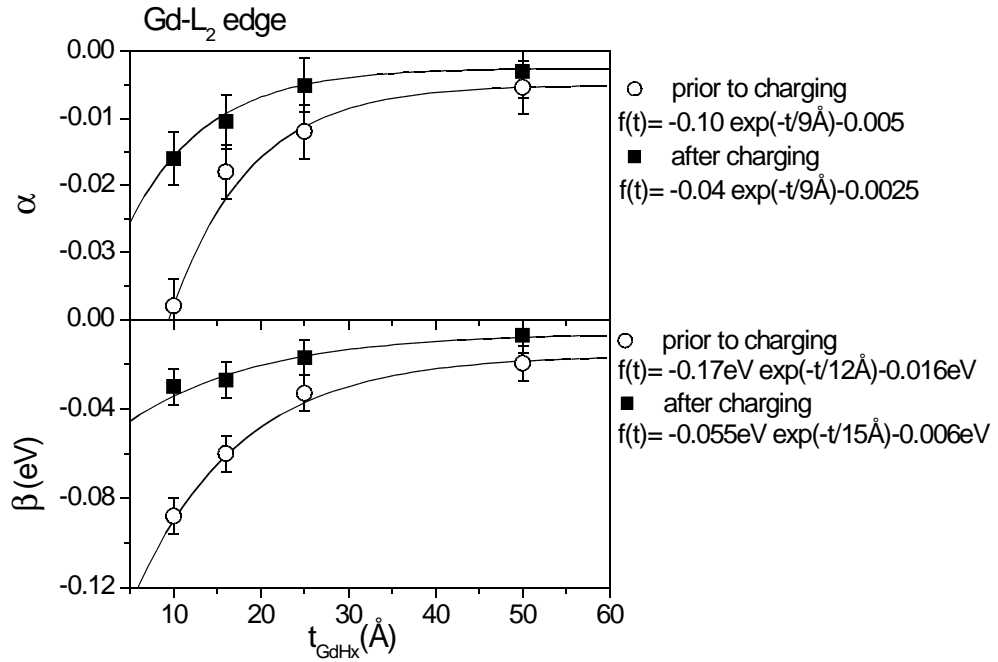
Figure 3.30. Parameters α and β as a function of the GdH$_X$ sublayer thickness in Fe/GdH$_X$ multilayers. For the metal GdH$_{2-\delta}$ the values are plotted with circles, for the insulator GdH$_{3-\gamma}$ the values are plotted with squares. The lines are fits with an exponential decay function shown on the right.

observed in the Fe/GdH$_X$ multilayers (positive at the L$_2$ edge and negative at the L$_3$ edge) are the opposite of the signs expected by comparison with the XMCD spectra measured for the Fe/LaH$_x$ and Fe/CeH$_X$ multilayers at room temperature (see chapter 3.8.1 and 3.8.2). To briefly recall the problem of relating the sign of the XMCD signal to the orientation of the ordered magnetic moment probed: based on the convention given in chapter 2.3 one concludes that a positive (negative) XMCD signal at the L$_2$ edge is associated with a parallel (antiparallel) magnetic polarization with respect to the applied magnetic field. Therefore it must be concluded that the Gd-5d ordered magnetic moment is aligned along the magnetic field direction due to the positive sign of the XMCD at the L$_2$ edge.

This is contradictory to the model of Brooks (chapter 2.1). The magnetic order in the paramagnetic GdH$_X$ is induced by 3d-5d hybridization leading to an anti-parallel orientation of the 3d and 5d interfacial magnetic moments. Since the Fe

magnetization is aligned in the magnetic field direction, a negative XMCD signal at the L_2 edge of Gd is expected. In fact the reversed sign in the case of Gd is an indication of a strong 4f-5d spin interaction that enhances the $M^{\downarrow}$ matrix element for the 2p→5d dipole transition and leads to a negative $\Delta M = M^{\uparrow} - M^{\downarrow}$ and consequently to positive XMCD at the Gd-L_2 edge. As pointed out in chapter 2.8 the enhancement of the dichroic signal by ΔM can be up to 30% [32]. This breathing effect competes with the spin polarization of the 5d states which leads to a positive parameter α that is only in the order of one percent as indicated by the results for the Fe/LaH$_X$ system. For the Fe/GdH$_X$ multilayer system the 4f-5d exchange interaction results in a negative parameter of α even at RT, whereas for the Fe/CeH$_X$ multilayer system a negative value of α is observed only for low temperatures at the L_2 edge (chapter 3.8.2). Is is a result of the strong spin moment of the 4f state.

In the literature Gd and its compounds are textbook examples for the 'breathing effect'. Early calculations of Harmon et al. [33] predict the contraction of the 5d states. Schütz et al. [34] found a negative (positive) XMCD signal at the Gd-L_2(L_3) edge. Goedkoop at al. [22] measured the $L_{2,3}$-XMCD spectra of Gd in insulating Gd$_3$Ga$_5$O$_{12}$ and calculated the influence of the 'breathing effect'. In their case the localized Gd-4f moment is pulled in field direction. Quite interesting is the comparison with the amorphous alloy system Gd(Ni$_X$Co$_{1-X}$) [35]. In this TM-RE alloy the RE-4f and TM-3d-electron magnetizations are aligned antiparallel. Their different temperature dependence leads to a compensation temperature for the overall magnetization of the alloy. It separates the low-temperature regime where the Gd-sublattice magnetization dominates from the high temperature regime where the TM sublattice magnetization dominates. Below the compensation temperature the overall magnetization direction is determined by the RE-4f moment. A negative (positive) sign of the XMCD is observed at the L_2(L_3) edge.

Above the compensation temperature, the magnetization direction is determined by the TM-magnetic moment and the sign of the dichroism is reversed at both edges. This effect reveals again that the breathing effect, i.e. the spin dependence of the matrix element for the 2p→5d transition due to the 4f-5d exchange interaction determines the size and sign of the dichroism at the L$_{2,3}$ edges of Gd and not the magnetic polarization of the 5d-electron states.

The signs of the L$_{2,3}$ spectra of Gd in this alloy system (and also in Gd metal and various Gd intermetallics and compounds) agree with our observation in the Fe/GdH$_X$ multilayers. This is remarkable since the magnetic order on Gd is generated a different mechanism. To conclude, the XMCD experiments at the Gd-L$_{2,3}$ edges in various systems, including our multilayers, support the breathing model quite convincingly.

For the sample 16Å Fe/ 25Å GdH$_X$ the temperature dependence is studied at the DCI (energy dispersive beamline D 11). It is known from literature [36,37] that the GdH$_X$ bulk values of the antiferromagnetic(AF)-ordering temperature are at about 21 K for the dihydride and somewhat lower for the trihydride. The full magnetic moment on the 4f shell of 7μ_B is measured: 7.7μ_B for the dihydride and 7.3μ_B for the trihydride [37]. With the powerful element selectivity of the XMCD it is possible to examine the ordering temperature of the RE-hydride sublayer in the Fe/GdH$_X$ multilayer separately. It is of special interest in how far the interaction with the Fe-layer reduces the antiferromagnetic order of GdH$_X$ and secondly, does the modification of the electronic structure by additional hydrogen charging influence the magnetic properties? A typical scan of the bulk magnetization at constant field with a vibrating sample magnetometer just reveals the influence of the AF ordering on the magnetization of the Fe layer by a reduction of the signal depending on the field value.
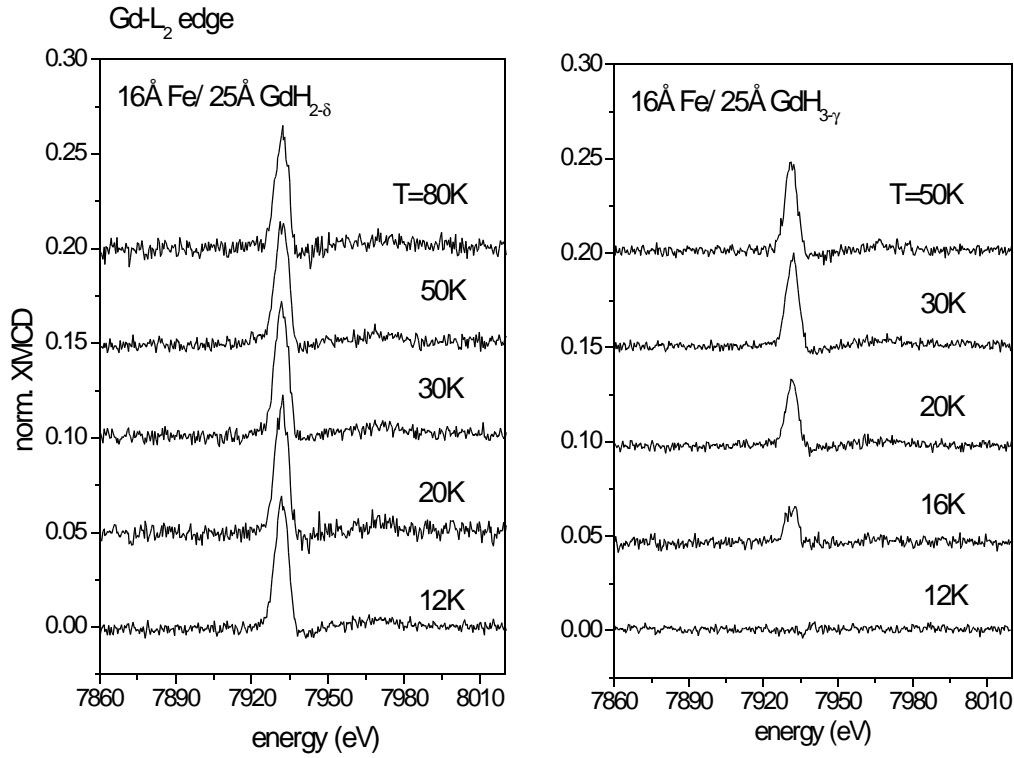
Figure 3.31. Dichroic spectra at the Gd-L$_2$ edge for the 16Å Fe/ 25Å GdH$_X$ multilayer sample. Left: metallic dihydride GdH$_{2-\delta}$ prior to charging. Right: insulating phase GdH$_{3-\gamma}$. The spectra are measured near the expected AF-ordering temperature T$_N$=20 K of the GdH$_X$ sublayer.

The XMCD spectra for as-prepared sample and after additional hydrogen charging are plotted in figure 3.31 in the temperature range near the expected transition temperature of about 20 K. Measurements of the resistance reveal that the GdH$_X$ sublayers in the sample are in the insulating state after charging in an hydrogen atmosphere of 1000 mbar H$_2$ and evacuation of the cryostat afterwards. In GdH$_X$ the metal-to-insulator transition occurs at x=2.3 [37]. The signal of the as-prepared samples in the metallic GdH$_{2-\delta}$ phase show a small increase with lowering the temperature and passes a not very pronounced maximum at 20 K which indicates AF ordering in GdH$_X$ sublayer. The shape does not change significantly. The size of the dichroism is about 0.07. For the charged case a different behavior is ob-
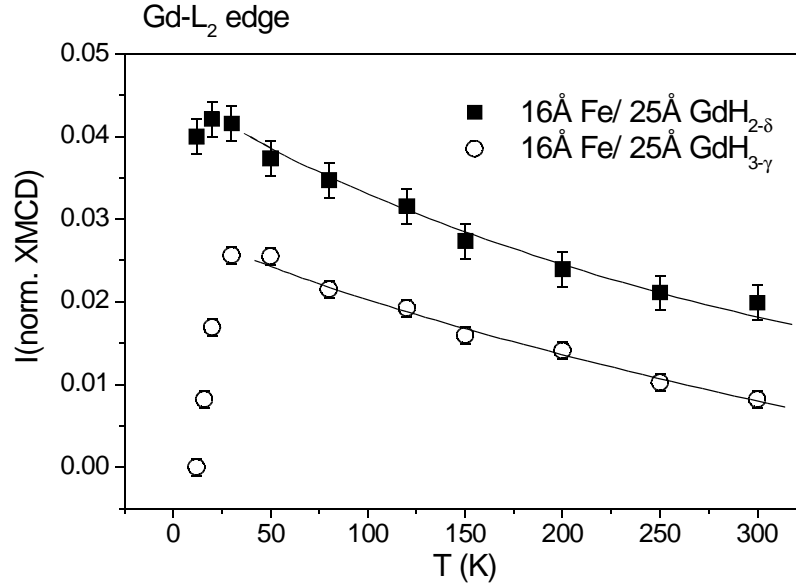
Figure 3.32. Dichroic signal at the Gd-L$_2$ edge measured for the metallic dihydride GdH$_{2-\delta}$ (squares) and the insulating trihydride GdH$_{3-\gamma}$ (circles) as a function of temperature.

served: the AF ordering results in a strong drop of the signal below ~25 K. At the lowest temperature of 12K the dichroic signal even vanishes.

This behavior is visible more clearly in figure 3.32 which shows the amplitude of the XMCD as a function of the temperature. At RT the amplitudes differ from each other by a factor of two. From RT to 150 K they follow a Curie-Weiss-like behavior. The AF ordering results in an antiparallel alignment of neighboring 4f spins and the average magnetic polarization vanishes. In both cases, the metallic GdH$_{2-\delta}$ and the insulating GdH$_{3-\gamma}$, the AF order can be observed even for the 25Å GdH$_X$ thin film. The Néel temperature of the GdH$_X$ sublayer is in the order of the value reported for bulk GdH$_X$. Secondly, the value is higher in the insulating than in the metallic phase of the GdH$_X$ sublayer.

The AF ordering in the GdH$_X$ sublayers permits to observe the effect of the exchange biasing which is of great current interest. The details of the exchange

biasing are not well understood but the principle is easy. If the magnetic ordering of the AF layer in contact with a ferromagnetic (FM) layer takes place in a magnetic field sufficient to saturate the Fe, the AF layer in direct contact to the magnetic moments at the interface next to the FM layer will order with spins parallel to the FM layer. Due to the AF order the next atomic layer in the AF layer is supposed to orientate antiparallel. Since the AF coupling is not destroyed in a high field this yields to a memory effect that forces the FM moments at the interface in the direction imprinted by the outer field during the ordering of the AF layer. It acts as an effective field, the so called exchange bias field.
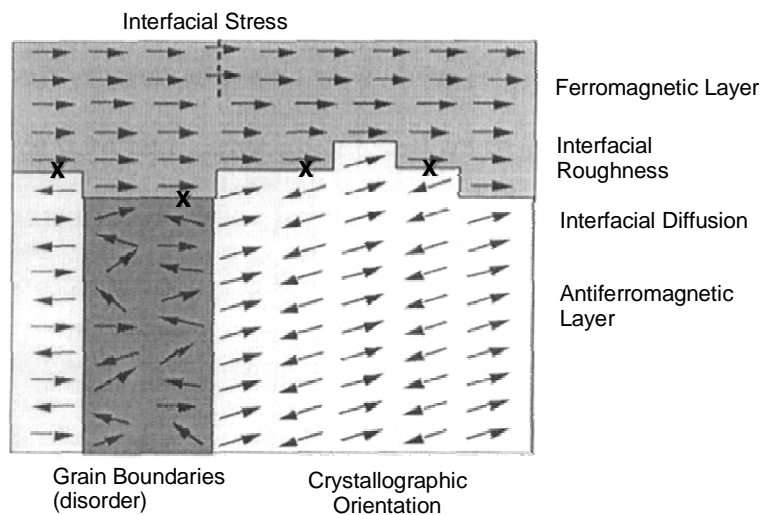

Figure 3.33. Schematic diagram of the influence of interface roughness, grain boundaries and crystallographic orientation at an AF-FM interface. In this figure, the interfacial spins prefer to align parallel. The frustrated interfacial spins are marked with an x [38].

Figure 3.33 illustrates the related problems. An interface is never atomically flat which results for example in frustration of the spins that want to order antiferromagnetically. Another problem is the orientation of the crystallites at the interface: due to the crystalline anisotropy the AF magnet prefers to align the moments parallel to a crystallographic direction. The influence of the strength of the AF coupling on the exchange-bias field can be studied gradually in the

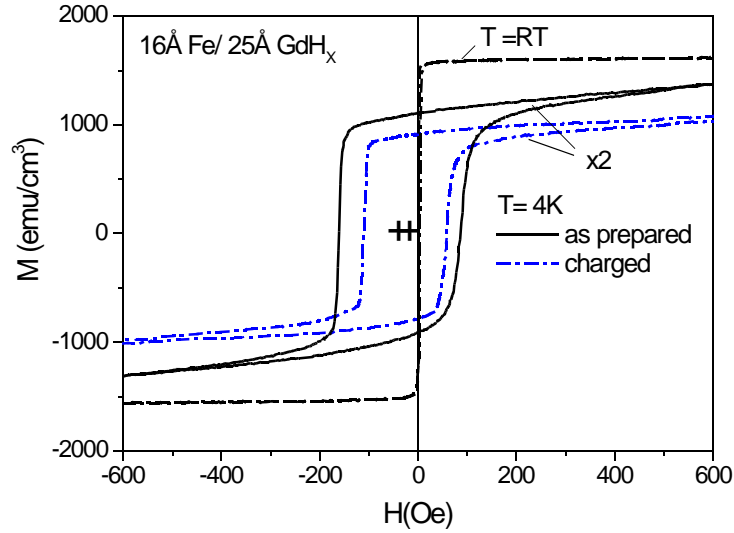Fe/GdH$_X$ system by tuning the electronic properties via the hydrogen content in the GdH$_X$ sublayer.

Figure 3.34. Hysteresis curves above the Néel temperature (solid line), and after field cooling in H=20 kOe. The field cooled curves are multiplied by factor of two. Dashed line: as-prepared sample (GdH$_{2-\delta}$ metallic). Dotted line: after additional hydrogen charging (GdH$_{3-\gamma}$ isolating).

A first impression of the magnitude of the exchange biasing induced by the AF order of the Fe/GdH$_X$ samples is shown for the 16Å Fe/ 25Å GdH$_X$ multilayer sample (figure 3.34). The magnetization M(H) for the field cooled curves is multiplied by a factor of 2 to provide a better comparison with the hysteresis curve measured at T=300K. At RT the coercive and saturation fields are very small with values below 20 Oe. With reaching the Néel temperature the saturation field is strongly enhanced. After cooling the sample in a magnetic field of 20 kOe to T=4 K, the coercive field rises due to the strong coupling at the interface by two orders of magnitude. Only 50% of M$_S$ is reached at 800 Oe and the remaining non saturated part of the 16 Å thick Fe layers is still coupled at the interface to the AF ordered GdH$_X$ layer. The center of the hysteresis curve is shifted on the field axis to negative field values. But the exchange bias is small; the value of the shift on

the field axis is marked with a cross. It is 40 Oe for the as-prepared sample with metallic $GdH_{2-\delta}$ sublayer and 22 Oe in case of the insulating $GdH_{3-\gamma}$ sublayer. This is only a factor of ~1/3 (1/4) of the coercive field H_C for the $Fe/GdH_{2-\delta}$ ($Fe/GdH_{3-\gamma}$) multilayer. After additional charging, the hysteresis is getting softer. The magnetization at H=800 Oe is lower than in the as prepared sample.

For a 16Å Fe/ 10Å GdH_X multilayer sample (not shown), the exchange-bias field for the uncharged sample is only 5 Oe and vanishes for the charged sample. This can be attributed to a rougher interface and smaller GdH_X-crystallite size resulting in frustration effects at the Fe interface and a higher number of grain boundaries which do not contribute to the exchange bias field. Thus the effect is rather small and should be improved by growing smoother interfaces and larger crystallites, e.g. with thicker GdH_X layers.

3.9 Summary - interface polarization at the metal-to-insulator transition

In this chapter XMCD spectra measured at the $L_{2,3}$ absorption edges of RE in multilayers Fe/REH_X are presented which essentially probe the 2p→5d dipole transition. Variation of the hydrogen concentration x permits to investigate the effect of the metal-to-insulator transition in the RE hydride. For the three systems investigated (RE: La, Ce, Gd) in this work the intensity of the signals is reduced by a factor of two in the insulating state. The data are analyzed by a phenomenological two parameter model. The parameters denoted as α and β decay exponentially on a length scale of about 10 Å from the Fe interface into the ReH_X sublayers. The analysis reveals that in the case of Ce and Gd the XMCD signal does not simply represent the Fe-induced magnetic polarization of 5d electrons in the ground state. It may be strongly influenced by the spin dependence of the

matrix element for the 2p→5d transition. This effect is the result of the 4f-5d exchange interaction. In the Fe/GdH$_X$ system the element selectivity of the XMCD permits to probe the antiferromagnetic transition in the GdH$_X$ sublayers near 20K.

1   J.N. Huiberts, R. Griessen, J.H. Rector, R.J. Wijngaarden, J.P. Dekker, D.G. de Groot, N.J. Koeman, Nature **380,** (1996) 231-234; R. Griessen, J.N. Huiberts, J.H. Rector, Hydrogen activated thin films switching device, US Patent: 5635729, filed May 7, 1996, European patent pending no. WO 96/38758; Japanese patent pending no. 98-503858

2   F. J. A. den Broeder, S.J. van der Molen, M. Kremers, J. N. Huiberts, D. G. Nadegast, A. T. M. van Gogh, W. H. Huisman, N. J. Koeman, B. Dam, J. H. Rector, S. Plota, M. Haaksma, R. M. N. Hanzen, R. M. Jungblut, P.A. Duine, und R. Griessen, Nature **394**, 656 (1998); P. Ball, Nature 391, **232** (1998)

3   F. Leuenberger, Diplomarbeit, Universität Göttingen (1999)

4   D. J. Peterman, J. H. Weaver, and D. T. Peterman, Phys. Rev. B **23**, 3901 (1981)

5   P. Vajda, *Handbook on the chemistry of the Rare Earths,* edited by J. K. A. Gschneider, and L. Eyring, Elsevier Science B. V., Vol. 7, p. 139 (1995)

6   R. R. Arons in Landolt Börnstein, *Zahlenwerte aus Naturwissenschaften und Technik*, New Series, Springer, Berlin Vol. III, 19dl, p. 280 (1991)

7   Peter Fulde, *Electron Correlations in Molecules and Solids*, 3rd edition, Springer Verlag Berlin, 1995, p. 281

8   M. Gupta, J.P. Burger, Phys. Rev. B **22**, 6074 (1980)

9   Introduction: Ashcroft , Mernim, *Solid State physics*, chapt. 11, p. 200

10   D. K. Mismer, B. N. Harmon, Phys. Rev. B **26**, 5634 (1982)

11   K. K. Ng, F.C. Zhang, V. I. Anisimov, and T. M. Rice, Phys. Rev Lett. **56**, 1311 (1997), K. K. Ng, F.C. Zhang, V. I. Anisimov, and T. M. Rice, Phys. Rev. B **59**, 5398 (1999)

12   R. Eder, H. F. Pen, and G. A. Sawatzky, Phys. Rev. B **56**, 10 115 (1997)

13   V.O. de Haan, G. G. Drijkonigen, Physica B **198**, 24 (1994)

14   W. Lohstroh, PhD thesis, Universität Göttingen (1999)

15   P. H. Dederichs, 'Spinabhängiges Tunneln', in *Magnetische Schichtsysteme*, 30. Ferienkurs IFF Jülich (1999)

17 G. A. Landrum, R. Dronkowski, Angew. Chem. Ed. **39**, 1560 (2000)

18 D. Stoeffler and C. Cornea, presented paper PB-78 at the "Symposium on Spin Electronics", Halle (2000)

19 J. Röhler in *Handbook of Chemistry of Rare-Earths*, ed. L. Erving and S. Hüfner, Volume 10, Chap.71, North Holland, Amsterdam 1991

20 G. Schütz. F. Rahm, P. Mautner, R. Wienke, W. Wagner, W. Wihelm und P. Kienle, Phys. Rev. Lett. **62**, 2610 (1998)

21 C. T. Chen, Y. U. Idzerda, H.-J. Lin, N. V. Smith, G. Meigs, E. Chaban, G. H. Ho, E. Pellgrin, and F. Sette, Phys. Rev. Lett. **70**, 694 (1993)

22 J. B. Goedkoop, A. Rogalev, M. Rogaleva, C. Neumann, J. Goulon, M. van Veenendaal and B.T. Thole, J. Phys. F. 7, C2-415 (1997)

23 M. Imada, A. Fujimori, Y. Tokura, Rev. Mod. Phys. **70**, 1040 (1998), p. 1049

24 M. Julliere, Phys. Rev. Lett. **54 A**, 225 (1975)

25 J. M. De Teresa, A. Barthélémy, A. Fert, J. P. Contour, F. Montaigne, and P. Seneor., Science **286**, 507 (1999)

26 J. S. Moodera, J. Nowak, L. R. Kinder, and P. M. Tedrow, R. J. M. van de Veerdonk, B. A. Smits, M. van Kampen, H. J. M. Swagten, and W. J. M. de Jonge, Phys. Rev. Lett. **83**, 3029 (1999)

27 S. Parkin, paper presented at Symposium on spin electronics, Halle 2000

28 M. Arend, W. Felsch, G. Krill, A. Delobbe, F. Baudelet, and E. Dartyge, J.-P. Kappler, M. Finazzi and A. San Miguel-Fuster, S. Pizzini, and A. Fontaine, Physical Review B **59**, 3707 (1999)

29 M. Arend, PhD thesis, Cuvillier Verlag Göttingen (1998)

30 R. R. Arons, J. Schweizer, J. Appl. Phys. **53**, 2645 (1982)

31 E. Dartyge, A. Fontaine, Ch. Giorgetti, S. Pizzini, F. Baudelet, G. Krill, Ch. Brouder, and J.-P. Kappler, Phys. Rev. B **42**, 3155 (1992)

32 J. C. Lang, X. Wang, V. P. Antropov, B. N. Harmon, A. I. Goldman, H. Wan, G. C. Hadjipanayis, K. D. Finkelstein, Phys. Rev. B **49**, 5993 (1994)

34   G. Schütz et al., Z. Phys. B **73**, 67 (1998)

35   J. P. Rueff, R. M. Galéra, S. Pizzini, A. Fontaine, L. M. Garcia, Ch. Giorgetti,
     E. Dartyge and F. Baudelet, Phys. Rev. B **55**, 3063 (1997)

36   R. R. Arons in Landolt Börnstein, *Zahlenwerte aus Naturwissenschaften und
     Technik*, New Series, Springer, Berlin Vol. III, 19dl (1991)

37   Müller, Balckedge, Libowitz, *Metal Hydrides*, Academic Press, 1968

38   A. E. Berkowitz, K. Takano, J. Magn. Magn. Mater. **200**, 552 (1999)

4. Ce-4f configuration in Fe/Ce$_{1-X}$Si$_X$ multilayers

4.1 Introduction

Previous studies have revealed that the α- and γ-phase-like electronic configuration of Ce (chapter 2.1) can be stabilized in the multilayers Fe/Ce [1] and Fe/CeH$_{2-\delta}$, respectively. The absorption of hydrogen in Ce reduces the 4f-valence band hybridization, due to an expansion of the lattice, and leads to a relocalization of the 4f states. The result is a profound modification of the magnetic properties. A gradual transition by hydrogenation between these configurations is not possible because of the very small primary solubility of H in Ce: a two-phase structure appears if the solubility is transgressed (chapter 3.2). The experiment performed on the Fe/Ce$_{1-X}$Si$_X$ multilayers is conceived to induce a smooth progression of the 4f-states in the multilayers from itinerancy to localization, i.e. between the α and γ -like configurations by increasing the content x of the s-p element Si. It is the aim to study the impact of this effect on the Ce-L and M isotropic and XMCD spectra. In fact, experiments on thin films had shown [2] that small quantities (<10%) of Si stabilize the γ-like electronic configuration of Ce, with weak or negligible 4f-conduction-electron hybridization. The inter-metallic CeSi$_X$ with Si contents $1.5 \leq x \leq 2$ has attracted much interest because of its low-temperature properties [3]. They are intimately related to the localized 4f-electron states and governed by a competition of the Kondo effect and magnetic ordering which occurs through the RKKY interaction. Both effects arise from exchange interaction between the 4f and conduction electrons. For x<1.84 the ground state of the system is magnetically ordered, above this Si concentration magnetic order is suppressed

[4,5]. In amorphous $CeSi_X$-alloy films magnetic order could not be detected for all Si contents between $0.5 \leq x \leq 4.5$ investigated [6]. Above 100 K the susceptibility follows a Curie-Weiss law with an effective moment derived from a $4f^1$ configuration. A very large Sommerfeld coefficient of the electronic specific heat was detected for these samples, similary as in Heavy Fermion systems. This indicates the presence of strong correlations involving the 4f and conduction electrons.

It is a surprise of the present investigation that in the $Fe/Ce_{1-X}Si_X$ the presence of Fe has a considerable influence on the electronic structure of Ce: the α-like configuration is preserved up to much higher concentrations than in the single alloy layers.

4.2 Structural properties

4.2.1 X-ray diffraction

The structural properties of the $Fe/Ce_{1-X}Si_X$ multilayer samples is investigated with small-angle and high-angle X-ray diffraction to yield informations on the crystal structure of the sublayers and the quality of the interfaces (chapter 1.2). Results are presented in figure 4.1. The thickness of the multilayer stack is ~ 4000 Å for all samples.

The small-angle reflectivity is plotted in figure 4.1 on the top and reveals very strong Bragg peaks even for large angles of $10°$ ($q = 0.69$ Å^{-1}) indicating smooth interfaces. A comparison with the corresponding data of the Fe/Ce multilayers [7] indicates that the chemical super-structure of $Fe/Ce_{1-x}Si_x$ multilayers for $x=0.1$ shows substantially the same interface roughness of about 1 monolayer. With increasing Si concentration x, the structural interface quality is even improved as it can be seen in figure 4.1 at the top for $x=0.65$ of the Ce_xSi_{1-X} sublayer. There is no thickness dependence of the interface quality. Even for a thickness of 10 Å Fe,
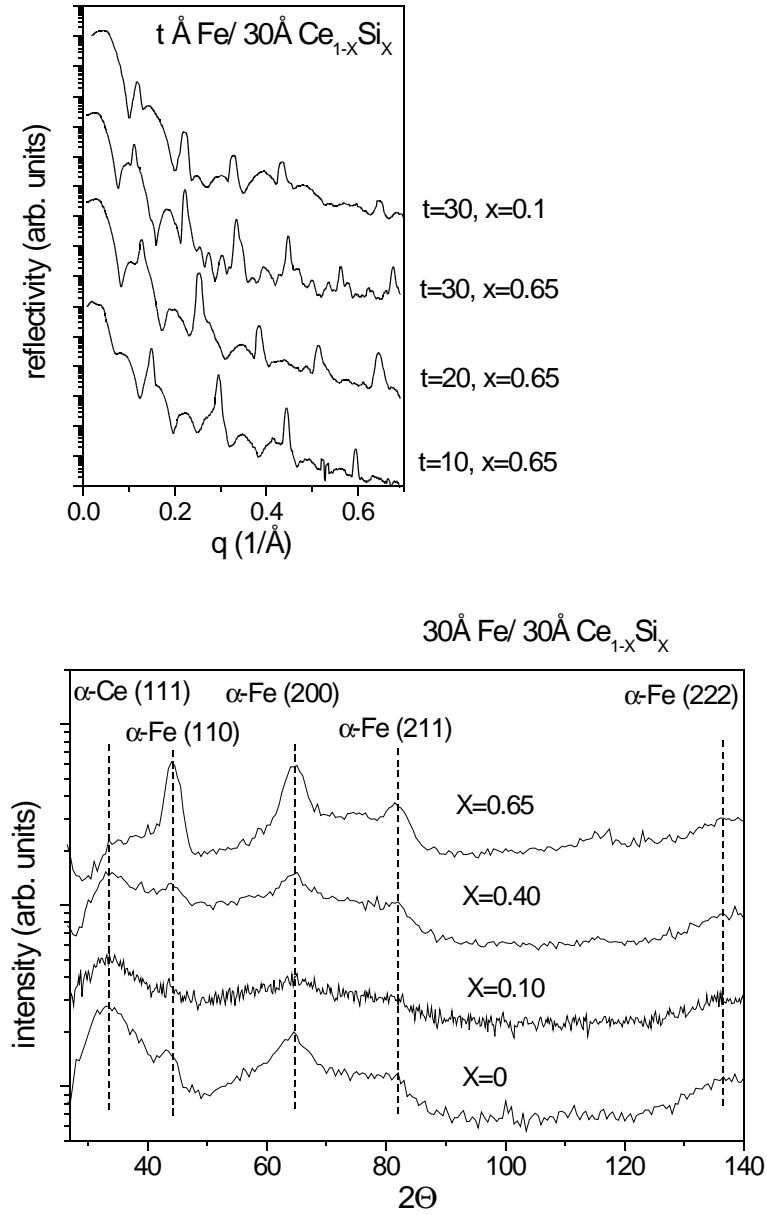
Figure 4.1. Small-angle X-ray reflectivity of the layered chemical superstructure, superposed by fringes of the Cr-cap layer (top). In the high-angle diffraction data region, only very weak peaks signal the amorphous CeSi-alloy. The positions of the bcc-Fe crystalline peaks are marked (bottom).

sharp Bragg peaks of the superstructure are visible. There is no hint indicating a Fe$_{1-x}$Si$_x$ interface alloy.

The high-angle X-ray diffraction data maintains only weak intensity of the reflexes even for long counting rates of 120 s per step. The $Ce_{1-x}Si_x$ sublayers are amorphous: there is a broad α-Ce(111) peak which vanishes and moves towards larger angles with increasing Si content. Of much more interest is the evolution of the Fe reflections as function of the Si concentration. They are assigned to a bcc structure. For x=0.1 only broad maxima are visible. They increase rapidly above x=0.4 and become sharp for x=0.65. Applying the Debeye Scherrer formula, the crystallite size is estimated to be between 26-30Å in growth direction. There is no texture. Note that even for x=0.1 an amorphous structure of Fe can be excluded since otherwise the multilayer would not be ferromagnetic at room temperature [7].

4.2.2 Magnetic interfaces: ^{57}Fe Mössbauer spectroscopy

Mössbauer spectroscopy provides essential information on the interaction at the interfaces of the multilayers and on the interfacial mixing. The ^{57}Fe Mössbauer conversion electron spectra are measured by P. Schaaf [8] (figure 4.2, left). The spectra are magnetically split, revealing the ferromagnetic nature of the samples. The dominating contribution to the spectra is the magnetically split sextet spectrum with the magnetic hyperfine field of bcc-Fe. The asymmetry of the lines and a broad background feature in the middle of the spectra indicate inequivalent Fe environment and hence need a further analysis. As previously [9] the spectra were decomposed into a sextet representing the normal bcc-Fe part in the core of the Fe layers, and a probability distribution $p(B_{hf})$ of magnetic hyperfine fields B_{hf} attributed to Fe affected by the interfaces [10]. This model is adapted to the layered structure of the samples. The resulting hyperfine-field distributions $p(B_{hf})$ related to the interfaces are compared in figure 4.5 on the right.

The contribution of the interface component to the total intensity of the spectrum corresponds to a nominal Fe-layer thickness of 8-10 Å per interface, depending on
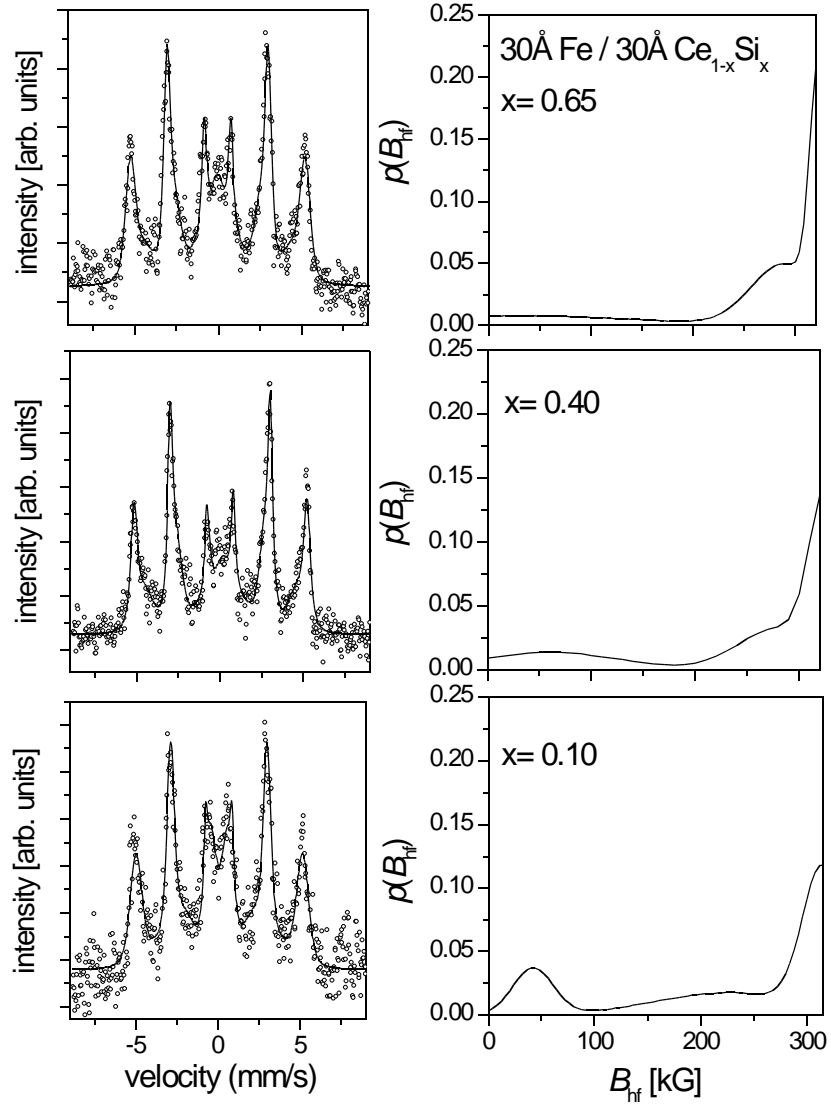
Figure 4.2. Left: ^{57}Fe Mössbauer conversion electron spectra at room temperature for Fe/Ce$_{1-X}$Si$_X$ multilayers. Solid lines: fits described in the text. Right: hyperfine field distributions p(Bh$_f$) corresponding to the interface contribution of the spectra.

the Si concentration. This points to a magnetic interaction of Fe with Ce and/or Si on a length scale exceeding the interfacial roughness and mirrors a modification of the Fe electronic structure near the interfaces. The hyperfine field distribution $p(B_{hf})$ presents characteristic structures. As argued before [9], these structures may be assigned to different parts of the interface. For x=0.1 there is a pronounced

maximum at 45 kG which represents Fe atoms next to the interface. Its contribution to the total intensity of the spectrum corresponds to 2.5 Å per interface, i.e. nominally one monolayer of Fe. This value is compatible with the structural roughness derived from X-ray small-angle diffraction data. The same feature was observed for the Fe/Ce multilayers and attributed to a weak magnetic interface alloy. The signature gets broader for x=0.4 and becomes very flat for x=0.65. For the highest Si concentration x=0.65 a symmetric doublet has to be added to get a close fit of the Mössbauer spectrum. It indicates the presence of a small amount of paramagnetic Fe (1.5 Å per interface) and may point to the formation of a nonmagnetic silicide. It is an important result, that the Mössbauer spectra and small-angle X-ray diffraction data excludes the formation of such silicides which usually form very easy, on a large scale of the multilayer. This must be due to the presence of Ce.

The magnetic properties of Fe in the multilayers were further characterized by their macroscopic saturation magnetization measured by vibrating-sample magnetometry (VSM). The easy axis of the magnetization is in the plane of the layers. The magnetic moments at saturation resulting from VSM are compared in figure 4.3 with estimations of the magnetic moments of Fe obtained from XMCD spectra recorded at the Fe-$L_{2,3}$ edges and their analysis by the sum rules. These spectra and details of the analysis are not presented here, only the result is shown (figure 4.3). The value of the macroscopic magnetization yield a value of about 2.2 μ_B/Fe, atom which is that of bulk bcc-Fe, but somewhat reduced for the value of the highest Si concentration of x=0.65. This reduction corroborates with the results from Mössbauer spectroscopy which show that about 10% of Fe are nonmagnetic in this multilayer. The Fe magnetic moments estimated from the measurements of the XMCD are somewhat reduced compared to the macroscopic values but show the same trend. Such absolute discrepancies are not uncommon, they are usually related to problems with the applicability of the sum rules [11].
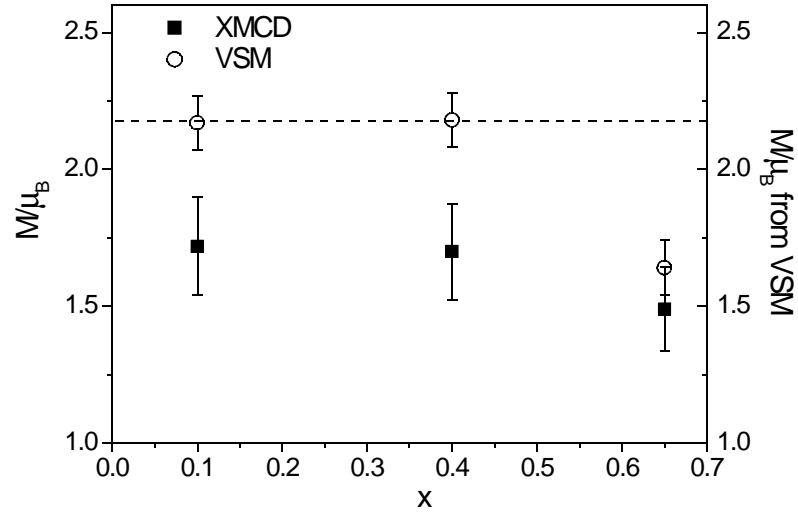
Figure 4.3. Magnetic saturation moment in Fe/Ce$_{1-X}$Si$_X$ multilayers obtained from VSM (circles) and XMCD spectra at the Fe-L$_{2,3}$ edges (squares) at room temperature.

4.3 The 4f configuration of Ce in the multilayers Fe/Ce$_{1-x}$Si$_x$

The 4f electronic configuration in the Ce ground-state can be explored by XA spectroscopy at the 2p→5d (L$_{2,3}$) and 3d→4f (M$_{4,5}$) excitation thresholds. Figure 4.4 shows the isotropic Ce-L and M absorption spectra obtained for the multilayer 30Å Fe/ 30Å Ce$_{1-x}$Si$_x$. As before, the thickness of the multilayer stacks is ~4000 Å for the measurements at the L$_{2,3}$ edges and the total RE thickness of the samples prepared for the measurements at the M$_{4,5}$ edges is ~150Å (chapter 1.1 and 1.4).

The M$_{4,5}$ edge probes the 4f ground state configuration more directly than the L$_{2,3}$-edge spectra, in which it is involved as a result of a final-state effect due to the interaction of the 2p-core hole with the 4f configuration [12]. Traditionally, this spectroscopy at the Ce-L$_{2,3}$ edges has been more frequently applied to the Ce systems in order to distinguish between the γ- or α-phase-like electronic

structures. The former leads to a white line profile, as it is observed in Fe/CeH$_X$ multilayers (chapter 3.7), the latter into a double-peak structure which is observed in the spectra in figure 4.4. The energy separation of both peaks is about 8 eV. In the L$_1$ spectrum involving an excitation into the unoccupied p-valence states the α -like configuration is represented as a two step profile.

We first focus on the study of the L$_2$ and L$_3$ edges. The double-peak structure in the spectra reveals that the 4f states of Ce in the multilayers are in an α-phase like electronic configuration. But the gradual reduction of the intensity of the peak at the high photon-energy with increasing Si concentration indicates a modification of the 4f configuration as Ce is substituted by Si. Unfortunately, a rigorous interpretation of the measured Ce-L$_{2,3}$ edge spectra is a difficult task. In the photo-absorption process the 4f-electron configuration interacts strongly with the 2p core hole. This leads to a reordering in energy of the 4f levels. As a consequence, different 4f configurations mixed in the ground state manifest themselves as separate structures in the L$_{2,3}$-edge profiles. Hence these profiles, even though they are determined by final-state effects, are closely related to the initial 4f configuration. In a phenomenological approach [13] widely used as an analysis tool by the experimentalist, the configuration of the electronic ground state of Ce, characterized by the 'effective occupation number' of the 4f states, $n_{4f} \leq 1$, is deduced from the deconvolution of the L$_{2,3}$ edge spectra: The two-line structure related to α–like Ce systems is interpreted as a superposition of two white-line resonances with the final states $2p^5 4f^1 5d^n$ and $2p^5 4f^0 5d^{n+1}$ (they are superposed to a step-like intensity distribution associated with excitation into the continuum states, see chapter 3.7, figure 3.11). The 4f ground state occupancy n_{4f} then is simply obtained from the relative intensity of the two white lines which are described by a Lorentzian; their width is proportional to the width of the 5d band (chapter 2.7). It is evident that this interpretation cannot be rigorously true. More elaborate models are required to interpret these spectra. In fact, Kotani et al. have
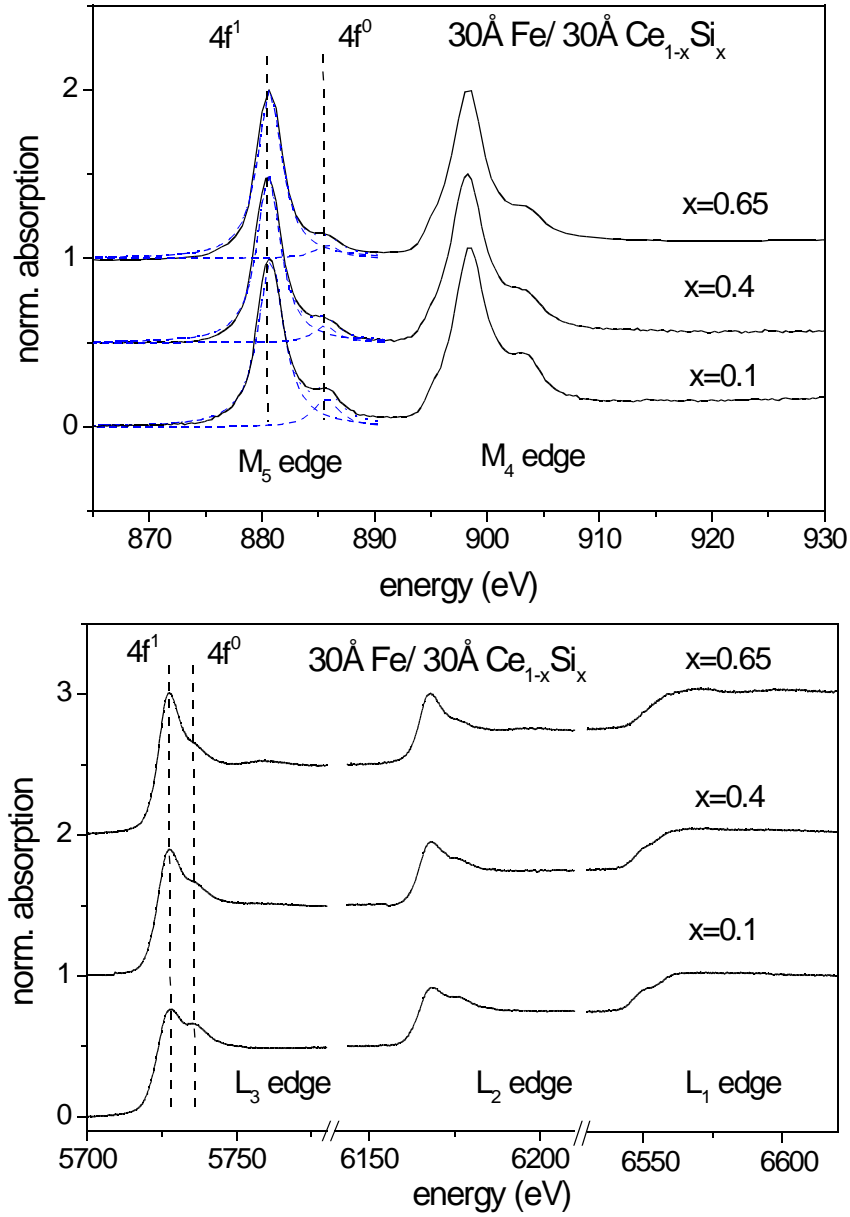
Figure 4.4. M$_{4,5}$ (top) and L$_{1,2,3}$ (bottom) edges for the Fe/Ce$_{1-x}$Si$_x$ multilayer. The Si concentration is varied from x=0.1 to x=0.65. Two transitions 4f^1 and 4f^0 are resolved. The M$_{4,5}$ edges are normalized to the M$_5$ amplitude. For the L edges, the jump at the absorption edges is normalized to 0.5 for the L$_3$, and to 0.25 for the L$_2$ and L$_1$ edge. Dashed lines: fit as described in the text. The fit for the XAS at the L$_2$ edge is not shown.

shown [14] that the theoretical description of the $Ce\text{-}L_{2,3}$ absorption process must involve the interaction of the photoelectron and the electronic system in the final state. Malterre has extended their calculations by taking into account the hybridization of the photoelectron and the conduction band states [15]. He finds that the $L_{2,3}$ near-edge spectra of Ce yield a reliable image of its ground state configuration. Hence the phenomenological analysis of the $L_{2,3}$ spectra, even if the approach is oversimplified, should provide a satisfactory measure of the 4f occupancy n_{4f} in the ground state, at least in the Ce-α phase. However, it is questionable if the $L_{2,3}$ spectroscopy can yield the correct value of n_{4f} if n_{4f} approaches 1 and the intensity of the second feature vanishes.
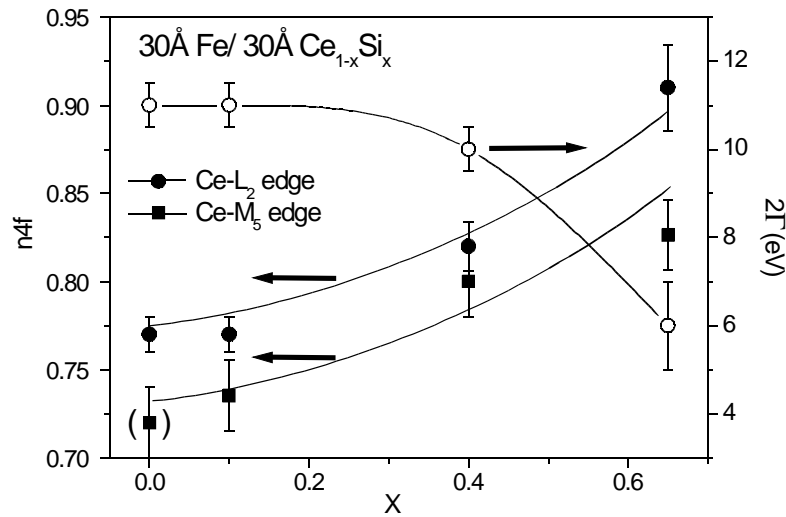

Figure 4.5. Occupation of the 4f-orbital extracted from the analysis L_2-absorption edges (circles) and M_4 edges (squares) for the multilayers 30Å Fe/ 30Å $Ce_{1-x}Si_x$ as a function of the Si concentration. Also shown: the line width 2Γ resulting from the phenomenological analysis at the L_2 edge (open circles). The value marked with brackets is for a $Ce_{1-x}Si_x$ thickness of 10 Å.

The Ce 4f-state occupancy n_{4f} extracted from the L_2-absorption spectra as well as the linewidth 2Γ, which is correlated with the 5d bandwidth, is reported in figure 4.5. For low Si concentration $x \leq 0.1$ n_{4f} adopts the minimum value reached by

α-Ce metal exposed to an external pressure [13], hence Ce is in a phase with α-like electronic configuration. With increasing x there is a continuos increase of n_{4f} up to 0.9 which reflects a gradual reduction of the strength of the 4f-conduction electron hybridization, i.e. an increasing degree of localization of the Ce-4f states in the multilayers. In fact, at the highest Si content x=0.65 n_{4f} is closed to that of the γ-phase. This is corroborated by the evolution of the linewidth which decreases from above 10 eV expected for α-like Ce in these multilayers to 6 eV expected when the γ-like Ce phase is approached [16].

The Ce-M$_{4,5}$ absorption spectra reveal a similar evolution (figure 4.4, top). They consist of two resonances well separated by the $3d^9$ spin-orbit splitting. Each resonance is characterized by a two-peak structure which corresponds to the final-states $3d^9 4f^2$ (main contribution) and $3d^9 4f^1$ (satellite at the high photon-energy end). They are directly related to the initial $3d^{10} 4f^1$ and $3d^{10} 4f^0$ configuration since the absorption process involves the transition into the 4f configuration. This feature confirms the α-like character of Ce in the multilayers. In contrast, in γ-like Ce systems the M$_4$ and M$_5$ resonances exhibit a fine structure arising from the exchange splitting of the $3d^9 4f^2$ final state which is well described by atomic multiplett calculation [17]. The fine structure is smeared out in α-like systems. The theoretical description of the M$_{4,5}$ absorption thresholds in highly correlated Ce systems appears to be much clearer than that of the L$_{2,3}$ edges [12,18]. Thus it is possible to adjust the experimental n_{4f} values, extracted from the intensity ratios of the $4f^1$ and $4f^0$ channel at the M$_{4,5}$ edge (figure 4.4), in order to determine the correct value of n_{4f} in the ground state. The numbers are close to the ones resulting from the L$_{2,3}$ profiles (figure 4.5) with a systematic shift to lower values [19].
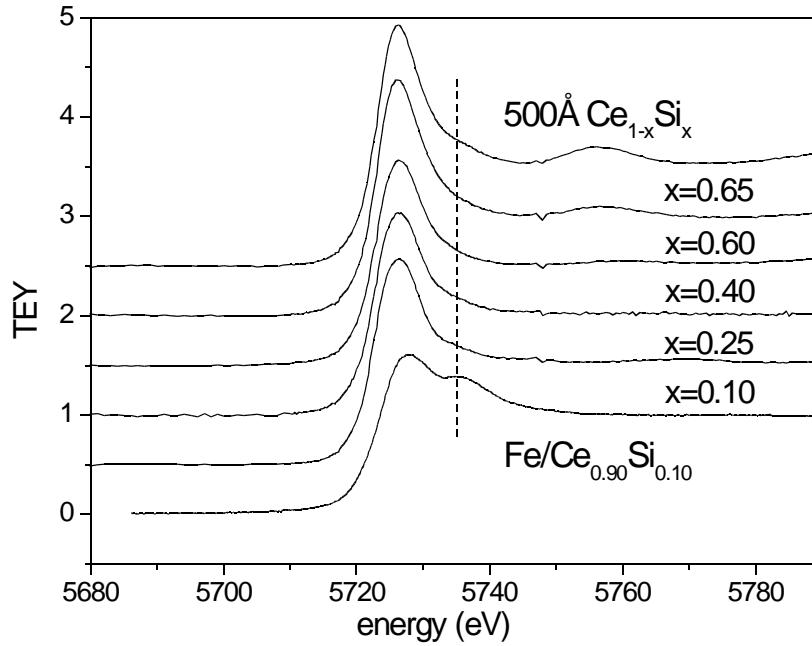
Figure 4.6. Absorption measurements at the Ce-L₃ edge Ce₁₋ₓ Siₓ films measured with total electron yield (TEY) and the multilayer Fe/Ce₀.₉ Si₀.₁ as a reference (top).

The 4f-electronic configuration of Ce is different in single $Ce_{1-x}Si_x$ films. This is visible in the Ce absorption spectra presented in figure 4.6, which in this case are obtained by measuring the total electron yield (TEY). The alloy films are prepared under the same conditions as the multilayers with Fe. They grow in an amorphous structure. Obviously Ce is in the γ-like configuration in these films already at x=0.1. The estimated 4f occupation number is ranging between 0.94 (x=0.10) and 1 (x=0.65). The value of n_{4f} is difficult to extract from the L_3 spectra due to the small $4f^0$ contribution. This agrees with the previous results obtained for the alloys [2]. Apparently the intercalation between Fe in the multilayers stabilizes the α-like Ce configuration to considerably high Si concentration, presumably due to the stress at the interfaces as in the pure Fe/Ce multilayers [1]. For the single $Ce_{1-x}Si_x$ films, the amplitude of the white line at the L_3 edge, A_{4f^1}, increases about 35% as the Si concentration is raised to x=0.65. This visualizes a change in the electronic

structure, i.e. a charge transfer from the Ce-5d band to the s-p orbitals of Si which form the covalent bonding.

It can be seen in figure 4.6 that with increasing Si concentration in the alloy films an oscillation in the Near Edge X-ray Absorption Fine Structure (NEXAFS) appears at 5750 and 5790 eV. This NEXAFS feature is present in the spectra of the multilayers as well and indicates a structural change in the Ce environment on the scale of the atomic distance. Note that a structural change in the layers as a function of the Si content is seen in the X-ray diffraction data as well (chapter 4.2.1).

In conclusion, the X-ray absorption experiments discussed in this section reveal that it is possible to model the electronic structure of the Ce sublayers to a certain extent by alloying with Si: the degree of localization of the 4f states is determined by the concentration of the s-p element Si.

4.4 Dichroism at the Ce-M$_{4,5}$ edges

The XMCD spectra at the M$_{4,5}$ edges are measured in transmission at the beamline SU 23 of Super ACO at LURE. All spectra are collected with an angle of 40° between magnetic field vector and layer normal. At room temperature the dichroic signals are very small (<0.5% of the white line without normalization to the polarization rate) and beyond the instrumental resolution. Therefore all XMCD spectra are recorded at 10 K. An average over four spectra for each acquisition is shown in figure 4.7a. The spectra are normalized to the M$_5$-white line and to 100% polarization rate of the photons (25.8% at the M$_5$ and 20.8% at the M$_4$ edge). With increasing Si concentration the intensity of the signals increases by a factor of up to two. In figure 4.7b, the amplitudes of the M$_4$ and M$_5$ maxima are plotted as a function of the Si concentration.
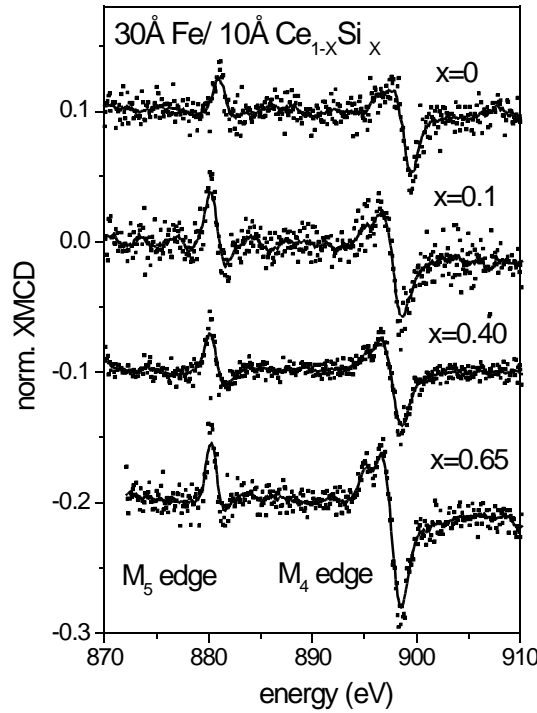
Figure 4.7a. XMCD spectra at the Ce-M$_{4,5}$ edges for the samples 30Å Fe/ 10Å Ce$_{1-x}$Si$_x$. The spectra are measured at a temperature of 10 K for different concentrations x=0, 10, 40, 65.

The ratio of the M$_4$/M$_5$ amplitudes does not change significantly. It is astonishing that the dichroic signal increases with decreasing the Ce content. This means, that in the more diluted Ce alloy the polarization of the 4f moments is even more effective. This can be attributed to the increased 4f-state occupation leading to a stronger 4f-5d exchange interaction. It has to be expected that the changed magnetic moment on the 4f electron will be mirrored in the line shape of the XMCD spectra at the Ce-L$_{2,3}$ edges. This will be discussed in the following paragraph.
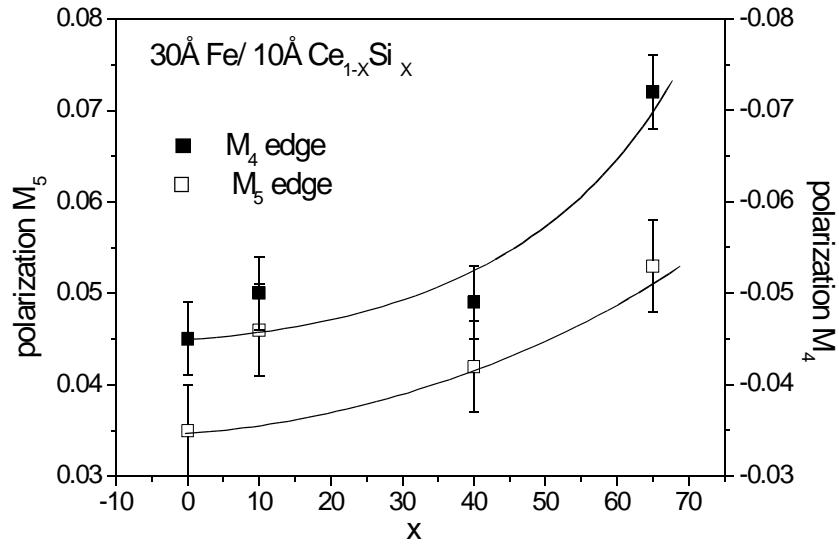
Figure 4.7b. The amplitudes of the XMCD signals at the maxima of the M$_4$ (negative peak) and M$_5$ edges are plotted as a function of the Si concentration.

4.5 Dichroism at the Ce-L$_{2,3}$ edges

The dichroic signals at the L$_{2,3}$ edges are measured at the energy dispersive beamline D11 at the DCI storage ring of LURE between 10 K and 300 K for two angular positions. The spectra are normalized by the jump at the absorption edge and to 100% polarization rate of the photons. The dichroic signal is measured by flipping the magnetic fields between ±20 kOe. For this field value the samples are fully saturated in the 'grazing incidence' geometry with an angle of 60° between magnetic field and layer normal, and saturated to about 90% for the normal incidence. At the L$_1$ edge where an excitation into the p-hole states occurs, no dichroic signal could be detected despite of the possibility of a magnetic polarization transfer by p-s hybridization with Si. For the L$_2$, L$_3$ transitions into the 5d-hole states the dichroism is about 0.5-1% of the absorption edge.
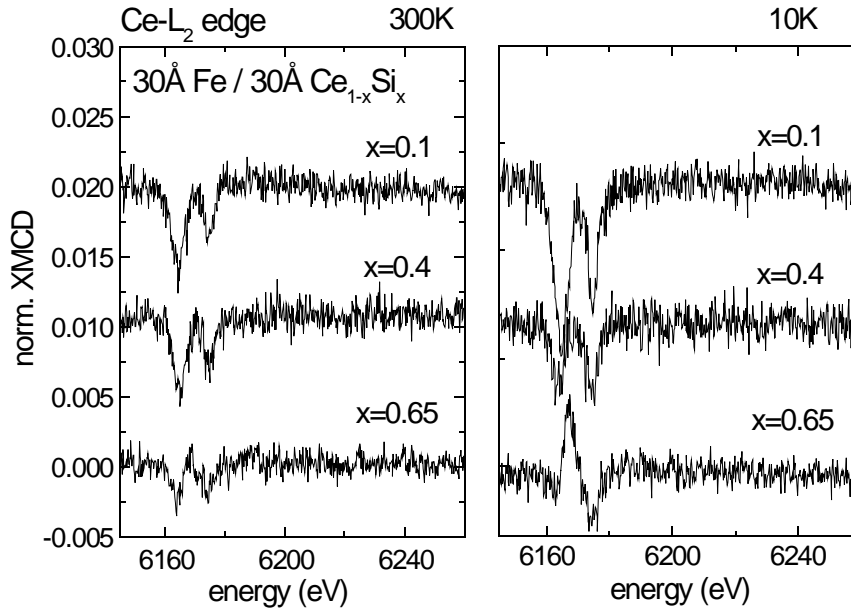
Figure 4.8. XMCD spectra measured at the Ce-L_2 edge for the 30Å Fe/ 30Å $Ce_{1-x}Si_x$ multilayer as a function of the Si concentration. The spectra are measured at room temperature (left) and 10K (right) in normal transmission.

In figure 4.8 the dichroic L_2 spectra at 300 K are plotted for the different Si concentrations of the $Ce_{1-x}Si_x$ sublayers. The spectra at room temperature exhibit the double peak structure already observed previously for the Fe/Ce multilayers [1] where Ce is α-like. This signature reflects the $4f^0$ and $4f^1$ final-state contributions. The shape of the spectra is quite different at 10 K. For the lowest Si content, an increase of the signal of about a factor two is observed. For x=0.4, the peak intensities of the dichroic spectra are equal for both transitions and for the highest concentration of x=0.65 even a reversed sign is observed. This quite complex shape of the XMCD signal in the latter case is similar to the dichroic spectra of the $Fe/CeH_{2-\delta}$ samples discussed in chapter 3.8.2. Thus, it seems to be connected to the increased localization of the 4f states at this Si content.

At the Ce-L_3 transition (figure 4.9) the XMCD spectra simply exhibit the typical
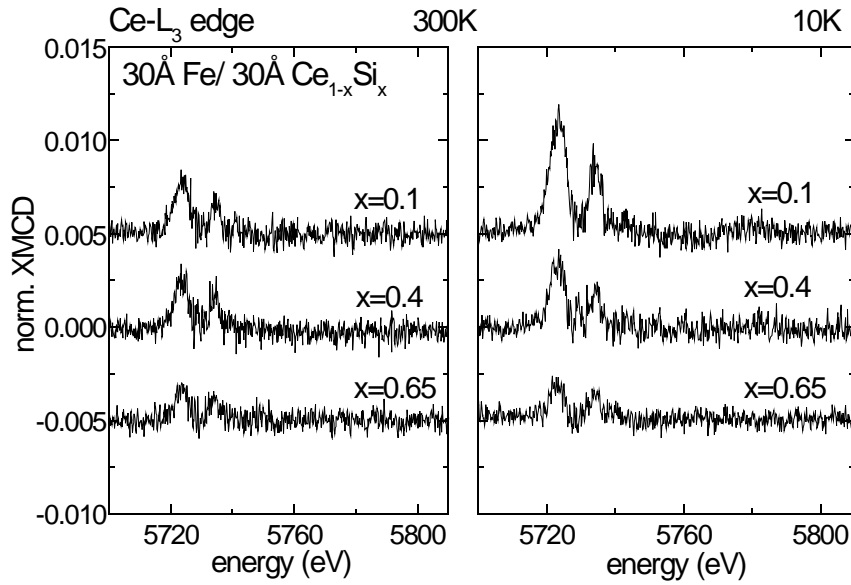
Figure 4.9. XMCD spectra measured at the Ce-L$_3$ edge for the 30Å Fe/ 30Å Ce$_{1-x}$ Si$_x$ multilayers as a function of the Si concentration. The spectra are recorded at room temperature (left) and 10K (right). Here the spectra are measured in grazing incidence (at 60° with respect to the layer normal).

double peak structure related to the 4f^1 and 4f^0 to the final state. The amplitude of the dichroic signals decreases monotonously with the Si concentration. Compared to the spectra measured at the L$_2$ edge the L$_3$ spectra are less sensitive to a variation of the temperature, in particular for the highest Si concentration of x=0.65. The anomalous behavior of the spectra presented in figures 4.8 and 4.9 is reflected in the ratio L$_2$/L$_3$ of the XMCD intensities.

The L$_2$/L$_3$ branching ratios are plotted in figure 4.10 as a function of the Si concentration in Ce-sublayers. At room temperature the values are near -2. This is known from compound CeFe$_X$ and the Fe/Ce multilayers [1,16], where the orbital 5d moment is quenched. The situation is different at 10K for the highest Si concentration. Here, the L$_2$/L$_3$ ratio changes its sign and amounts to +2.5. This is not an indication for directional change of the magnetic 5d moment similarly as in
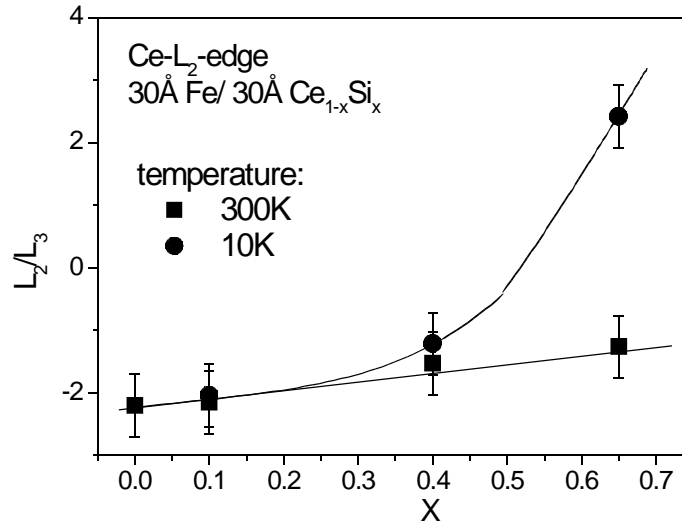
Figure 4.10. Ratio of the amplitudes (at the low energy peak) of the L_2 and L_3 XMCD signals of Ce measured for the multilayers 30Å Fe / 30Å $Ce_{1-x}Si_x$ at 300 K and 10 K.

the Fe/CeH_X multilayers (chapter 3.8.2). The variation of the XMCD at the L_2 edge in form and amplitude is related to the 4f-5d magnetic moment interaction.

As remarked above, the shape of the XMCD spectra at the Ce-$L_{2,3}$ are very similar for the $Fe/Ce_{0.35}Si_{0.65}$ and the $Fe/CeH_{2-\delta}$ multilayers. But, in the case of the hydride system a strong dependence of the XMCD in shape and amplitude as a function of the angle between the magnetic field which is parallel to the beam and the layer normal is observed. It is related to the magnetocrystalline anisotropy of the multilayers which induces a perpendicular magnetization orientation at low temperatures [19]. For the $Fe/Ce_{1-X}Si_X$ samples, the magnetization is oriented in the layer plane at all temperatures. Thus no anisotropy in the XMCD signals is expected to be present.

This can be examined in figure 4.11 where the spectra measured at 0° and 60° with respect to the layer normal at 300 K and 10 K are shown. The line shape is very similar for both positions. The spectra recorded under the same conditions for
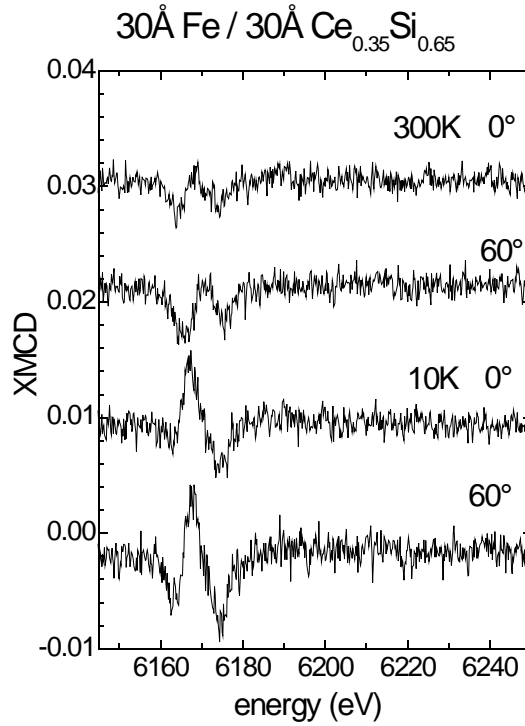
30Å Fe / 30Å Ce$_{0.35}$Si$_{0.65}$

Figure 4.11. Spectra at the Ce-L$_2$ edge for the highest Si concentration of x=0.65. The spectra are compared at two temperatures for an angle of 0° and 60° respectively. The spectra measured in normal incidence (0°) are corrected for incomplete saturation which is near 90% for H=20 kOe.

the multilayer sample with x=0.1 to prove the absence of an angular anisotropy as well. The interpretation of the Ce-L$_{2,3}$ XMCD spectra of the Fe/Ce$_{1-X}$Si$_X$ multilayer is difficult since a real theory of such RE spectra does not exist. The similarities of the dichroic signals for the sample with x=0.65 and the hydrided multilayers Fe/CeH$_{2-\delta}$, and in particular the large positive L$_2$/L$_3$ ratio at low temperature in case of the Si alloy (figure 4.12), suggest that the exchange interaction between the 5d and 4f electrons of Ce has an important influence on the dichroism of the Fe/Ce$_{0.35}$Si$_{0.65}$ heterostructure. This is supported by the observation of an increased 4f-state occupation, i.e. an increased localization of the 4f states in the Ce$_{1-X}$Si$_X$ sublayers (section 4.3). However, it must be kept in mind that the Ce-4f

configuration is quite different in the two systems: it is γ-phase like in the hydride but α-like in the alloy with Si even for the highest Si content of this element. In the following the phenomenological α-β model (chapter 2.8) is applied to analyze the temperature dependence of the XMCD at the L_2-absorption edge. The $4f^0$ channel is described with an additional Lorentzian function. This procedure is based on the analysis of the white lines widely applied to extract the occupation number of the 4f states (chapter 4.3).
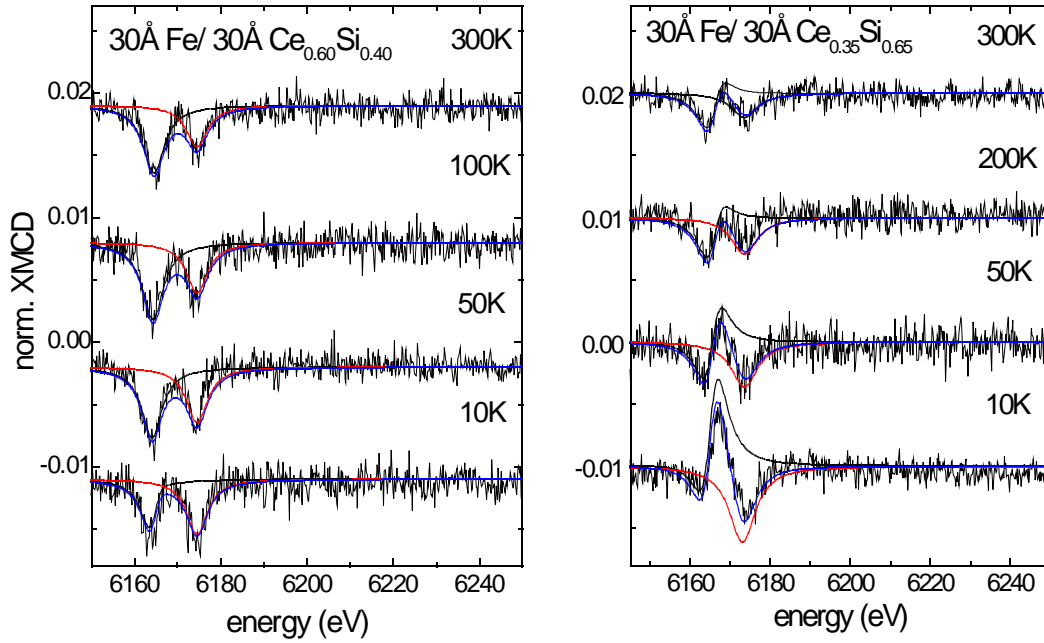

Figure 4.12. Analysis of the XMCD spectra at the Ce-L₂ edge with the α-β model. As lines, the fit for the first transition (parameters α ,β) and second transition as well as the sum are shown. Left: Si content x=0.4 Right: Si content x=0.65.

The results of the analysis of the white-line spectra are used as initial parameters (width $2\Gamma=8$ eV, the amplitudes A_L and the ratio R of the $4f^1$ and $4f^0$ contributions) and thus only α, β and the polarization of the $4f^0$ channel are used as free parameters as described in chapter 2.8. The fits for the Si concentration

x=0.1 are not shown here, but reveal an equal change of the amplitude for both transitions. The analysis of the curves shown for the Si concentration x=0.4 and x=0.65 describes the evolution of the spectra as a function of the temperature quite reasonable and both channels 4f^1 and 4f^0 can be separated (figure 4.12). For x=0.4 the amplitude of the first transition slightly decreases with temperature. For x=0.65, the 4f^1 transition reveals a gradual variation from a dominating negative XCMD at 300 K to a strong positive feature at low temperatures.

The values of the parameters α and β extracted from the analysis are given in figure 4.13. The vanishing β for x=0.1 in the entire temperature range suggests that for this Si concentration the 4f-5d exchange is negligible. This means the XCMD signal represents the spin polarization of the Ce-5d band in the ground state. For x=0.4 a slight decrease of α goes along with a non-zero β value for 10 K and produces the decrease of the amplitude of the first transition in the XMCD spectrum, which gets slightly asymmetric in addition.

The growing importance of the breathing effect, i.e. the spin dependence of the transition matrix element for the 2p→5d transition which competes with the contribution of the 5d spin polarization to α (chapter 2.8), is reflected for x=0.65. Here α is very small at 300 K and changes sign at 50 K. Upon lowering the temperature the XMCD spectrum at the 4f^1 transition is varying gradually towards a pure derivative line shape at 50 K, revealing the influence of the β factor as α crosses zero, and changes the sign for 10 K. These dependencies point to an increased influence of the 4f-5d exchange interaction on the Ce-L$_2$ spectra at high Si concentrations and low temperature. For the same reason β increases with increasing Si concentration and decreasing temperature.
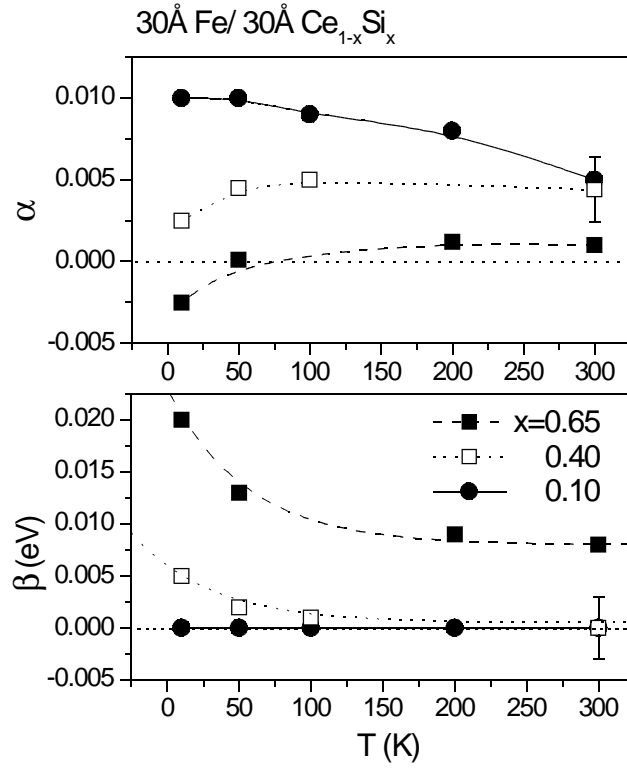
Figure 4.13. Parameters extracted from the fit with the α-β model at the Ce-L$_2$ edge. The values of the 'breathing' α and the energy shift β are plotted as a function of the temperature for the different Si concentrations of the Ce$_{1-x}$Si$_x$ sublayers. The data values are fitted with an exponential decay function as described in the text.

The variation of the parameters α and β may be described by the functions

$$\alpha(T) - \alpha_{x=0.1}(T) = A^{\alpha} e^{\frac{-T}{T_0^{\alpha}}} + A_0^{\alpha} \qquad\qquad 4.2$$

$$\beta(T) \qquad\quad = A^{\beta} e^{\frac{-T}{T_0^{\beta}}} + A_0^{\beta}$$

with the constants $T_0^{\alpha,\beta}$, $A_0^{\alpha,\beta}$ and $A_0^{\alpha,\beta}$ listed in table 4.2. For $\alpha(T)$ the values $\alpha_{x=0.1}(T)$ with a Si content of x=0.1 are substracted as a reference without breathing effect.

		T$_0^i$	**A^i**	**A$_0^i$**
x= 0.40	*i=α*	*140 K*	*- 0.8·10^{-2}*	*0*
	i=β	*55 K*	*55 meV*	*0.5 meV*
x= 0.65	*i=α*	*160 K*	*-1.1·10^{-2}*	*-0.2·10^{-2}*
	i=β	*55 K*	*15 meV*	*8 meV*

Table 4.2. Constants entering equations 4.2 describing the temperature dependence of α and β with an exponential fit.

4.6 Summary

The measurements at the L$_{1,2,3}$ and M$_{4,5}$ absorption edges of Ce in the Fe/ Ce$_{1-X}$Si$_X$ multilayer show that, for the alloy range discussed here, the 4f-state of the Ce can be tuned from delocalized for low Si concentrations to more localized for high concentrations. This is visible in an increased 4f state occupation number and in the stronger dichroism at the M$_{4,5}$ edges for the highest Si content in the Ce$_{1-X}$Si$_X$ sublayer.

It is also reflected in the L$_{2,3}$-XMCD spectra. While they show a double-peak structure known for the pure Fe/Ce multilayers with α-phase-like Ce, they are distinctly modified at low temperature: for a Si content of x=0.4 the two peaks have the same amplitude, and for x=0.65 the spectral shape is completely different. This modification is attributed to the increased magnetic polarization on the 4f states and thus increased 4f-5d exchange interaction. In fact, the L$_2$/L$_3$ ratio is near -2 for the lowest Si concentration x=0.1 at 10K as expected for a non-interacting Ce-5d shell; but it changes sign and increases considerably for x=0.65. Comparison with the results obtained for the Fe/CeH$_X$ multilayers (chapter 3.8.2) suggests to attribute this to a 4f-5d exchange interaction. Unfortunately a theory of the XMCD spectra at the L edges of the RE does not exist. Therefore the experimental data were tentatively compared with the α-β model. The

phenomenological model admits to parameterize the spectra and describe the trends in the variation with Si concentration and temperature. It should be noted that the behavior of the $Ce_{1-x}Si_x$ alloys in the multilayers with Fe is very different from bulk compounds $CeSi_{2-\delta}$ which order magnetically for $\delta>0.15$ but are nonmagnetic for $\delta=0$. In these compounds the Ce-4f occupancy is close to one and the Kondo effect plays an important role.

1   F. Klose, O. Schulte, F. Rose, W. Felsch, S. Pizzini, C. Giorgetti, F. Baudelet, E. Dartyge, G. Krill, and A. Fontaine, Phys. Rev. B **50**, 6174-6183 (1994).

2   D. Malterre, G. Krill, J. Durand, and G. Machal, Phys. Rev. B **34**, 2176 (1986)

3   A. Delobbe, Thèse de Université Paris-Sud, Orsay (1999)

4   W. H. Lee, R.N. Shelton, S-K. Dhar and K.A. Gschneider, Jr., Phys. Rev. B **35**, 8523 (1987)

5   P. Hill et al., J. Phys. Cond. Matt. **4**, 5015 (1992)

6   T. Hihara, K. Sumiyama, H. Yamauchi, Y. Homma, T. Suzuki, K. Suzuki, J. Phys.: Condens. Matter **5**, 8425 (1993)

7   J. Thiele, F. Klose, A. Schurian, O. Schulte, W. Felsch, and O. Bremert, J. Magn. Magn. Mater. **119**, 141 (1993)

8   P. Schaaf, unpublished results

9   Ph. Bauer, F. Klose, O. Schulte, and W. Felsch, J. Magn. Magn. Mater. **138**, 163-172 (1994).

10 J. Hesse and A. Rübartsch, J. Phys. E 7, 526 (1974); G. LeCaer and J.M. Dubois, *ibid*. 12, 1083 (1979)

11 C. T. Chen, Y. U. Idzerda, H.-J. Lin, N. V. Smith, G. Meigs, E. Chaban, G. H. Ho, E. Pellegrin, and F. Sette, Phys. Rev. Lett. **75**, 152 (1994)

12 O. Gunnarson and K. Schönhammer, in *Handbook on the Physics and Chemistry of the Rare Earths*, editor K. A. Gschneider, Jr., L. Eyring and S. Hüfner (North-Holland, Amsterdam 1987), Volume 10, p. 103

13 J. Röhler in *Handbook of Chemistry of Rare-Earths*, ed. L. Erving and S. Hüfner (North Holland, Amsterdam 1991), Volume 10, Chap.71

14 T. Jo and A. Kotani, Solid State Commun. **54**, 451 (1985); A. Kotani, J. Phys (Paris), Colloq. **48**, c9-869 (1987); A. Kotani and J. C. Parlebas, Adv. Phys. **37**, 37 (1998)

15 D. Malterre, Phys. Rev. B **43**, 1391 (1991)

16 M. Arend, M. Finazzi, O. Schulte, A.-M. Dias, F. Baudelet, Ch. Giorgetti, M. Münzenberg, P. Schaaf, E. Dartyge, J.P. Kappler, G. Krill, and W. Felsch, Phys. Rev. B **57**, 2174 (1998)

17 M. S. S. Brooks, O. Eriksson, and B. Johansson, J. Phys.: Condens. Matter 1, 5861 (1989); Thole et al. Phys. Rev. B **32**, 5107 (1985)

18 J. C. Fuggle, F. U. Hillebrecht, J.-M. Esteva, R. Karnatak, O. Gunnarson, and K. Schönhammer, Phys. Rev. B **27**, 4637 (1983)

19 M. Arend, W. Felsch, G. Krill, A. Delobbe, F. Baudelet, and E. Dartyge, J.-P. Kappler, M. Finazzi and A. San Miguel-Fuster, S. Pizzini and A. Fontaine Phys. Rev. B **59**, 3707 (1999)

5. Element-specific magnetization reversal in Fe/Ce multilayers

5.1 Introduction

Soft magnetic materials are very interesting from a technological point of view, e. g. for the construction of extremely sensitive magnetic field sensors. The sensing layer for measuring the magnetic field of the earth, for example, has to switch in the field of ~0.5 G. Nanocrystalline soft magnetic compounds are well known since 40 years. The description of the magnetic properties can be related to the microstructure (grain size) very well [1]. The origin of the softness is related to a strong reduction of the magnetic crystalline anisotropy. The anisotropy on the atomic scale is randomly averaged out. Thus there is no net anisotropy effect on the magnetization process. The characteristic length scale for magnetic materials is the exchange length L_{ex}. It depends on the exchange stiffness A_{ex}, the energy required for the rotation of two adjacent spins, and the crystalline magnetic anisotropy energy density K_1 for rotating the spins from a preferred easy-axis direction in the crystallite:

$$L_{ex} = \sqrt{\frac{A_{ex}}{K_1}} \qquad\qquad 5.1$$

Typical values for bcc-Fe are $A_{ex} = 2.8 \cdot 10^{-6}\,\text{erg/cm}$ and $K_1 = 3 \cdot 10^3\,\text{erg/cm}^3$ resulting in an exchange length of $L_{ex} \sim 100\,\text{Å}$ [2,3].

The role of different energy contributions is evident in equation 5.2, where the total energy is calculated for the case of a simple one dimensional spin chain with N spins.

$$E = \sum_{i=1}^{N} \left(-\frac{A_{ex(i,i-1)}}{d^2} \cos(\Theta_i - \Theta_{i-1}) - K_1 \cos^2(\Theta_i - \Theta_{0,i}) - H M_i \cos(\Theta_i) \right) \qquad 5.2$$

d is the distance between two spins coupled with an exchange constant $A_{ex\,(i,i-1)}$, Θ_i is the angle of the spin orientation with respect to the field axis, H is the applied field (Zeeman term), and M_i is the magnetic moment per spin i and K_1 an uniaxial magnetic anisotropy constant. $\Theta_{0,i}$ denotes the angle of the magneto-crystalline local easy axis. The expression has to be minimized in respect to Θ_i and reveals the significant energies that contribute to the magnetization reversal process, i.e. the interplay between exchange stiffness preferring a parallel orientation of adjacent spins and the magnetic anisotropy term preferring an orientation in the direction of the local magnetic easy axis.

If the exchange length is longer than the crystallite size D, which is the case in nanocrystalline materials, the crystalline anisotropy term has to be replaced by a random crystalline anisotropy <K> [1]. <K> is calculated from random walk arguments: the orientation of the magnetization does not follow the local variation of the magnetic anisotropy in the nanocrystalline systems and therefore the crystalline magnetic anisotropy is averaged out. The reduction of the anisotropy calculated by Herzer [1] scales with the reciprocal squareroot of the number of nanocrystalline grains N inside the volume L_{ex}^3

$$\langle K \rangle = \frac{K_1}{\sqrt{N}} \qquad 5.3$$

In a multilayer system, soft magnetic behavior is maintained especially below a critical thickness. This is observed experimentally but its origin is not clear.
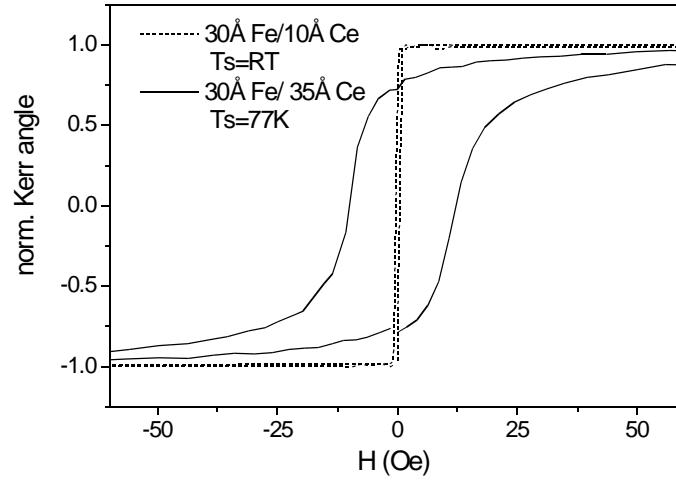
Figure 5.1. Soft magnetic [30Å Fe/10Å Ce]x100 multilayer sample with saturation fields below 1 Oe. The [30Å Fe/ 35Å Ce]x61 sample with a thicker Ce layer thickness grown at lower temperatures is magnetically much harder.

Figure 5.1 shows an example for a soft and hard magnetic hysteresis curve measured in the case of the Ce/Fe multilayers. The soft magnetic sample with saturation field of 1 Oe is prepared at room temperature and has a smaller Ce sublayer thickness than the magnetically harder one.

For multilayers, the magnetic properties are strongly related to the structural properties of the interface, i.e. diffusion or structural roughness. These parameters depend on the substrate temperature, growth technique and growth rates. A critical factor in multilayer structures is the misfit of the lattice constants depending on the sublayer components chosen. It is well known that in TM/RE multilayers the misfit between the lattice constants can be quite large (~30%) and results in an amorphous growth of the sublayers up to a thickness of ~20 Å.

In this chapter measurements of the XMCD at the Ce-L_2 edge in Fe/Ce multilayers which probe the role of this sublayer material in the magnetization reversal process are compared with the magneto-optic Kerr effect data representing the Fe magnetization. The Fe-layer thickness is kept fixed at 30Å, whereas that of the Ce

layers is varied between 20 and 45 Å. Two samples [30Å Fe/ 30Å CeH$_{2-\delta}$]x67 and [30Å Fe/ 15ÅLa/ 10ÅCe/ 15Å La]x57 are studied as a reference.

5.2 Structural properties

The samples are prepared as described in chapter 1.1 with total thickness of the multilayer stack ~4000 Å. The high-angle diffraction data reveal the crystallite size and structure in growth direction (figure 5.2) for the different multilayer structures prepared. The hydrogenated Fe/CeH$_{2-\delta}$ multilayer samples show a good crystallinity and a textured growth of both constituents, as discussed more in detail in chapter 3.4. The high-angle diffraction spectra of the Fe/Ce multilayers reveal weak peaks of the bcc-Fe crystallites in the 30Å-thick Fe layers. The thickness is just above the critical thickness value of 25 Å for crystalline growth.
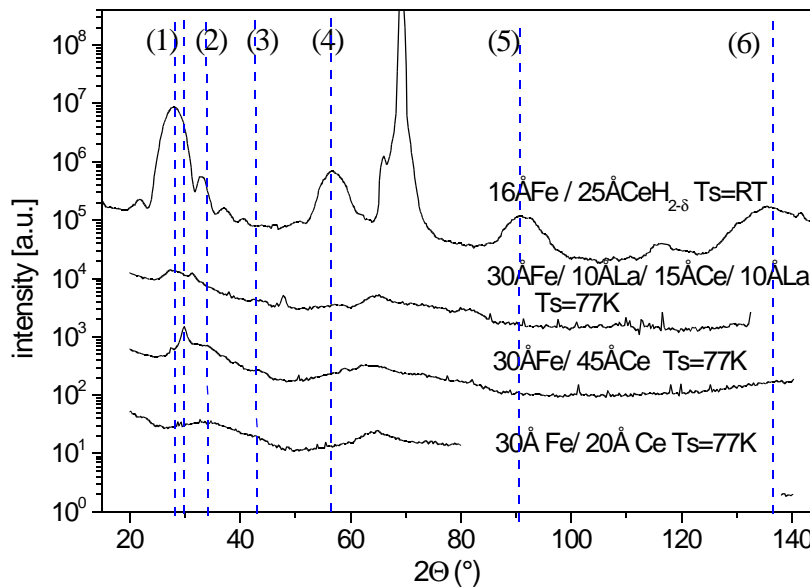

Figure 5.2. High-angle X-ray diffraction data for the different Fe/RE multilayer types. The positions marked are: (1) CeH$_{2-\delta}$(111), in between γ-Ce(111), (2) α-Ce(111), (3) α-Fe(110), (4) and (5) CeH$_{2-\delta}$(222) and (333) respectively, (6) α-Fe(222). The lower three spectra are measured with an offset of Θ=4°. All samples are grown on Si(100) substrate.
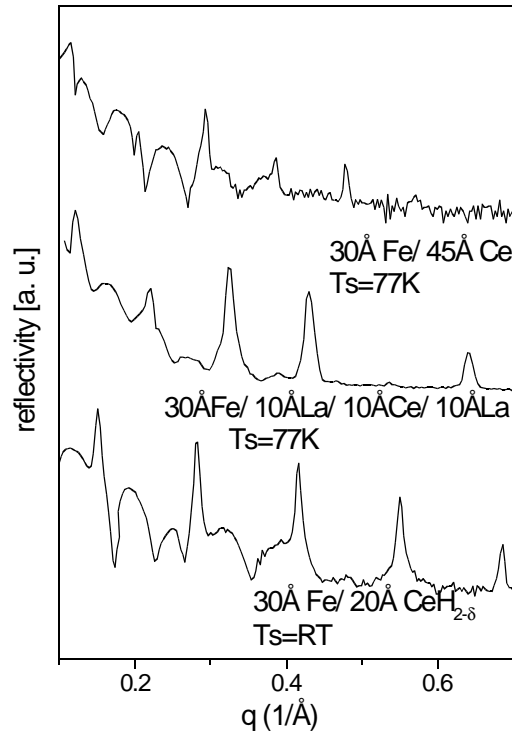
Figure 5.3. Small-angle X-ray diffraction profiles for the different Fe/RE multilayer structures: the Fe/Ce system, the Fe/La/Ce/La system and the hydrogenated $Fe/CeH_{2-\delta}$ system.

The crystalline growth is clearly stated by the magnetic measurements: the Curie temperature is above 300 K. In contrast, the La and Ce layers in Fe/La/Ce/Ce and the 20 and 35 Å thick Ce layers in Fe/Ce grow in an amorphous structure, in the case of Ce with α-phase-like short-range order. In the Fe/Ce multilayer system with the largest Ce-layer thickness of $t_{Ce}= 45$Å, the signature of the crystalline γ-phase of Ce appears. The peak is superposed to the α-like phase and indicates the transition to a laminated α/γ-Ce-like two-phase structure, with the α-like-phase at the Fe/Ce interfaces and the γ-like phase in the center. These results are in agreement with the conclusions drawn from previous studies on these multilayer systems [4,5,6].

Figure 5.3 shows the small-angle X-ray reflectometry of the multilayer structures. From these measurements the periodicity (modulation of the chemical periods) and the interface roughness are extracted by the fitting procedure described in chapter 1.2. For the Fe/CeH$_{2-\delta}$ multilayer and the Fe/La/Ce/La multilayer with La at the Fe interface, the small angle data show multiple Bragg peaks. The interface roughness (rms) amounts 2.0-2.5 Å. For the Fe/Ce multilayer grown at 77K, the intensity of the Bragg peaks decreases much faster: the roughness (rms) amounts 4-5Å.

5.3 Magnetic interfaces: [57] Fe Mössbauer spectroscopy

Substantial information on the magnetic interfaces in the multilayers results from [57]Fe Mössbauer spectroscopy of the Fe/Ce, Fe/CeH$_{2-\delta}$ [7,5] and Fe/La/Ce/La multi-layers [6] similar as in the Fe/Ce$_{1-x}$Si$_x$ multilayers discussed in chapter 4.2. The analysis reveals the presence of an interface component with a reduced magnetic hyperfine field in addition to the normal six-line part resulting from the core of the bcc-Fe layers. This interface component reflects the perturbation of the electronic structure of Fe near the interface. As reported in [7] and in the same way as in chapter 4.2 the spectra were decomposed into a sextet representing the bcc-Fe part in the core of the Fe layers, and a probability distribution of magnetic hyperfine fields attributed to different interface regions, adapted to the layered structure of the samples. The [57]Fe Mössbauer spectra and the hyperfine field distribution p(B$_{hf}$) related to the interface are shown in figure 5.4.

The Fe environment is affected on a length scale (in the growth direction) of ~9Å per interface in the samples [30Å Fe/ 30Å Ce]x67 and [30ÅFe/ 10ÅLa/ 10ÅCe/ 10ÅLa]x68, and of ~4 Å per interface in the sample [16Å Fe/16Å CeH$_{2-\delta}$]x150. This exceeds the extension of the structural roughness in the case the Fe/Ce and
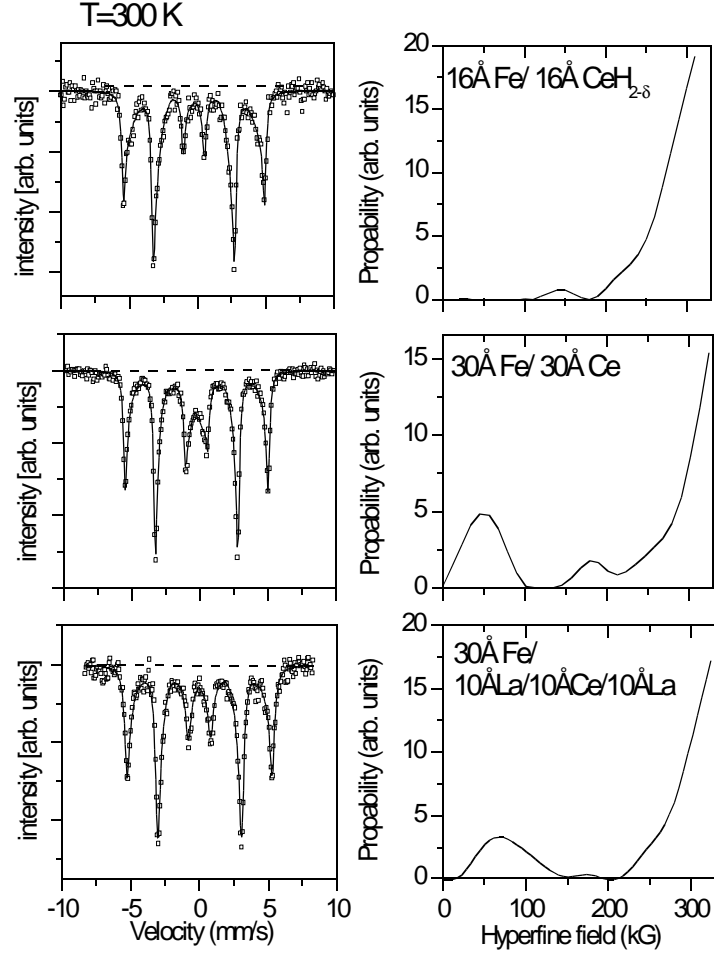
Figure 5.4. Left: ^{57}Fe Mössbauer spectra of the multilayer systems Fe/CeH$_{2-\delta}$ (top),   Fe/Ce (middle), Fe/La/Ce/La (bottom) measured at room temperature. Right: corresponding B$_{hf}$ distribution [from 7,6].

Fe/La/Ce/La multilayers. A special feature is observed in the Mössbauer spectrum of the Fe/Ce system: the hyperfine-field distribution attributed to the interface, $p(B_{hf})$ presents a pronounced maximum near 50 kG. The contribution of this signature to the total intensity of the spectrum corresponds to a Fe-layer thickness of 2.5 Å per interface, i.e. of nominally 1 atomic layer. This value is compatible with the structural roughness derived from the X-ray diffraction data. The low-

field $p(B_{hf})$ structure represents the Fe atoms in the intermixed zone at the direct Fe/Ce interface [7]; they form a kind of weakly magnetic 'interface alloy' as compared to Fe in the center of the sublayers (the magnetic hyperfine field of Fe is reduced by a factor of seven). In view of the XMCD data it can be concluded [6] that this 'interface alloy' is stabilized by the hybridization between the 3d states of Fe and the delocalized 4f states of Ce. It presents a well-defined mean local environment. Note that the amorphous compounds $CeFe_2$ and Ce_2Fe_{17} have Curie temperatures below room temperature ($T_C(CeFe_2)$=220K).

The magnetic perturbation at the interface can be changed significantly by the insertion of a La layer between the Fe and Ce: the maximum in the distribution $p(B_{hf})$ is reduced and shifted to higher B_{hf} values. This agrees well with the smaller interface roughness observed in the X-ray reflectometry data and with the absence of the Ce-4f Fe-3d hybridization at the interface [6]. The feature at low B_{hf} values vanishes completely in for the $Fe/CeH_{2-\delta}$ multilayers (graph on the top in figure 5.3). In this case only 4Å of Fe at each interface show a reduction of the hyperfine field which agrees with the smoother interfaces and the well-textured growth. The average hyperfine field is typically ~260 kG in Fe/Ce, 321 kG in $Fe/CeH_{2-\delta}$, 300 kG in Fe/La and ~285 kG Fe/La/Ce/La in the multilayer.

In a first approach the magnetic hyperfine field is proportional to the spin S of the Fe atom and thus to the average spontaneous magnetization of the Fe environment. This interpretation is problematic because the Fermi conversion factor can change at the interfaces if there is a strong 4s-orbital hybridization of the conduction electrons. The result of this hybridization effect is a reduction of the 2s, 1s polarization of the Fe orbitals and therefore a reduced B_{hf} of the Fe core [8]. Here, in the Fe/Ce multilayers the reduction of the B_{hf} cannot result from this effect: the reduced average value is connected with a reduction of the macroscopic
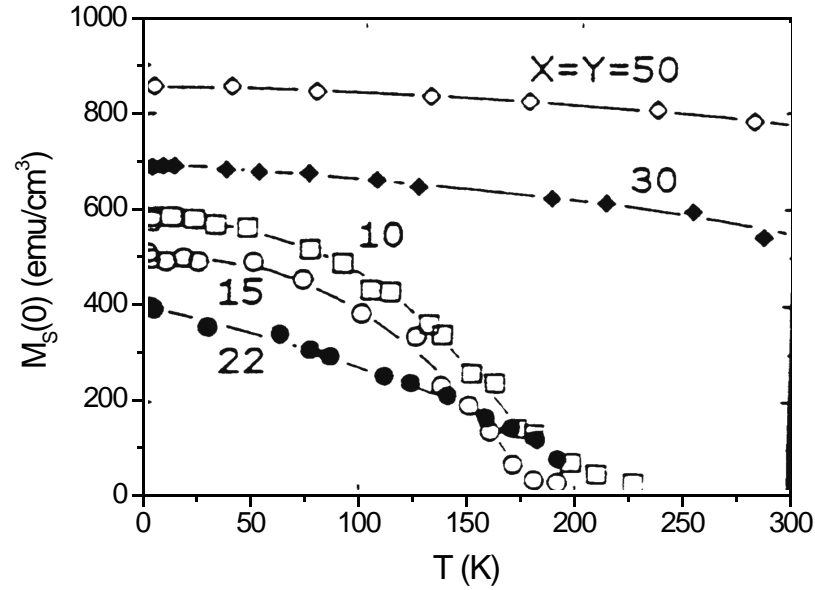
Figure 5.5. Temperature dependent measurements of the spontaneous magnetization for different XÅ Fe/ YÅ Ce multilayer samples at the amorphous-to-crystalline transition of the Fe layers (taken from [5]).

magnetization (figure 5.5, [5]). For this reason it can be assumed that this small value of B_{hf} is essentially related to a small value of the spontaneous magnetization.

5.4 Experimental details - element selective hysteresis measurements

The element selectivity intrinsic to X-ray absorption (XA) spectroscopy is used to probe the magnetic field dependence of the Ce-5d polarization in the multilayers which is induced by Fe. Therefore the L_2 edge (6164 eV) is investigated, which involves the dipole-allowed transition from the $2p_{1/2}$ core level to the $5d$ valence states (chapter 2.3). The XMCD spectra at the Ce-L_2 edges are measured at the energy dispersive beamline ID 24 at the European Synchrotron Radiation Facility (ESRF) as described in chapter 1.4.

The polarization of the Ce-5d electrons is induced by the Fe, although the α-Ce interface is near a ferromagnetic instability as it is outlined in [6]. The mechanism is explained by the model of Brooks [9] discussed in chapter 2.2 by a hybridization of the Fe-3d and Ce-5d band at the direct interface, resulting in an antiparallel orientation of the Fe-3d and Ce-5d moment. For the XMCD measurements the field is applied in grazing incidence (30° from the layer plane), parallel to the incoming beam.

In principle, it is possible to measure the magnetic polarization of Fe at the $L_{2,3}$ or K edge with the same experimental setup. For the energy range available at ID 24 solely the Fe-K edge is accessible: the dichroic signal of the transition is only 0.1% It is a transition into the unoccupied Fe-p states with minor magnetic polarization. Therefore the magnetic polarization of the Fe-3d electrons is investigated by the magneto-optical Kerr effect described in [10]. The Kerr-rotation angle is determined by the intra-band transitions of the 3d electrons excited by the incoming polarized light with a wavelength of 632.8 nm. At this wavelength the method has a depth sensitivity of ~300 Å. It is important to discuss the determination of the field values for both experimental setups carefully to warrant a genuine comparison of the XMCD and Kerr-effect hysteresis curves.

5.4.1 Determination of the magnetic field

The measurement of magnetic fields is difficult if the field is in the Oersted range. For example, if an electromagnet is used fields remain though the applied current is zero because of the residual fields of the Fe core. Another uncertainty appears if the field values are measured with different sensors for both experiments. For this reason the identical setup is used for the MOKE measurements at University of Göttingen and brought to the beamline ID24 at the ESRF where the XMCD measurements are carried out: a two-coil setup in Helmholtz geometry with a large

area of homogeneous field (40x30mm^2). In this setup it is possible control the applied field by measuring the current. The accuracy is better than 2 mA (~0.1 Oe). The power supplies (Heinzinger, Delta Electronics) have an excellent accuracy in the low current region (<100 mA). The absolute calibration of the field value is done with a hall resistor (acurracy: 5%). The calibration value is H=50 Oe/A. In the experimental setup stray fields that give an offset on the field axis, are avoided.

For the XMCD measurements the magnetic field is applied at 30° referred to the plane as pointed out above. But all samples have a strong in plane anisotropy (at 300 K) due to the shape anisotropy. As the out-of-plane component of the applied field is small compared to the demagnetization field (~20 kOe, multiplied with cos (60°) = 0.5 for the geometry used) the out-of-plane magnetization component of the samples can be neglected. And finally the measurements prove that there is no systematic deviation comparing the different hysteresis curves (MOKE and XMCD). For the XMCD measurements the field component in the layer plane, H_{eff}=cos(30) H, is plotted on the field axis.

5.5 Experimental results

Figure 5.6 displays a representative set of Ce-L$_2$ XMCD spectra out of a hysteresis cycle for the multilayer 30Å Fe/ 20Å Ce. The spectra are measured at different magnetic fields, which pass from negative values (top) through zero to positive values (bottom). For the acquisition of one spectrum the field value is fixed and the helicity of the incoming beam is flipped by rotating the quarter-wave plate (chapter 1.4).
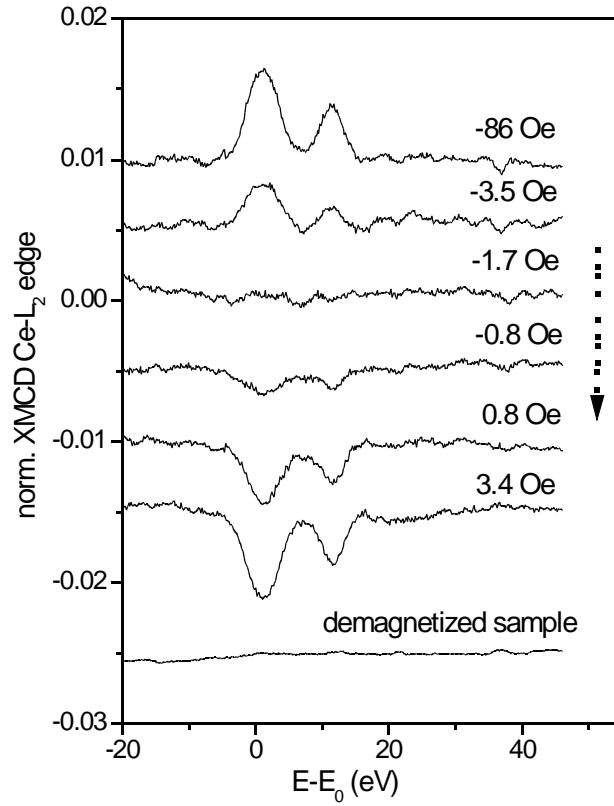
Figure 5.6. Set of XMCD spectra at the Ce-L$_2$ edge in the multilayer 30Å Fe/ 20Å Ce for different field values during a hysteresis cycle. The applied magnetic fields increase from negative to positive values (dotted arrow).

As expected for the Fe/Ce multilayers [4], the XMCD signals consist of two contributions as in the case of the the isotropic absorption spectra, with the same splitting (~10 eV). This is the signature of an α-like 4f configuration in Ce. The change of sign indicates that a reversal of the net 5d-electron polarization of Ce occurs as soon as the applied field turns from positive to negative values. From the definition of the XMCD signal it can be concluded that a negative sign at the L$_2$ edge for a positive applied magnetic field indicates an antiparallel orientation of the Ce-5d and Fe-3d ordered magnetic moment (chapter 2.2, 2.4). In figure 5.7 the magneto-optical Kerr effect data of a representative Fe/Ce multilayer and two
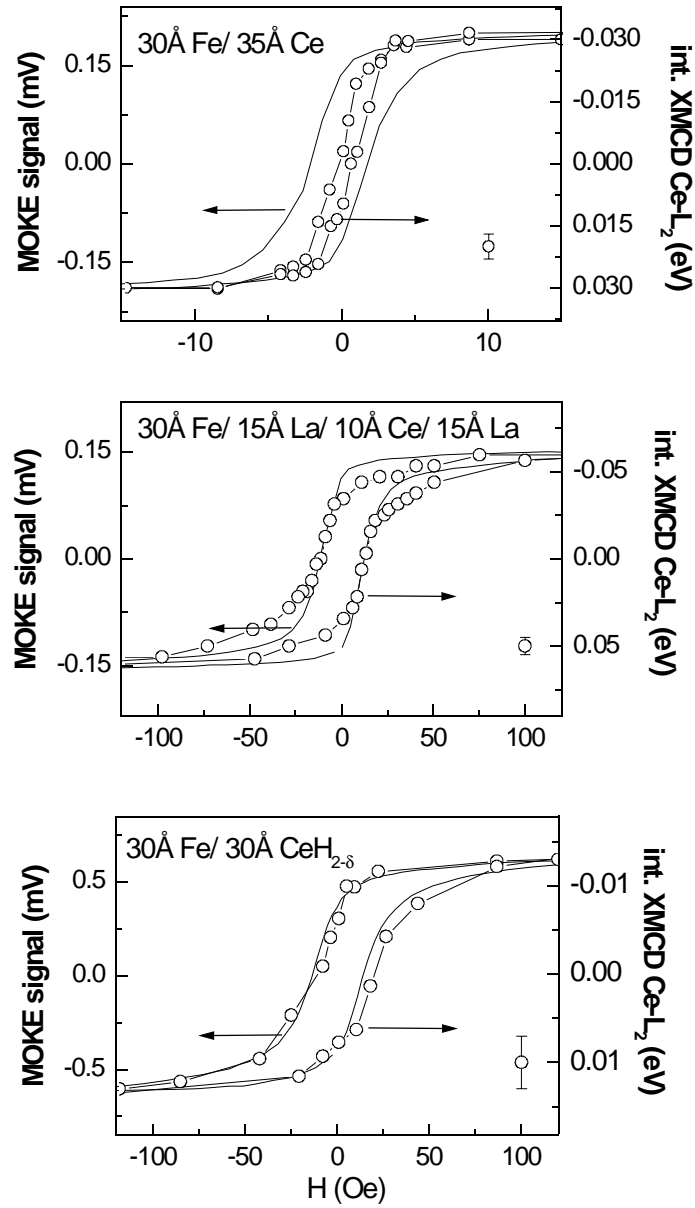
Figure 5.7. Hysteresis curves measured with the magneto-optical Kerr effect (continuous curves) and the integrated XMCD at the Ce-L$_2$ edge (circles) for the multilayer samples 30Å Fe/ 35Å Ce (top) 30Å Fe/ 15Å La/ 10Å Ce/ 15Å La (middle) and 30Å Fe/ 30Å CeH$_{2-\delta}$ (bottom). Note the different magnetic-field scale for the samples containing hydrogen and lanthanum. The XMCD loops are mirrored at the vertical axis.

reference samples is compared to the integrated XMCD which is a measure of the Ce-5d magnetic polarization. The Kerr rotation essentially represents the Fe-layer magnetization within a depth sensitivity of 300 Å. The scale on the field axis is changed by a factor of 8 in the lower graphs. For a direct comparison of the hysteresis loops, the axis of the integrated Ce-L_2-XCMD signal is mirrored at the origin. For all samples the Fe thickness is fixed.

The Fe/Ce multilayers are magnetically very soft and reach magnetic saturation in a small field. This is at variance with the usually observed hysteresis of a single Fe layer with a comparable thickness. The reference samples, the La intercalated as well as the hydrogenated multilayer, are considerably magnetically harder. While the MOKE-derived absolute coercivity ranges between 1 and 3 Oe for Fe/Ce, it amounts to 13 Oe for Fe/La/Ce/La and 15 Oe for Fe/CeH$_{2-\delta}$.

The hysteresis of the integrated Ce-L_2 signal should follow the Fe-layer magnetization since the Ce-5d moment is induced by Fe. This behavior is observed for the Fe/CeH$_{2-\delta}$. But in the Fe/Ce multilayers the polarization of the 5d-Ce electrons reveals a smaller hysteresis than expected from the Fe-layer magnetization. Somewhat more complicated is the case of the Fe/La/Ce/La-multilayer: the Ce-5d magnetization is transferred via the La polarization and not by the direct interface polarization. The difference is not as dramatic as in the case of the Fe/Ce system. Starting at saturation, the Ce magnetization decreases faster than the Fe magnetization. At the coercive fields the magnetization curves cross and with increasing the reversed field the Fe magnetization increases first before the Ce polarization follows.

The characteristic values of the hysteresis curves are depicted in figure 5.8. The ratios of the coercive fields, H_C^{XMCD}/H_C^{MOKE}, and squarenesses, S^{XMCD}/S^{MOKE}, are plotted for the different multilayer samples. For the three Fe/Ce multilayers the
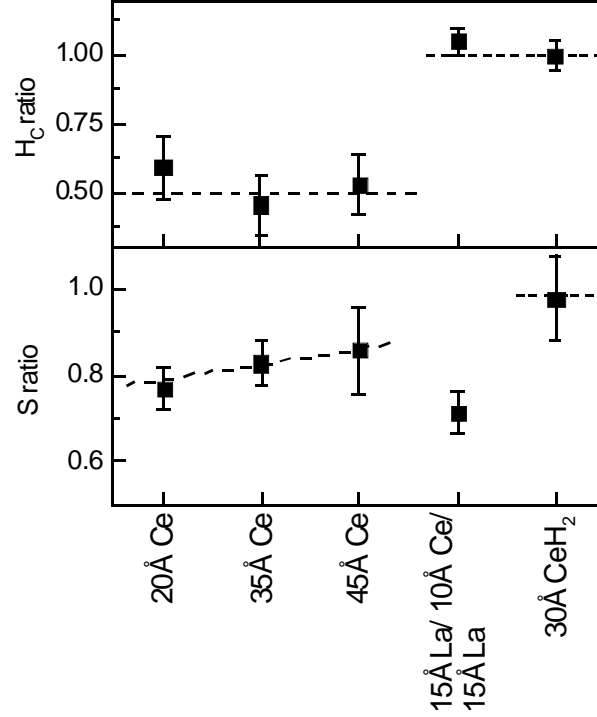
Figure 5.8. Characteristic values of the hysteresis in a direct comparison: the ratios of the coercive fields H_c^{MOKE} /H_c^{XMCD} as well as the ratios of the squareness S^{MOKE}/S^{XMCD} are shown for the studied samples.

coercivity of the Ce-5d hysteresis, H_c^{XMCD}, is reduced by 50% with respect to the value of the total hysteresis, H_c^{MOKE}, for all Ce-layer thicknesses t_{Ce}. The coercive fields are considerably reduced for all Ce thicknesses investigated. The multilayer systems show different squareness ratios: ~0.8 for Fe/Ce compared to 0.7 for Fe/La/Ce/La and about one for the Fe/CeH$_{2-\delta}$ multilayer ($S=M_R/M_S$). The low squareness ratios of the La intercalated multilayer is related to the observation that the Ce-5d electrons are more difficult to magnetize than the Fe-3d electrons (figure 5.7).

5.6 Discussion

The following significant results are obtained by the element-selective hysteresis experiments: the Fe/Ce multilayers are the magnetically very soft compared to the two reference samples and an unequal reversal of the Ce-L_2 XMCD and MOKE signal occurs in the external magnetic field.

The magnetic softness of the Fe/Ce multilayers may be related to the amorphous structure of Ce. In fact, previous investigations on this system indicate that the Fe-3d moments are rigidly coupled to the Ce-5d moments at the interface by 3d-5d hybridization [6]. Thus the reversal of the Fe-layer magnetization depends on the micromagnetic structure of the Ce layers. Due to their amorphous nature the Ce layers are very soft magnetically since the structural correlation length (on the order of the interatomic distance) is small compared to the exchange correlation length underlying the ferrimagnetic spin configuration. Then, the effective magnetic anisotropy is small, even more in view of the delocalized nature of the 4f states of the α-like Ce configuration in these multilayers. As a consequence, the Fe-layer magnetization can easily rotate in a reversed magnetic field, or nucleated rotated magnetic domains can easily expand. By inserting a La spacer between Ce and Fe, or by separating the Fe sublayers by a crystalline $CeH_{2-\delta}$ layer in which the 4f states are localized, this effect described vanishes. In both cases, the coercivity is considerably increased.

It is more difficult to understand why XMCD and MOKE hysteresis cycles in the Fe/Ce multilayers differ from each other. This behavior is discussed in relation to two possible mechanisms.

The smaller coercivity of the XMCD loop related to the Ce-5d magnetic polarization compared to the Fe-3d determined MOKE loop may be directly related to the special magnetic structure of the Fe/Ce interfaces. For the Fe/Ce system, the small magnetic hyperfine field B_{hf} ~50 kG in the intermixed region immediately at the interface, signals a considerably reduced exchange stiffness A_{ex} compared to the interior of the Fe layers. Taking the relation

$$A_{ex} \propto \frac{Tc\,M_S{}^2}{d} \qquad\qquad 5.6$$

(T_C: Curie temperature, M_S: saturation magnetization) and B_{hf} as a qualitative measure of M_S, M_S~B_{hf}, one can calculate a profile of A_{ex} shown in figure 5.9. It covers the distance from the core of the Fe layers to the interface with Ce and is
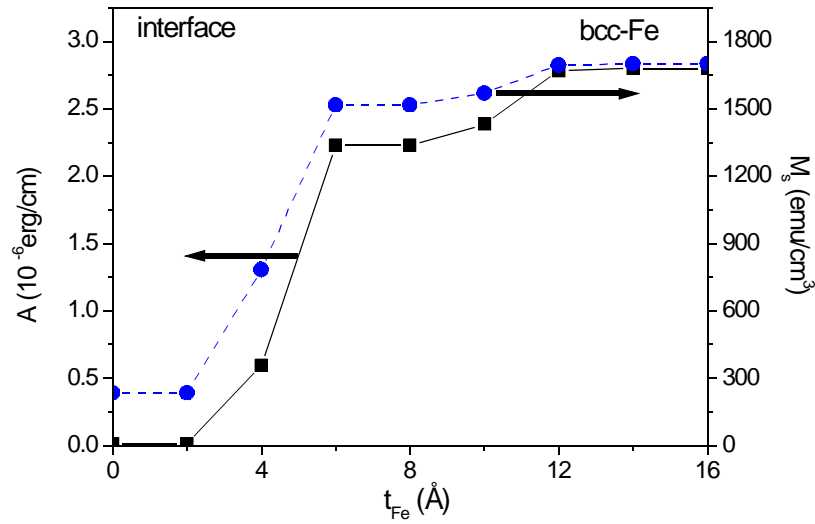

Figure 5.9. Profile of the exchange stiffness A_{ex} and the saturation magnetization M_S governed from the Mössbauer data as described in the text. The variation across the Fe sublayer is shown from the interface region to the central bcc-Fe part.

based on the values $A_{ex}= 2.8 \cdot 10^{-6}$ erg/cm, $M_S=1700$ emu/cm^3, and $T_C=1044$ K for bcc-Fe. The variation of M_S uses the variation of B_{hf} across the Fe layers determined by ^{57}Fe Mössbauer spectroscopy [7]. Note that one gets a two orders of magnitude reduction of A_{ex} at the interface compared to the central part of the Fe layer: $A_{ex,interf}$ /$A_{ex,bcc}$=0.007. This estimate disregards the equally observed reduction of T_C (figure 5.5). A similar approach is used by Suzuki et. al. [11] in a nanocrystalline two phase model.

The value of the magnetic anisotropy is very difficult to estimate. Since the intermixed Fe-Ce region is expected to adapt the highly disordered amorphous structure of the Ce layer, it exhibits a small magnetocrystalline anisotropy. On the other hand, due to the misfit of the lattice parameters at the interface magnetostriction may contribute to the magnetic anisotropy.

The most important result is the reduction of A_{ex} at the interface. Since the bulk value of B_{hf} is recovered ~9 Å away from the interface, coupling of the interfacial Fe moments to the bulk magnetization of the film must be rather disturbed. Thus the magnetization of the interfacial Fe atoms may reverse in a lower field compared to the core of the Fe layer; due to the rigid coupling to the Ce this
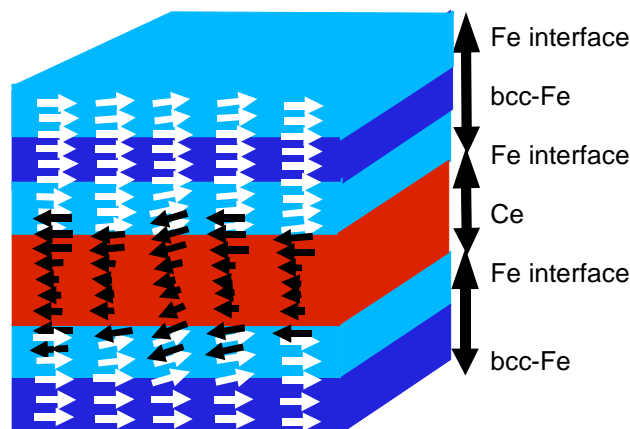

Figure 5.10. A simple model visualizing the magnetization-reversal process nucleated in the interface region.

would appear as a reduced coercivity in the Ce-5d XMCD hysteresis compared to the MOKE loop. For an illustration, a simple picture is drawn in figure 5.10.

The measured 5d magnetic moments of Ce in the multilayers resulting from the XMCD experiment present an average over the Ce sublayer. In a model of coherent magnetization rotation, the difference of the XMCD and MOKE signal at a given applied field can be converted into a twist angle Θ: this yields to (since the normalized signals $M_{Ce\text{-}5d}/M_{Ce\text{-}5d,max}$ and $M_{Fe\text{-}3d}/M_{Fe\text{-}3d,max}$ are the projections in the direction of the applied field)

$$\Theta(\langle \boldsymbol{m}_{S,Fe-3d}\rangle,-\langle \boldsymbol{m}_{S,Ce-5d}\rangle)=\arccos\left(\frac{M_{Ce-5d}}{M_{Ce-5d,max}}\right)-\arccos\left(\frac{M_{Fe-3d}}{M_{Fe-3d,max}}\right) \qquad 5.5$$

The negative sign in equation 5.5 considers the antiparallel alignment between the average Ce $\langle \boldsymbol{m}_{S,Ce\text{-}5d}\rangle$ and the average Fe magnetization $\langle \boldsymbol{m}_{Fe,S\text{-}3d}\rangle$. The resulting angle Θ is plotted in figure 5.11 for the 30Å Fe/ 35Å Ce mulitlayer. At a field of
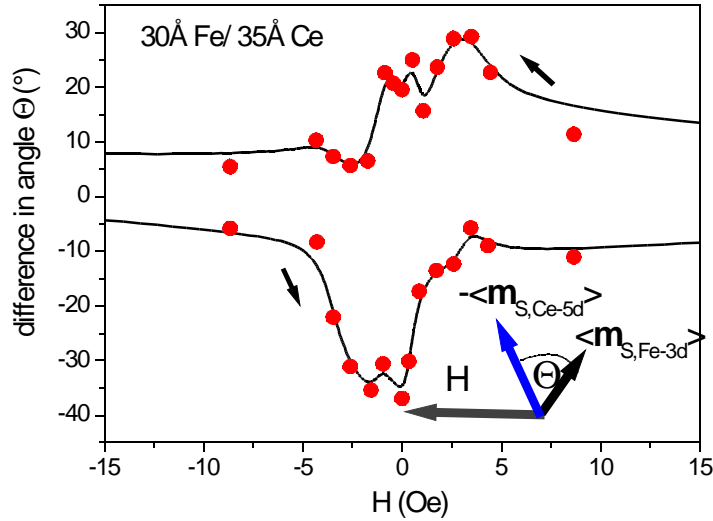

Figure 5.11. Difference in angle between an average Ce magnetization direction and an average Fe direction for the 30Å Fe/ 35Å Ce multilayer. The twisting angle is calculated in a model of coherent rotation using equation 5.5. The line is a guide to the eyes.

15 Oe the difference in angle is about 5°. As the field is decreased, the XMCD signal decreases more rapidly than the MOKE signal, which indicates that the net Ce-5d and Fe magnetization become increasingly non-collinear with a maximum canting angle of Θ~30° at 2 Oe. Reversing the fields leads to the same behavior, but the maximum value of Θ becomes slightly larger (~40%) because of a small shift of the Ce hysteresis on the field axis (0.2 Oe).

The different MOKE and Ce-XMCD hysteresis of the Fe/Ce multilayers may also be related to the complex non-collinear spin structure in the Ce layers [12].
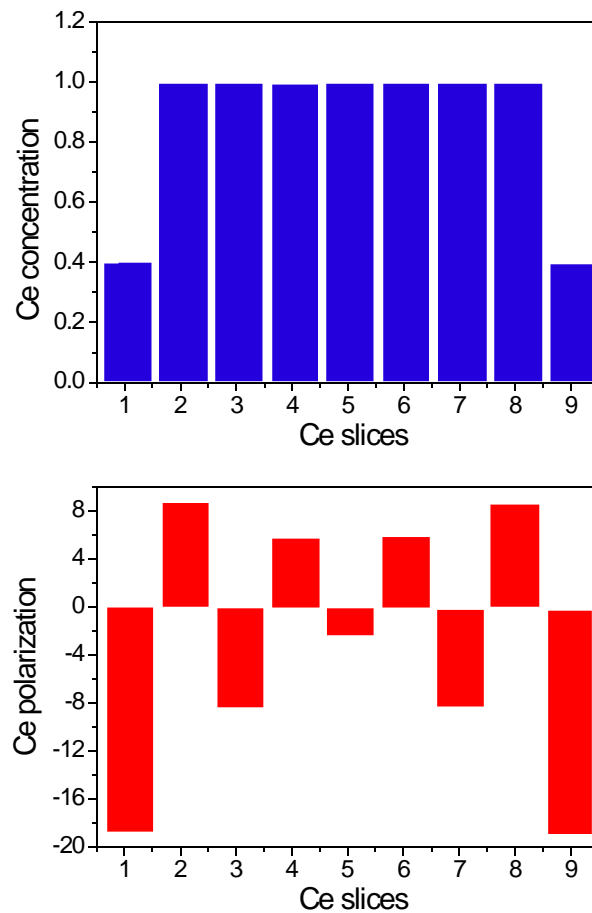
Figure 5.12. Profiles across the Ce sublayer in the 30Å Fe/ 20Å Ce multilayer. Top: Ce atomic concentration. Bottom: Ce 5d induced polarization resulting from X-ray resonant magnetic scattering experiments at the Ce-L_2 edge [12].

A twisted magnetic structure in the the multilayers is compatible with the oscillating, non-uniform magnetization profiles of the 5d states in Ce suggested by the results of X-ray Resonant Magnetic Scattering (XRMS) shown in figure 5.12. The oscillation profile is found in Fe/Ce and Fe/La/Ce/La multilayers as well, with a period equal to two times the (111) interplanar distance of α-Ce and an amplitude slowly decreasing towards the center of the Ce layer [12,13]. In each case, the net magnetic 5d-electron polarization and its overall extension recovers the results derived from XMCD [6].

5.7 Summary

The element selectivity of XMCD and its sensitivity to detect small magnetic moments is used to explore the process of magnetization reversal in Fe/Ce multilayers. Comparative experiments were performed on multilayer samples Fe/La/Ce/La and Fe/CeH$_{2-\delta}$. In these systems, Fe induces magnetic order on the 5d states of Ce. The Fe/Ce system is very soft magnetically, with saturation fields of a few Oersteds. This can be related to the amorphous structure of Ce. One finds that in this multilayer system the coercivity of the Ce-5d electron hysteresis is about 50% smaller than measured by MOKE. Two explanations for the different magnetic response of the Ce-5d and Fe magnetic moments to an external magnetic field have been considered: the differences in the hysteresis curves reflect either the soft magnetic interface or the complex non-collinear magnetic structure in the Ce layers. The latter property may also be a possible explanation for the behavior of the Fe/La/Ce/La sample. The different behavior of the Fe/CeH$_{2-\delta}$ system may be a signature of its different electronic structure. The study illustrates the power of the XMCD technique for studying element-resolved details of the magnetization process in thin-film heterostructures, which are not accessible by classical techniques.

1   G. Herzer, J. Magn. Magn. Mater **112**, 258 (1992), G. Herzer, IEEE Trans. Magn. **25** (1990) 1397

2   E. Kneller, Ferromagntismus, Springer, Berlin, 1962

3   R.S. Trebble and D.J. Craik, magnetic materials, London: Wiley-Interscience, ch.1, pp.33-35,1969

4   F. Klose, M. Steins, T. Kacsich, and W. Felsch, J. Appl. Phys. 74, 1040-1045 (1993), F. Klose et al. Phys. Rev. B **50**, 6174 (1994)

5   J. Thiele, F. Klose, A. Schurian, O. Schulte, W. Felsch, and O. Bremert, J. Magn. Magn. Mater. **119**, 141-149 (1993)

6   M. Arend, M. Finazzi, O.Schulte, M. Münzenberg, A.-M. Dias, F. Baudelet, Ch. Giorgetti, E. Dartyge, P. Schaaf, J.-P. Kappler, G. Krill, and W. Felsch, Phys. Rev. B **57**, 2174 (1998).

7   Ph. Bauer, F. Klose, and W. Felsch, J. Magn. Magn. Mater.**138**, 163 (1994).

8   A .J. Freeman, in *Hyperfine Structure and Nuclear Radiations*, E. Matthias and D.A. Shirley (ed.), North-Holland Pupl. Comp., Amsterdam

9   M. S. S. Brooks, B. Johansson, J. Phys. F. 13, L197 (1983), J.F. Janak, Phys. Ref. B 16, 255 (1977)

10 M. Münzenberg, Diplomarbeit, Universität Göttingen (1997)

11 K. Suzuki and J. M. Cadogan, Phys. Rev. B **58**, 2730 (1998)

12 L. Sève, N. Jaouen, J. M. Tonnerre, D. Raoux, F. Bartolomé, M. Arend, W. Felsch, A. Rogalev, J. Goulon, C. Gautier, and J. F. Bérar, Phys. Rev. B **60**, 9662 (1999)

13 N. Jaouen, J.M. Tonerre, E. Bontempi, D.Raoux, L. Sève, F. Bartolomé, A. Rogalev, M. Münzenberg, W. Felsch, H.A. Dürr, E. Dudzik, H. Maruyama, Physica B **283**, 175 (2000)

6. Summary

This work illuminates the unique possibilities of circular magnetic dichroism in X-ray absorption (XMCD) for the studies of ordered magnetism. The element and electron-shell sensitivity of this spectroscopic method is used to study the magnetic properties of multilayer systems with Fe and Ce, La and Gd as the main constituents. Emphasis is laid on the $L_{2,3}$ spectra of the RE which are theoretically not well understood. Strong electronic correlations are effective in the multilayers. With the exception of the Gd-based heterostructures below 20 K, the rare-earths are magnetically polarized by Fe.

The first part of the thesis is concerned with the systems Fe/REH_x. The 4f-electron states of Ce are localized here, like in Gd. Magnetism of the RE-5d states near the interfaces was studied for different thicknesses of the hydrides by measuring XMCD at the RE-$L_{2,3}$ edges. The main interest was to probe the impact of the metal-to-insulator transition in the REH_x sublayers on the spectra. It is produced by increasing the hydrogen content to $x > 2.8$ ($x > 2.3$ for GdH_x) for which the 5d band becomes depleted of electrons. An astonishing result is that the magnetic polarization of the RE-5d band does not vanish in the insulating hydride. The XMCD signal is reduced by a factor of two to three for the three systems. The Fe-induced interface polarization decreases exponentially from the interface into the REH_x sublayers, with a characteristic penetration length of ~10 Å both in their metallic and insulating phase.

The $L_{2,3}$-XMCD spectra are analyzed in a phenomenological two-parameter model

(denoted α-β model). It explains the observed shapes of the dichroic signals qualitatively. The exchange interaction between the 4f and 5d electrons results in a contraction of the 5d orbital for one spin direction which enhances the 2p-to-5d dipole transition probability. This so-called 'breathing' effect competes with the contribution of the magnetic polarization of the 5d states to the dichroic spectra and may reverse their sign. This is observed for the Fe/GdH_x systems, and, at low temperatures, for the Fe/CeH_x system. A second effect of the 4f-5d exchange interaction is an energy shift of the absorption edges for the two directions of the 5d magnetization relative the photon helicity. It produces a derivative-like spectrum if the effect of the enhanced 2p-5d transition probability and the 5d polarization compensate.

The second part is devoted to the multilayer system $Fe/Ce_{1-x}Si_x$. X-ray absorption spectra at the Ce L and M edges reveal that the degree of localization of the Ce-4f states increases with increasing concentration of the s-p element Si, but the electronic configuration of Ce remains α-phase like. The variation is reflected in the evolution of the XMCD spectra at the $Ce-L_{2,3}$ edges: for x=0.65 a reversed sign is found a low temperature, similarly as in the case of the Fe/CeH_x system, where the Ce-4f configuration is γ-phase like. It is attributed to an increased 4f-5d exchange interaction which is manifest also in the XMCD spectra measured at the $Ce-M_{4,5}$ edges. The spectra reveal an increased ordered magnetic 4f moment.

The experiments on the Fe/GdH_x multilayers demonstrate that the element selectivity of XMCD is an indispensable tool to decompose different magnetic contributions in a multicomponent system where classical methods in magnetometry probe the overall magnetization. Here, measurements at the $L_{2,3}$ edges of Gd permit to determine the antiferromagnetic transition in the GdH_x

sublayers embedded in between Fe, in the metallic and isolating phase. It occurs near 20 K as in bulk metallic GdH_2, but in contrast to the bulk hydride the Néel temperature does not vary much if the material becomes insulating.

The element selectivity of XMCD is also used to investigate the role of the interfaces in Fe/Ce multilayers in the process of magnetization reversal in an applied magnetic field. Measurements are presented of the hysteresis curve in the Ce-5d magnetization. They are compared to magnetization curves measured by MOKE, which essentially probe the Fe-layer contribution. The MOKE loops reveal that this multilayer system is very soft magnetically. This is related to the amorphous structure of Ce. The coercivity of the Ce-5d hysteresis is 50% smaller than that of the Fe layers. The effect is unexpected since ordered magnetism on Ce is induced by Fe. The different magnetic response of the Ce-5d and Fe layers may be attributed to the magnetically soft interfaces in the heterostructures. However, a relation to the complex non-collinear magnetic structure in the Ce sublayers cannot be excluded.

Danksagung

An dieser Stelle möchte ich mich bei all denjenigen bedanken die zum Gelingen dieser Arbeit beigetragen haben:

- Wolfgang Felsch für die Themenstellung, für seine Betreuung in den letzten Jahren, die vielen guten Ideen und interessanten Diskussionen, sowie für seinen unermüdlichen Einsatz.

- Wiebke Lohstroh, Markus Arend, Frank Leuenberger, Björn Sass und Ulrike Lüders für anregende Diskussionen und die freundschaftliche und fröhliche Zusammenarbeit.

- Thomas Neisus, für sein besonderes Interesse und seinen ständigen Einsatz, sowie Alain Fontaine, Stefania Pizzini und Sakura Pascarelli für die engagierte Zusammenarbeit bei den Experimenten an der dipersiven Beamline ID 24 am ESRF.

- Gérard Krill für das Interesse an der Arbeit und die vielen Diskussionen

- Christian Theodoresçu, Jean-Paul Kappler, Anne Delobbe und Jean-Jacques Gallet am Super ACO sowie Elisabeth Dartyge, François Baudelet, Christine Giorghetti, und Agnes Travèrse am DCI für ihre Mithilfe, Betreuung und guten Tips bei den Experimenten.

- Ein besonderes Dankeschön gilt den Mitarbeitern des I. Physikalischen Institutes für die freundschaftliche und angenehme Atmosphäre, sowie für ihre fortwährende Unterstützung.

Lebenslauf

Name: Markus Münzenberg

Geburtstag: 30.05.1971

Geburtsort: Gießen

Schulausbildung:

1978-82:   Grundschule, Georg-August-Zinn-Schule, Darmstadt-Wixhausen

1982-84:   Förderstufe, Thomas-Mann-Schule, Darmstadt-Arheiligen

1984-91:   Gymnasium, Justus-Liebig-Schule, Darmstadt

1991 :   Abitur

Zivildienst:

1991-1992:   St. Hildergardis Hospital, Mainz

Hochschulausbildung:

Studium der Physik an der Universität Göttingen vom WS 1992/1993-WS 2000/2001

1994:   Vordiplom

1997:   Diplom

               Thema der Diplomarbeit "Untersuchungen zur Zwischenschichtkopplung bei [La/Fe]-Vielfachschichten und am Reorientierungsübergang von [CeH$_2$/Fe]-Vielfachschichten mit dem magnetooptischen Kerreffekt"

1997-2000:   Wissenschaftlicher Angestellter im Sonderforschungsbereich 345

               der Universität Göttingen

               Anfertigen der vorliegenden Dissertation am I. Physikalischen Institut